UNIVERSITÀ DEGLI STUDI DI MILANO

Scuola di Dottorato in Fisica, Astrofisica e Fisica Applicata
Dipartimento di Fisica

Corso di Dottorato in Fisica, Astrofisica e Fisica Applicata
Ciclo XXVII

Microscopic studies of static and dynamic properties in quantum liquids and gases

Settore Scientifico Disciplinare FIS/03

Thesis Director: Professor Davide Emilio GALLI

Director of the Doctoral School: Professor Marco BERSANELLI

PhD Thesis of:
Filippo TRAMONTO

Academic Year 2013/2014

Commission of the final examination:

External Referee:
Professor Gaetano Senatore

External Member:
Professor Robert Grisenti

External Member:
Professor Danilo Giulietti

Final examination:

27 January 2015

Università degli Studi di Milano, Dipartimento di Fisica, Milano, Italia

To my grandfather Carlo,
It was with you that I began
to play with numbers,
to be curious of knowledge
and stubborn in overcoming obstacles
Thank you

Contents

Introduction

The study of quantum boson systems, such as superfluid ^{4}He, has played a very important role in the context of modern condensed matter physics, both providing extremely interesting experimental scenarios, and serving as a powerful test for many-body theories and computational methods. Indeed these systems, though possessing all the features of strongly interacting ones, do not have the added complexity related to Fermi statistics or to nuclear physics, and so it is possible to describe them from "first principles" with a high level accuracy, starting from a microscopic Hamiltonian, and also to investigate their properties, on a quantitative basis, using computational techniques like *quantum Monte Carlo* methods.

However, the theoretical study of quantum Bose liquids and gases is not an easy task. Due to the strong repulsive core in the interparticle interaction, perturbative approaches often used in study of many-body systems are not feasible. In fact, a strongly interacting system can be described as a system where one cannot define a small parameter on which a perturbative theory can be built. This complication has inspired the development of numerical approaches based on the variational principle [1], and of quantum Monte Carlo methods [2–6] that, in the case of boson systems, are in principle "exact".

From a more general point of view, the quantum Monte Carlo methods are very convenient tools to investigate quantum many-body problems for two reasons: first, they are *ab initio* approaches, therefore they help to understand the properties of the many-body system from a microscopic perspective; second, they allow for studying different condensed-matter systems, e.g. quantum liquids [4], quantum solids [7], electron gases [8], nuclear matter [9] and ultracold gases [10], using the same theoretical tool. Information about important phenomena obtained in one particular field can be transported to the other fields of physics to obtain a more general understanding.

In the work we carried out, presented in this dissertation, we concentrated on two fundamental issues in quantum many-body theories and condensed matter physics, related to the study of Bose quantum many-body systems: the first concerns the characterization of low-energy excited states by means of calculations of imaginary-time correlation functions; while the second regards the characterization of local structures in non-homogeneous quantum systems.

The issue of low-energy dynamics of boson systems has been always of great historical interest, starting from the study of superfluid helium, for which excited states play a central role in the explanation of the phenomenon of superfluidity and its properties. Then, after the realization of Bose-Einstein condensates in ultracold gases (and also of BCS phases and BEC-BCS crossover) a new world was opened for exploration. Thanks to the possibility to tune the strength of the interaction between the elements constituting the quantum system, the experimentalists are able to realize a great variety of model Hamiltonians and are also able to create complex systems mixing different kinds of constituents. Two main theoretical paradigms exist for the description of the excited state spectrum for Bose systems: Bogoliubov's theory for weakly-interacting systems, well represented by dilute ultracold gases, and Feynman's theory of the energy-momentum dispersion relation in quantum boson fluids, able to describe qualitatively the phonon-maxon-roton spectrum that characterizes strongly-interacting Bose systems, like superfluid ^{4}He. There are still some open questions and issues concerning those two paradigms. One question is whether we can provide a unified theoretical approach able to describe collective excitations, from the weakly-interacting to the strongly-interacting regimes. Another question is if we can describe both of these interacting regimes with a single system model. These two questions are dealt with directly in part of the research work presented in this dissertation. We have studied dynamic properties of hard sphere systems from the weakly-interacting to the strongly-interacting regime. Another investigation, the result of a collaboration with T. Minoguchi of the University of Tokyo regarding the freezing of superfluid helium-4, offered the possibility of studying static properties and low energy excitations of another model many-body system: the system of distinguishable particles, i.e. particles obeying Boltzmann statistics, called boltzmannons [4, 11, 12], in a temperature regime where, if they were ^{4}He atoms, i.e. bosons, they would form a superfluid phase. This Boltzmann system is very intriguing, as it would allow to recognize and study effects on static and dynamic properties only caused by quantum particle delocalization, allowing one to isolate th additional effects brought about by Bose statistics.

How we can characterize the low-energy excited states of many-body systems, such as the ones we have just described? In order to carry out such investigations we need to calculate the spectral functions or, their time Fourier transform, i.e. the time correlation functions. The *ab initio* determination of spectral functions of a quantum many-body system is an extremely difficult problem. Feynman showed that it is an NP complete problem and suggested that quantum computers would offer a solution [13]. The quantum Monte Carlo methods based on path integrals [4], have allowed for the accurate study of static properties for strongly interacting many-particle systems, but they make use of imaginary-time propagation. The calculation of estimates of time-dependent observables using real-time propagation requires evaluation of multidimensional integrals of rapidly oscillating exponentials. For this purpose, the stochastic methods based on importance sampling, e.g. the diffusion Monte Carlo (DMC) method, are inefficient and generate statistical errors, that grow exponentially with time. This is called the *real-time sign problem* and is the main barrier to the use of numerical simulations to calculate real-time correlation functions [14]. But there is another, more indirect, way to determine the dynamic structure factor. By means of quantum Monte Carlo calculations we can obtain the imaginary-time intermediate scattering function, that is the Laplace's transform (bilateral for T>0) [4] of the dynamic structure factor. The latter could be determined by the inversion of the transform. But this inversion, also called analytic continuation, is an *ill-posed* inverse problem [15].

The ill-posed inverse problems are studied in general with two different classes of methods: regularization techniques and statistical inversion methods. In the first class, instead of trying to solve directly the equation to invert (the transform), one seeks to find a nearby "regularized" problem, that has a unique solution and that is robust with respect to errors in the data; in other words, one renders the ill-posed problem a problem solvable with a unique solution. While the methods in the second category do not try to determine a solution, but aim to extract information on the solution from the data in order to select the models (the possible solutions) most compatible with the computed data [16–20]. The recently introduced Genetic Inversion via Falsification of Theories (GIFT) method [21], belonging to the latter class, offers an alternative approach based on the concept of *falsification* of models through the use of a genetic algorithm to explore the space of spectral function models with the purpose of finding and collecting a large group of compatible models, discarding the non-compatible ones, and retaining only the features shared in the majority of them.

Regarding the issue of the study of local structures in quantum many-body systems, a fundamental open problem in condensed matter physics is the understanding of crystallization in supercooled liquids [22]. Supercooled liquids are liquids at a temperature below their melting point, so that either they are in a metastable phase with respect to the solid phase, or they are in the non-equilibrium dynamic process toward solidification. The underlying mechanics for crystallization are still poorly understood [23], as they are rooted in a complicated interplay between thermodynamic properties, particle dynamics and geometric effects. Crystallization itself usually is divided into the initial formation of embryos, i.e. the *nucleation*, and the subsequent proceeding transformation of the liquid, i.e. the *crystal growth*. Both the nucleation and the crystal growth strongly depends on the microscopic structural properties of the liquid, which vary spatially in the system due to statistical fluctuations. These local fluctuations and structures become more important when the liquid consists of several substances. In this regard, an open question extensively debated in these days is the connection between crystallization and its antagonist vitrification (or glass formation) [24]. In this case the investigation of the dynamic processes in supercooled liquids that control the crystal growth is important to understand the nature of glass transition [25–29]. Mixing a few components, for example creating binary mixtures, is a common strategy to hinder crystallization and, eventually, to induce the formation of glass.In this context two experimental groups performed measurements on the dynamics of crystallization of supercooled liquids of p-H_2–o-D_2 mixtures [30] and of mixtures of p-H_2, and o-D_2, with Ne. They found a strong slow-down of crystallization with increasing content of o-D_2 molecules in p-H_2 supercooled liquid. In addition, the results on p-H_2/o-D_2–Ne mixtures showed an even greater slow-down. To explain these results, we investigated static structural correlations and microscopic structures in supercooled liquids, by means of path integral Monte Carlo (PIMC) simulations.

The structure and the properties of materials in reduced dimensionality are also important issues in condensed matter physics, and confinement effects are one of the key themes. Indeed, it is known that the interplay between confining potential and interparticle interaction may generate completely new phenomena, as well as strongly enhancing correlation effects. Confinement can derive from an external potential as in the case of He absorbed on a substrate, or can derive from self-binding of a limited number of particles. This is the case of nanodroplets of He doped with attractive ions, in which the ion-He and He-He interactions are responsible for the confinement. Confinement causes a large variety of new and interesting phenomena. For instance, the internal structure of the fluid can became more ordered by contact with an impurity. When the helium acts as an embedding matrix on molecular complexes or charged impurities, important structural and dynamic properties of the embedding quantum environment are made more manifest and can be more easily studied. For example, ^{4}He nanodroplets doped with different positive ions are studied. A recent experimental work [31], used spectroscopic techniques to investigate ^{4}He nanodroplets doped with ions of noble gases. For the nanodroplets doped with a positive argon ion $Ar^+@^4He_n$, the authors found three *magic numbers*, 12, 32, and 44, that were interpreted as evidence of three distinct solvation shells containing 12, 20 and 12 helium atoms, from the first to the third shell, respectively. Their interpretation had been also suggested by a previous PIMC study by Galli et al. [32] on ^{4}He nanodroplets doped with a positive sodium ion Na^+, which found a solid structure around the ion consisting of 3 concentric solvation shells: an icosahedron (12 atoms), a dodecahedron (20 atoms), and an icosahedron (12 atoms), going from the first inner shell to the third shell. In order to confirm the existence of these structure also in $Ar^+@^4He_n$ complexes, we carried out PIMC simulations which are part of the research work presented in this dissertation.

Guide to the thesis

In this thesis I present studies of dynamic and static properties of quantum liquids and gases by means of quantum Monte Carlo (QMC) techniques at zero temperature (PIGS), as well as at finite temperature (PIMC) on different quantum systems.

The thesis is organized as follows.

1. In Chapter 1, I describe the path integral Monte Carlo (PIMC) method and the path integral ground-state method (PIGS). Both methods are based on the path integral formalism developed by Feynman. I present these two methods in a unified scheme by using the same notation. I do not go into the technical details of Metropolis moves and computed estimators, as nowadays, their implementation is widely covered in the literature. I also briefly present the worm algorithm; this allows to sample the exchanges of the quantum particles, more efficiently if compared to the standard PIMC algorithm, and thus more accurately accounts for the effects of the Bose statistics. Then I explain in detail the approximations of the propagator for short imaginary times that have been employed in the research work presented in this thesis. In particular, I describe a new short-time propagator that we developed and exploited in the study of helium-4 nanodroplets doped with a positive argon ion, presented in Chapter 6.

2. Chapter 2 is devoted to the discussion of dynamical properties and their numerical computation. First I introduce and give a derivation of the dynamic structure factor from scattering theory, also describing some of its main properties. I define related quantities, as the density response function and the time correlation functions. Then I present the problem of analytic continuation, i.e. the extraction of spectral functions from imaginary-time correlation functions. After a brief description of some inversion methods used in literature, I present in detail our inversion method, called Genetic Inversion via Falsification of Theories (GIFT), developed within our research group.

3. In Chapter 3, I present a study of the excited states of Bose hard sphere gases from the weakly to the strong interacting regime, as well as in metastable gas and solid phases, by means of the GIFT method. We have also studied static properties like the static density response function, the static structure factor, the one-body density matrix and the equation of state near freezing.
   These studies have been published in:
   R. Rota, F. Tramonto, D. E. Galli, and S. Giorgini, "Quantum Monte Carlo study of the dynamic structure factor in the gas and crystal phase of hard-sphere bosons", *Physical Review B* **88**, 214505 (2013).
   R. Rota, F. Tramonto, D. E. Galli, and S. Giorgini, "Many–body Bose systems and

the hard-sphere model: dynamic properties from the weak to the strong interaction regime", *Journal of Physics: Conference Series* **529** 012022 (2014).

4. In Chapter 4, I present the results of investigations with path integral Monte Carlo simulations to compute energy versus density, the static and dynamic structure factors, and the density response function of a *Boltzmann*-liquid ^{4}He, near freezing and below the superfluid ^{4}He transition temperature. The results of simulations are used also as inputs for describing the freezing of superfluid helium-4 by means of calculations, performed by our collaborator T. Minoguchi, using a modified density functional technique.
   Part of these results are published in:
   T. Minoguchi, M. Nava, F. Tramonto and D.E. Galli, Density Functional Theory and Bose Statistics for the Freezing of Superfluid ^{4}He, *Journal of Low Temperature Physics* **171**, 259 (2013).

5. In Chapter 5, I describe the PIMC simulations we carried out in order to investigate the microscopic origin of the crystallization slow-down observed in supercooled liquids of p-H_2–o-D_2 mixtures, as well as mixtures of p-H_2, and o-D_2, with Ne. Then I show the results for the partial radial distribution functions, and for the local orientational order correlations. Some details of the experiments performed by our collaborators (groups of R. E. Grisenti and S. Montero) are also discussed.
   Part of the results presented here are published in:
   M. Kühnel, J. M. Fernández, F. Tramonto, G. Tejeda, E. Moreno, A. Kalinin, M. Nava, D. E. Galli, S. Montero, R. E. Grisenti, "Observation of crystallization slow-down in supercooled parahydrogen and orthoùdeuterium quantum liquid mixtures", *Physical Review B* **89**, 180201(R) (2014).

6. In the last Chapter, I present the studies on ^{4}He nanodroplets doped with an Ar^+ ion. After a brief background introduction, I show the results on density profiles, structures of solvation shells, and total and dissociation energies of Ar^+ doped ^{4}He nanodroplets.
   The results are published in:
   F. Tramonto, P. Salvestrini, M. Nava, D. E. Galli, "Path Integral Monte Carlo study confirms a highly ordered snowball in ^{4}He nanodroplets doped with an Ar+ ion", *Journal of Low Temperature Physics* (2015), Doi: 10.1007/s10909-014-1266-6.

Chapter 1

Path Integral Methods

In this chapter I present the Quantum Monte Carlo (QMC) numerical methods employed in the research projects on which I worked during the PhD. The employed methods are Path Integral Monte Carlo (PIMC) [4], for systems at finite temperature, and Path Integral Ground State (PIGS) [6], for systems at zero temperature. Both are based on the Feynman path integral formalism and allow to calculate a number of physical properties of quantum systems. In particular, for systems of bosons or distinguishable particles, given a Hamiltonian of a finite system, the computed physical estimates are exact. "Exact" means that all systematic errors can be arbitrary reduced below the statistical errors and the only required input are interatomic potentials.

In the first two sections I introduce the PIMC and PIGS methods, then in the following sections I explain both common and specific aspects of the two methods.

1.1 Path Integral Monte Carlo

In principle, all static and dynamic properties of a many-body quantum system at thermodynamic equilibrium are described by the thermal density-matrix

$$\hat{\rho} = \sum_i \frac{e^{-\beta E_i}}{Z} |i\rangle\langle i| = \frac{e^{-\beta \hat{H}}}{Z}, \tag{1.1}$$

where $\{|i\rangle\}$ is an orthonormal complete set of eigenvectors of the Hamiltonian $\hat{H}$ of the system; E_i are the energy eigenvalues of $\hat{H}$; β is proportional to the inverse of the temperature, $\beta = 1/k_{\mathrm{B}}T$ (k_{B} is the Boltzmann constant) and Z is the partition function (in the canonical ensemble, where the total number of particles N the volume V and the temperature T are fixed)

$$Z = \sum_i e^{-\beta E_i} = \mathrm{Tr}\Big(e^{-\beta \hat{H}}\Big). \tag{1.2}$$

An eigenvalue of $\hat{\rho}$, $e^{-\beta E_i}/Z$, is the probability to find the system, at the thermodynamic equilibrium at the temperature T, in the eigenstate $|i\rangle$. In general, the expectation value of a physical observable $\hat{O}$ is given by

$$\left\langle \hat{O} \right\rangle = \mathrm{Tr}(\hat{\rho}\,\hat{O}) = \mathrm{Tr}\left(\frac{e^{-\beta\hat{H}}}{Z} \hat{O} \right) = \frac{\mathrm{Tr}\left(e^{-\beta\hat{H}} \hat{O} \right)}{\mathrm{Tr}\left(e^{-\beta\hat{H}} \right)} \tag{1.3}$$

In coordinate representation, the density matrix is formally rewritten as

$$\rho(\mathbf{R},\mathbf{R}') = \langle \mathbf{R} | \hat{\rho} | \mathbf{R}' \rangle = \langle \mathbf{R} | \frac{e^{-\beta\hat{H}}}{Z} | \mathbf{R}' \rangle \tag{1.4}$$

where $\mathbf{R} = \{r_1, \dots, r_N\}$ and $\mathbf{R}' = \{r'_1, \dots, r'_N\}$ represent two possible sets of positions of the N particles making up the system, also called configurations. Likewise the partition function Z is given by

$$Z = \int \mathrm{d}\mathbf{R} \ \langle \mathbf{R} | e^{-\beta\hat{H}} | \mathbf{R} \rangle \,. \tag{1.5}$$

Equation 1.3, in coordinates representation, becomes

$$\left\langle \hat{O} \right\rangle = \frac{1}{Z} \int \mathrm{d}\mathbf{R} \ \langle \mathbf{R} | e^{-\beta\hat{H}} \hat{O} | \mathbf{R} \rangle = \int \mathrm{d}\mathbf{R}\, \mathrm{d}\mathbf{R}'\, \rho(\mathbf{R},\mathbf{R}') \, \langle \mathbf{R}' | \hat{O} | \mathbf{R} \rangle \,, \tag{1.6}$$

where in the second equality we introduced the resolution of identity $1 = \int \mathrm{d}\mathbf{R}' \, |\mathbf{R}'\rangle\langle\mathbf{R}'|$. For convenience, and for consistency with the notation of the PIGS method (Section 1.2), we redefine the density matrix as the propagator in the imaginary-time evolution

$$G(\mathbf{R},\mathbf{R}';\beta) \equiv Z\rho(\mathbf{R},\mathbf{R}') = \langle \mathbf{R} | e^{-\beta\hat{H}} | \mathbf{R}' \rangle \,. \tag{1.7}$$

Thus we have

$$\left\langle \hat{O} \right\rangle = \frac{1}{Z} \int \mathrm{d}\mathbf{R}\, \mathrm{d}\mathbf{R}'\, G(\mathbf{R},\mathbf{R}';\beta) \, \langle \mathbf{R}' | \hat{O} | \mathbf{R} \rangle \,. \tag{1.8}$$

The PIMC [4] method is based on the fact that we can write the operator $e^{-\beta\hat{H}}$ as the product of M operators $e^{-\delta\tau\hat{H}}$, with $\delta\tau = \beta/M$,

$$e^{-\beta\hat{H}} = \left(e^{-\delta\tau\hat{H}} \right)^M . \tag{1.9}$$

The quantity $\delta\tau$ is called *imaginary-time step*, since the density matrix operator, apart from the normalization factor $1/Z$, $Z\hat{\rho} = e^{-\beta\hat{H}}$ is formally equivalent to the time-evolution operator $e^{-it\hat{H}/\hbar}$ with $t = -i\hbar\beta$ ($\hbar$ is the reduced Plank constant). This is also the reason for which $e^{-\beta\hat{H}}$ is called *imaginary-time* evolution operator.

In coordinate representation, Eq. 1.9 (setting $\mathbf{R} \equiv \mathbf{R}_0$ and $\mathbf{R}' \equiv \mathbf{R}_M$) becomes

$$G(\mathbf{R}_0,\mathbf{R}_M;\beta) = \int \mathrm{d}\mathbf{R}_1 \cdots \mathrm{d}\mathbf{R}_{M-1} \ G(\mathbf{R}_0,\mathbf{R}_1;\delta\tau) \cdots G(\mathbf{R}_{M-1},\mathbf{R}_M;\delta\tau). \tag{1.10}$$

Therefore the expression of the expectation value $\left\langle \hat{O} \right\rangle$ 1.8 becomes

$$\begin{aligned} \left\langle \hat{O} \right\rangle &= \frac{1}{Z} \int \mathrm{d}\mathbf{R}_0 \cdots \mathrm{d}\mathbf{R}_M \ G(\mathbf{R}_0,\mathbf{R}_1;\delta\tau) \cdots G(\mathbf{R}_{M-1},\mathbf{R}_M;\delta\tau) \, \langle \mathbf{R}_M | \hat{O} | \mathbf{R}_0 \rangle \,, \\ \text{with} \quad Z &= \int \mathrm{d}\mathbf{R}_0 \cdots \mathrm{d}\mathbf{R}_{M-1} \, G(\mathbf{R}_0,\mathbf{R}_1;\delta\tau) \cdots G(\mathbf{R}_{M-1},\mathbf{R}_0;\delta\tau) \,. \end{aligned} \tag{1.11}$$

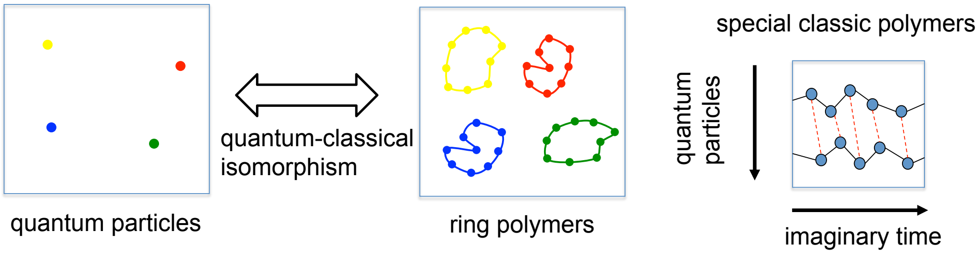

Figure 1.1 (left) Schematic representation of the quantum-classical isomorphism (see, e.g., [4]) between the quantum particles and the *ring*-polymers whose configurations are sampled with Metropolis moves during the PIMC simulations for $T > 0$. (right) Representation illustrating the interaction between beads at the same imaginary time.

We note that, the expression 1.10 for the propagator $G(\mathbf{R}_0, \mathbf{R}_M; \beta)$ is exact for each $M \geq 1$. The expression 1.10 can be read as the decomposition of the evolution of the system in imaginary time $-i\hbar\beta$, from the initial configuration $\mathbf{R}_0$ to the final configuration $\mathbf{R}_M$, in M evolutions of shorter imaginary times $-i\hbar\delta\tau$, from the configuration $\mathbf{R}_l$ to the configuration $\mathbf{R}_{l+1}$ ($l = 0, \ldots, M-1$). In Eq. 1.10 all of the possible configurations $\mathbf{R}_0, \ldots, \mathbf{R}_M$ are integrated, and thus we are integrating on all of the possible discretized *paths* of the many-body system that start from the configuration $\mathbf{R}_0$ and end in the configuration $\mathbf{R}_M$. In general, the expression of the propagator $G(\mathbf{R}, \mathbf{R}'; \delta\tau)$ for a many-body system is not known. However, if M is sufficiently large, $\delta\tau$ is small. In that case it is possible to approximate $G(\mathbf{R}, \mathbf{R}'; \delta\tau)$ to a known analytical expression, accurate (i.e. with a very small bias) for small values of imaginary time step $\delta\tau$. In literature there are various forms of these analytical expressions, each with a different degree of accuracy, i.e. that produce a different bias (systematic error) in the value of the calculated physical quantities, as will be discussed in Section 1.6. In this way, by representing the density matrix (the propagator) of a many-body system at thermodynamic equilibrium through an integral on imaginary-time discretized paths, we obtain a correspondence between a system of quantum particles with a classic system of interacting polymers [4], a system that adapts very well to being studied with Monte Carlo methods. Such correspondence is schematically illustrated in the left part of Fig. 1.1. Each quantum particle is associated with a classic polymer. These polymers interact in a particular way, since the interaction only takes place at the same imaginary time, and not between different times. In other words, in each polymer, a monomer interacts with another polymer only through the corresponding monomer at the same imaginary time [4], as illustrated in the right part of Fig. 1.1 . We also note that the trace in Eq. 1.3 implies that for most of the physical observables, for which one can express the matrix element $\langle \mathbf{R}_M | \hat{O} | \mathbf{R}_0 \rangle$ with an analytical expression (an estimator) in function of the coordinates, the initial configuration (in imaginary time) $\mathbf{R}_0$ coincides with the final one $\mathbf{R}_M$ and therefore the polymers form rings [4].

However, if we want to simulate a Bose system, i.e. particles have to obey the Bose statistics, we have to consider the permutations of particle coordinates. I will discuss this point in Section 1.4.

1.2 Path Integral Ground State

The PIGS method is a projection technique in imaginary time that, starting from an initial trial wave function $\Psi_T(\mathbf{R})$, projects it onto the ground-state wave function $\Psi_0(\mathbf{R})$ after an evolution over a long enough imaginary time interval τ. In fact, if $|\Psi_T\rangle$ is not orthogonal to the ground state $|\Psi_0\rangle$, the following relation holds

$$|\Psi_0\rangle = \lim_{\tau\to\infty} \mathcal{N}_\tau e^{-\tau\hat{H}} |\Psi_\mathrm{T}\rangle \,, \tag{1.12}$$

that is, in coordinate representation,

$$\Psi_0(\mathbf{R}) = \lim_{\tau\to\infty} \mathcal{N}_\tau \int \mathrm{d}\mathbf{R}'\, G(\mathbf{R},\mathbf{R}';\tau)\Psi_T(\mathbf{R}'), \tag{1.13}$$

where $\mathcal{N}_\tau$ is a normalization factor ($\mathcal{N}_\tau = e^{\tau E_0} / \langle\Psi_0|\Psi_T\rangle$), and in the second equation we have used the same imaginary-time propagator (Green's function) introduced above for the PIMC method $G(\mathbf{R},\mathbf{R}';\tau) = \langle\mathbf{R}|e^{-\tau\hat{H}}|\mathbf{R}'\rangle$, with $\beta = \tau$.

As stated above, the propagator is not known, in general, but for small time steps $\delta\tau$, various approximate analytical expressions of G are available. The adoption of one of these analytical forms is one of the two approximations which characterizes the PIGS method. Then, using the same expansion 1.10 employed for the PIMC method, with $\beta = \tau$ and, therefore, with $\delta\tau = \tau/M$, the ground-state wave function $\Psi_0(\mathbf{R})$ can be approximated with the multidimensional integral

$$\Psi_0(\mathbf{R}_M) \simeq \widetilde{\Psi}_0(\mathbf{R}_M) = \int \mathrm{d}\mathbf{R}_0 \cdots \mathrm{d}\mathbf{R}_{M-1}\; G(\mathbf{R}_M,\mathbf{R}_{M-1};\delta\tau) \cdots G(\mathbf{R}_1,\mathbf{R}_0;\delta\tau)\Psi_T(\mathbf{R}_0). \tag{1.14}$$

This choice corresponds to limiting the imaginary time propagation to $\tau = M\,\delta\tau$; this is the second approximation used in the PIGS method. The method is "exact" whenever this and the previous approximation affect the computed expectation values to an extent which is below their statistical uncertainty. Such a regime is always attainable by using a large enough M and a small enough $\delta\tau$ [33, 34].

The expectation value of a local observable, corresponding to the operator $\hat{O}$, is given

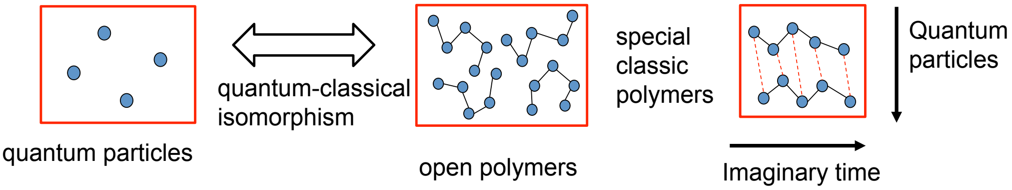

Figure 1.2 (left) Schematic representation of the quantum-classical isomorphism between the quantum particles and the *open* polymers which configurations are sampled with the Metropolis moves during the PIGS simulations for $T = 0$. (right) Representation illustrating the interaction between beads at the same imaginary time.

by

$$
\begin{aligned}
\left\langle \hat{O} \right\rangle &= \langle \Psi_0 | \hat{O} | \Psi_0 \rangle \simeq \frac{\langle \widetilde{\Psi}_0 | \hat{O} | \widetilde{\Psi}_0 \rangle}{\langle \widetilde{\Psi}_0 | \widetilde{\Psi}_0 \rangle} = \\
&= \int d\mathbf{R}_0 \cdots d\mathbf{R}_{2M} \, \frac{\Psi_T(\mathbf{R}_{2M}) G(\mathbf{R}_{2M}, \mathbf{R}_{2M-1}; \delta\tau) \cdots G(\mathbf{R}_1, \mathbf{R}_0; \delta\tau) \Psi_T(\mathbf{R}_0)}{\langle \widetilde{\Psi}_0 | \widetilde{\Psi}_0 \rangle} O(\mathbf{R}_M), \\
\text{with} \quad \left\langle \widetilde{\Psi}_0 \middle| \widetilde{\Psi}_0 \right\rangle &= \int d\mathbf{R}_0 \cdots d\mathbf{R}_{2M} \, \Psi_T(\mathbf{R}_{2M}) G(\mathbf{R}_{2M}, \mathbf{R}_{2M-1}; \delta\tau) \cdots G(\mathbf{R}_1, \mathbf{R}_0; \delta\tau) \Psi_T(\mathbf{R}_0).
\end{aligned}
\tag{1.15}
$$

Estimates like 1.15 can be interpreted as ensemble averages over a classical system of N polymers, which are *open*, in contrast to the *ring* polymers of the PIMC method. Each polymer $i = 1, \ldots, N$ is formed by $2M + 1$ monomers, or beads, corresponding to the coordinates $\{\boldsymbol{r}_i^{(0)}, \ldots \boldsymbol{r}_i^{(2M)}\}$; the sets of positions of the beads at the same imaginary time $\tau_l = l\delta\tau$ of all polymers determine the configuration of particles $\mathbf{R}_l = \{\boldsymbol{r}_1^{(l)}, \ldots, \boldsymbol{r}_N^{(l)}\}$. By virtue of the definition of $\Psi_0(\mathbf{R})$ in Eq. 1.14, only the central beads of the polymers are sampled according to the square of the ground-state wave function, and thus local operators (i.e. diagonal in coordinate representation), such as the one entering in Eq. 1.15, are evaluated only at the mid-point configuration $\mathbf{R}_M$.If we deal with non-local observables, such as the kinetic energy or any correlation function in imaginary time, Eq. 1.15) has to be modified since the corresponding estimators depend on more configuration points $\mathbf{R}$ [4].

Nonetheless, it is important to choose a sufficiently large number of projections M and to consider only the central part of the classical polymers for the evaluation of the averages. In the particular case of the ground-state energy, the identity

$$
\langle \Psi_0 | \hat{H} | \Psi_0 \rangle = \lim_{\tau \to \infty} \langle \Psi_T | e^{-2\tau \hat{H}} \hat{H} | \Psi_T \rangle \tag{1.16}
$$

provides one with an estimate in terms of the local energy $E_L(\mathbf{R}) = \langle \mathbf{R}|\hat{H}|\Psi_T\rangle / \Psi_T(\mathbf{R})$

$$E_{\mathrm{mix}} = \int \mathrm{d}\mathbf{R} f(\mathbf{R}) E_L(\mathbf{R}), \quad f(\mathbf{R}) = \int \prod_{l=0}^{2M-1} \mathrm{d}\mathbf{R}_l \, p(\mathbf{R}_0, \ldots, \mathbf{R}_{2M-1}, \mathbf{R}), \tag{1.17}$$

the so-called *mixed estimator* of energy[1], which is conveniently calculated starting from the trial wave function and has to be evaluated on either of the configurations, $\mathbf{R}_0$ or $\mathbf{R}_{2M}$, at the end-point of the polymers. Alternative estimators of the energy are also available, such as the direct and the virial estimator [4, 35]. However, unless the trial wave function is a particularly poor approximation of the ground-state wave function, it is preferable to use the energy mixed estimator for the calculation of $\langle \Psi_0|\hat{H}|\Psi_0\rangle$, since the other estimators typically suffer of a larger variance.

1.3 Monte Carlo methods: Metropolis algorithm

To calculate the estimates of physical observables, such as those given by Eqs. 1.11 and 1.15, QMC methods, like PIMC and PIGS, exploit the statistical approaches characteristic of the Monte Carlo (MC) methods. They make use of stochastic sampling, i.e. a generation of random numbers based on a certain probability distribution. These methods are well suited to be used in numerical calculations for quantum many-body systems, due to the large number of integration variables. In such systems the expectation values of physical observables are mainly calculated in the form

$$\left\langle \hat{O} \right\rangle = \int \mathrm{d}\mathbf{X} \, p(\mathbf{X}) \, O(\mathbf{X}), \tag{1.18}$$

where $\mathbf{X}$ indicates the set of N variables, specifying the *configuration* of the system, $O(\mathbf{X})$ is the *local value* of the operator $\hat{O}$ and $p(\mathbf{X})$ is the *probability density* that the system is in the configuration $\mathbf{X}$. If a sequence of P configurations $\mathbf{X}$ is generated from the probability $p(\mathbf{X})$, then the expectation value $\left\langle \hat{O} \right\rangle$ can be approximated as

$$\left\langle \hat{O} \right\rangle \simeq \frac{1}{P} \sum_{i=1}^{P} O(\mathbf{X}_i). \tag{1.19}$$

In the limit $P \to \infty$, the estimate 1.19 converges to the true value of the integral 1.18 according to a distribution that the central limit theorem sets to be a normal distribution with width proportional to $1/\sqrt{P}$; the width can be assumed as uncertainty of the estimation. To generate the $\mathbf{X}_i$ configurations, the *Metropolis algorithm* [36] is used. This is a very simple and effective technique, that allows to sample any probability density starting with a generator of random numbers uniformly distributed in the interval $[0, 1]$. The sequence of configurations is obtained through a stochastic process, according to the theory of Markov chains, that is, each configuration is generated by the previous one with a

---

[1] The probability density $p(\mathbf{R}_0, \ldots, \mathbf{R}_{2M-1}, \mathbf{R})$ will be defined in Eq. 1.23 in next section

probability of transition $T(\mathbf{X}_{\text{old}}|\mathbf{X}_{\text{new}})$ which satisfies the *principle of the detailed balance*

$$p(\mathbf{X}_{\text{old}})T(\mathbf{X}_{\text{old}} \mid \mathbf{X}_{\text{new}}) = p(\mathbf{X}_{\text{new}})T(\mathbf{X}_{\text{new}} \mid \mathbf{X}_{\text{old}}). \tag{1.20}$$

The Metropolis algorithm consists of the following steps: a move is attempted, i.e. a new configuration $\mathbf{X}_{\text{new}}$ is generated starting from the previous one $\mathbf{X}_{\text{old}}$ with the probability of transition $T(\mathbf{X}_{\text{old}}|\mathbf{X}_{\text{new}})$; this move will be accepted, or not, based on the probability

$$A(\mathbf{X}_{\text{old}} \mid \mathbf{X}_{\text{new}}) = \min\left(1, \frac{T(\mathbf{X}_{\text{new}} \mid \mathbf{X}_{\text{old}})p(\mathbf{X}_{\text{new}})}{T(\mathbf{X}_{\text{old}} \mid \mathbf{X}_{\text{new}})p(\mathbf{X}_{\text{old}})}\right); \tag{1.21}$$

accordingly $\mathbf{X}_{\text{new}}$ or $\mathbf{X}_{\text{old}}$ will added to the sequence of configurations, a new move is attempted, and so on. One can formally demonstrate that this procedure generate a sequence of configurations whose distribution converge to the probability density $p(\mathbf{X})$ [36, 37].

In the PIMC and PIGS methods presented in this Chapter, as can be seen comparing Eq. 1.18 with Eqs. 1.11 and 1.15, the probability distribution $p(\mathbf{X})$ is given, for the PIMC method, by the product of the propagators at small τ, i.e.

$$p(\mathbf{R}_0, \dots, \mathbf{R}_{M-1}) = \frac{1}{Z} G(\mathbf{R}_0, \mathbf{R}_1; \delta\tau) \cdots G(\mathbf{R}_{M-1}, \mathbf{R}_0; \delta\tau) \tag{1.22}$$

with $\mathbf{X} \equiv \{\mathbf{R}_0, \dots, \mathbf{R}_{M-1}\}$; while for the PIGS method, $p(\mathbf{X})$ is given, as well, by the product of the small-τ propagators, but also by the test wave functions $\Psi_T(\mathbf{R})$ evaluated in $\mathbf{R}_0$ and $\mathbf{R}_{2M}$, i.e.

$$p(\mathbf{R}_0, \dots, \mathbf{R}_{2M}) = \frac{\Psi_T(\mathbf{R}_{2M}) G(\mathbf{R}_{2M}, \mathbf{R}_{2M-1}; \delta\tau) \cdots G(\mathbf{R}_1, \mathbf{R}_0; \delta\tau) \Psi_T(\mathbf{R}_0)}{\langle \widetilde{\Psi}_0 | \widetilde{\Psi}_0 \rangle}, \tag{1.23}$$

with $X \equiv \{\mathbf{R}_0, \dots, \mathbf{R}_{2M}\}$.

To effectively explore the configuration space, in order to efficiently sample the probability density $p(\mathbf{X})$, various types of moves are used to continuously generate new configurations of the polymer system that will be accepted or not depending on the Metropolis algorithm. For example, the *rigid translation* of a whole polymer, the *Brownian bridge* that allows to move chains of beads of a polymer with a stochastic process, or moves that exchange parts of two polymers between them when they are sufficiently close, and so on [4, 33, 34, 38–40].

1.4 Bose statistics and *worm algorithm*

In the calculation of the expectation values, up to now we have considered the particles as distinguishable, i.e. obeying the Boltzmann statistics. If we want to treat the quantum system in which the Bose statistics is in effect, we must symmetrize the propagator 1.7, that is, it must now be symmetrical with respect to each exchange of position of a pair of particles. Practically, it is necessary to sum over all permutations of the coordinates of the particles of the propagator 1.7 in one of the two arguments,

$$G_{Bose}(\mathbf{R},\mathbf{R}';\beta) = \frac{1}{N!}\sum_{P} G(\mathbf{R},P\mathbf{R}';\beta). \tag{1.24}$$

Given that all terms of the sum are positive, it is possible to evaluate the expectation values with $G_{Bose}(\mathbf{R},\mathbf{R}';\beta)$ sampling the permutation space instead of directly calculating the sum. Note that with the PIMC method, for which the paths are closed, it is necessary to change the condition of closure ($\mathbf{R}_0 = \mathbf{R}_M$) into the condition $\mathbf{R}_0 = P\mathbf{R}_M$. Therefore, the ring-polymers are no longer closed on themselves, but can be connected to each other, thus forming long chains of monomers, which are also closed.

Then, in order to guarantee the Bose statistics we must also effectively sample the permutations between the quantum particles, i.e. between the polymers. The traditional way to do this is by cutting closed polymers at a point between two monomers and joining each free extremity to another of a different polymer, thus creating longer polymers. A more efficient technique for sampling such permutations is provided by the *worm algorithm*. It was developed for the first time for interacting boson system on lattice [41–43] and, later, extended to continuous-space systems in grand canonical ensemble [39, 40] and also in canonical ensemble [34, 44, 45] for PIMC simulations. The algorithm offers, in addition to an efficient permutation sampling, also a way to compute, within the same simulation, both diagonal and off-diagonal properties of the system under study. The worm algorithm works in a configurational space composed of two mutually exclusive spaces of configurations: one constituted by *diagonal* configurations (called ensemble Z), where only uncut polymers “live”, the other formed of *off-diagonal* configurations (called ensemble G, in the original terminology) where all the polymers are closed except one which is open (or divided in two pieces, with the PIGS method), usually referred to as the worm. The worm algorithm, thanks to its capability to sample efficiently the boson path permutations, generates an random walk which is ergodic and satisfying the detailed-balance principle (i.e. a Markov chain) through the permutation space. Thus, it allows for an efficient description of the thermodynamic properties connected to the Bose statistics of the quantum systems, such as the superfluidity effects or the off-diagonal correlations, and importantly for systems much greater than the ones accessible to conventional PIMC simulations. The worm algorithm can be used, and it is actually implemented in the codes used in the research project described in this thesis, also within the PIGS method. The advantage of doing this does not come from the efficiency of the worm algorithm in exploring off-diagonal configurations, because a similar efficiency is obtained with PIGS when “swap” moves are implemented. The benefit of using a worm-like algorithm here, instead, comes from the automatic normalization of one body density matrix ρ_1 (described in Section 1.7.1), which is a peculiarity of this method [39, 40].

1.5 Propagator

In order to be able to use the PIMC and PIGS methods effectively, it is necessary to have a good approximation for the propagator. First of all, we separate the Hamiltonian into a kinetic part and a potential part:

$$\hat{H} = \hat{T} + \hat{V}. \tag{1.25}$$

Expanding the evolution operator in imaginary time $e^{-\tau \hat{H}}$ we can obtain [46]

$$e^{-\tau(\hat{T}+\hat{V})} = e^{-\tau\hat{T}}\, e^{-\tau\hat{V}}\, e^{-\frac{\tau^2}{2}[\hat{T},\hat{V}]}\, e^{\frac{\tau^3}{6}[[\hat{T},\hat{V}],\hat{T}+2\hat{V}]} + O\big(\tau^4\big)\,. \tag{1.26}$$

For $\tau \to 0$, in the first approximation, the τ^2 and higher order terms can be ignored and we obtain

$$e^{-\tau(\hat{T}+\hat{V})} \simeq e^{-\tau\hat{T}} e^{-\tau\hat{V}}. \tag{1.27}$$

This is called *primitive approximation*. If we use this approximation for the propagator $G(\mathbf{R}, \mathbf{R}'; \delta\tau)$ in Eq. 1.10, in the limit for $M \to \infty$ the expansion of the propagator to large τ 1.10 remains exact. This is guaranteed by the Trotter formula [47]

$$e^{-\tau(\hat{T}+\hat{V})} = \lim_{M\to\infty} \left(e^{-\delta\tau\hat{T}} e^{-\delta\tau\hat{V}}\right)^M, \tag{1.28}$$

with $\delta\tau = \tau/M$ Therefore, if the integer number M, called *Trotter number*, is large enough, the propagator is well approximated.

The kinetic imaginary-time evolution operator $e^{-\delta\tau\hat{T}}$ and the potential one $e^{-\delta\tau\hat{V}}$ are easily writable in coordinates representation. The first, in the free space, turns out to be a propagator with Gaussian form,

$$\langle \mathbf{R} |\, e^{-\delta\tau\hat{T}}\, | \mathbf{R}' \rangle = \frac{1}{(4\pi\lambda\,\delta\tau)^{dN/2}} \exp\left(-\frac{(\mathbf{R}-\mathbf{R}')^2}{4\lambda\,\delta\tau}\right), \tag{1.29}$$

where $\lambda = \hbar^2/2m$. While the second is diagonal:

$$\langle \mathbf{R} | e^{-\delta\tau\hat{V}} | \mathbf{R}' \rangle = e^{-\delta\tau V(\mathbf{R}_l)} \delta(\mathbf{R}_l, \mathbf{R}_{l+1})\,. \tag{1.30}$$

For later convenience we also state the following definitions:

$$g^0(\boldsymbol{r}, \boldsymbol{r}'; \tau) \equiv \frac{1}{(4\pi\lambda\,\tau)^{d/2}} \exp\left(-\frac{(\boldsymbol{r}-\boldsymbol{r}')^2}{4\lambda\,\tau}\right), \tag{1.31}$$

$$G^0(\mathbf{R}, \mathbf{R}'; \tau) \equiv \prod_{i=1}^{N} g^0\big(\boldsymbol{r}_i, \boldsymbol{r}_i'; \tau\big) = \frac{1}{(4\pi\lambda\,\tau)^{dN/2}} \exp\left(-\frac{(\mathbf{R}-\mathbf{R}')^2}{4\lambda\,\tau}\right), \tag{1.32}$$

where $g^0(\boldsymbol{r}, \boldsymbol{r}'; \tau)$ is the propagator for a free single particle.

With the assumption that $\lambda\,\delta\tau \ll L^2$, the expression 1.29 is accurate also in the case that the many-body system is in a box with dimension $L = V^{1/d}$ and periodic boundary conditions. As regards the expression 1.30, since the exact propagator $G(\mathbf{R}, \mathbf{R}'; \tau) =$

$\langle \mathbf{R}|e^{-\tau(\hat{T}+\hat{V})}|\mathbf{R}'\rangle$ is symmetric for every τ, is more accurate to use a different approximation of the imaginary-time evolution operator, a "symmetrized" primitive approximation 1.27:

$$e^{-\tau(\hat{T}+\hat{V})} \simeq e^{-\frac{\tau}{2}\hat{V}} e^{-\tau\hat{T}} e^{-\frac{\tau}{2}\hat{V}}. \tag{1.33}$$

Therefore we have the symmetric expression of $\langle \mathbf{R}|e^{-\delta\tau\hat{V}}|\mathbf{R}'\rangle$:

$$\langle \mathbf{R}|e^{-\delta\tau\hat{V}}|\mathbf{R}'\rangle = \exp\left(-\frac{\delta\tau}{2}\left[V(\mathbf{R}) + V(\mathbf{R}')\right]\right). \tag{1.34}$$

Using Eqs. 1.10, 1.29 and 1.34, we come to the complete expression of the propagator in primitive approximation:

$$\begin{aligned} G(\mathbf{R}_0, \mathbf{R}_M; \tau) = {} & \frac{1}{(4\pi\lambda\,\delta\tau)^{d\,N/2}} \\ & \times \int \prod_{l=1}^{M-1} \mathrm{d}\mathbf{R}_l \exp\left(-\sum_{l=1}^{M}\left[\frac{(\mathbf{R}_{l-1} - \mathbf{R}_l)^2}{4\lambda\,\delta\tau} + \frac{\delta\tau}{2}(V(\mathbf{R}_{l-1}) + V(\mathbf{R}_l))\right]\right). \end{aligned} \tag{1.35}$$

1.6 High order approximations of the propagator

In addition to the primitive approximation, more accurate approximations, with greater order in $\delta\tau$, are used in the QMC methods. Several of them are based on decomposition of the imaginary-time evolution operator $e^{-\tau\hat{H}}$ in the kinetic operator of imaginary-time evolution operator $e^{-\tau\hat{T}}$ and in the exponential of an *effective-interaction* operator $\hat{U}$, i.e.

$$e^{-\tau\hat{H}} = e^{-\tau\hat{T}} e^{-\tau\hat{U}}. \tag{1.36}$$

In the coordinate representation, it translates into the decomposition of the propagator G in the *kinetic* part G^0 and in an *effective interaction* part G^{eff}.

$$G(R, R'; \tau) = G^0(\mathbf{R}, \mathbf{R}'; \tau)\, G^{\mathrm{eff}}(\mathbf{R}, \mathbf{R}'; \tau), \tag{1.37}$$

We note that within the primitive approximation, defined in Eq. 1.27 on the preceding page, G^{eff} is approximated with the symmetric propagator $\langle \mathbf{R}|e^{-\delta\tau\hat{V}}|\mathbf{R}'\rangle$ introduced in Eq. 1.34. The various approximations differ in the expression of G^{eff}. Since in the research projects presented in this dissertation, we have employed some of these approximations of the short-time propagator, I will discuss them in more detail in the following subsections.

1.6.1 Pair-product

One of the possible strategies to approximate the propagator at small time steps consists of writing it in the *pair-product* (PP) form [4, 48, 49]. That is decomposing the many–body effective potential propagator G^{eff} in a product of two–body propagators

$$G^{\text{eff}}(\mathbf{R},\mathbf{R}';\delta\tau) \simeq \prod_{1\le i<j\le N} G^{\text{eff}}_{\text{rel}}\left(\boldsymbol{r}_{ij},\boldsymbol{r}'_{ij};\delta\tau\right), \tag{1.38}$$

where $G^{\text{eff}}_{\text{rel}}\left(\boldsymbol{r}_{ij},\boldsymbol{r}'_{ij};\delta\tau\right)$ is the two–body effective-potential propagator of the interacting system, which depends on the relative coordinates $\boldsymbol{r}_{ij} \equiv \boldsymbol{r}_i - \boldsymbol{r}_j$. In this way, the short-time many-body propagator is given by

$$G(\mathbf{R},\mathbf{R}';\delta\tau) \simeq G^{PP}(\mathbf{R},\mathbf{R}';\delta\tau) = G^{0}(\mathbf{R},\mathbf{R}';\delta\tau) \prod_{1\le i<j\le N} G^{\text{eff}}_{\text{rel}}\left(\boldsymbol{r}_{ij},\boldsymbol{r}'_{ij};\delta\tau\right), \tag{1.39}$$

where G^0 is the free-particle propagator, defined in Eq. 1.32. Different methods exist to obtain $G^{\text{eff}}_{\text{rel}}$, one of these is to solve exactly the Schrödinger equation for two interacting particles, determining an exact two-body propagator.

1.6.2 Suzuki-Chin and pair Suzuki-Chin

Another approximation of the short-time many-body propagator is the pair Suzuki-Chin (PSC) approximation, given by

$$G^{\text{eff}}_{\text{rel}}\left(\boldsymbol{r}^{(l)}_{ij},\boldsymbol{r}^{(l+1)}_{ij};\delta\tau\right) \simeq \int \mathrm{d}r^{*,(l)}_{ij} \exp\left(-\frac{\tau}{3}\left[v_e\left(r^{(l)}_{ij}\right) + 4v_c\left(r^{*,(l)}_{ij}\right) + v_e\left(r^{(l+1)}_{ij}\right)\right]\right) \tag{1.40}$$

where $r^{(l)}_{ij} = \left|r^{(l)}_i - r^{(l)}_j\right|$ is the relative distance between the bead of the polymer i and the bead of the polymer j at the imaginary-time τ_l, while $r^{*,(l)}_{ij}$ is the relative distance between two beads at an imaginary-time τ^*_l between τ_l and τ_{l+1}, and

$$v_e(r) = v(r) + \frac{2}{3}\alpha\tau^2\lambda\left(\frac{\partial v(r)}{\partial r}\right)^2, \tag{1.41}$$

$$v_c(r) = v(r) + \frac{1}{3}(1-\alpha)\tau^2\lambda\left(\frac{\partial v(r)}{\partial r}\right)^2. \tag{1.42}$$

We note that the dummy integration variables $\{\boldsymbol{r}^*_i\}$ are required by the PSC approximation, and, with the parameter α set to zero, the configurations $\mathbf{R}^*_l$ at imaginary-time τ^*_l are fictitious, i.e. not used to estimate the physical observables, but exploited only by the short-time propagator.

1.6.3 Multiproduct Expansion and Pair-Multiproduct Expansion

Recently a high order approximation of the short-time many-body propagator has been proposed: the *multi-product expansion* (MPE) approximation [50, 51].

Let $\hat{G}_2(\delta\tau)$ denote the second order propagator in primitive approximation 1.27, in the symmetric form (see Eq. 1.34),

$$\hat{G}_2(\delta\tau) = e^{-\frac{\delta\tau}{2}\hat{V}} e^{-\delta\tau\hat{T}} e^{-\frac{\delta\tau}{2}\hat{V}}, \tag{1.43}$$

and given a set of n integer numbers $\{k_i\}$, then the multi-product expansion yields the following $2n$-th order propagator [50, 51]

$$\hat{G}_{2n}(\delta\tau) = \sum_{i=1}^{n} c_i \big[\hat{G}_2(\delta\tau/k_i)\big]^{k_i}, \quad c_i = \prod_{j=1(\neq i)}^{n} \frac{k_i^2}{k_i^2 - k_j^2}, \tag{1.44}$$

i.e. it is a propagator that is a sum of n products $\big[\hat{G}_2(\delta\tau_i)\big]^{k_i}$ with time-step $\delta\tau_i = \delta\tau/k_i$ $(i = 1, \dots, n)$.

In Ref. [50] is shown that convenient choices of $\{k_i\}$ for PIGS and PIMC are the sequences $\{k_i\} = \{1,2\}$, $\{k_i\} = \{1,2,4\}$ and $\{k_i\} = \{1,2,3,6\}$ in order to produce respectively the fourth ($n = 2$), sixth ($n = 3$), and eighth ($n = 4$) order propagator. In some of the projects I have worked on we used the MPE approximation at the eight-order, so let focus on $n = 4$. The choice $\{k_i\} = \{1,2,3,6\}$ produces a propagator in which the products in Eq. 1.44 can be represented by a path integral with a time-step $\delta\tau/6$. With the abbreviated notation $V_k = V(\mathbf{R}_k)$, the propagator is given by

$$\begin{aligned} G_8(\mathbf{R}_1, \mathbf{R}_7, 6\delta\tau) = & G^0(\mathbf{R}_1, \mathbf{R}_2; \delta\tau) \cdots G^0(\mathbf{R}_6, \mathbf{R}_7; \delta\tau) \\ & \times \Bigg[\frac{54}{35} e^{-\frac{\delta\tau}{2} V_1} e^{-\delta\tau V_2} e^{-\delta\tau V_3} e^{-\delta\tau V_4} e^{-\delta\tau V_5} e^{-\delta\tau V_6} e^{-\frac{\delta\tau}{2} V_7} \\ & - \frac{27}{40} e^{-\delta\tau V_1} e^{-2\delta\tau V_3} e^{-2\delta\tau V_5} e^{-\delta\tau V_7} + \frac{2}{15} e^{-\frac{3}{2}\delta\tau V_1} e^{-3\delta\tau V_4} e^{-\frac{3}{2}\delta\tau V_7} \\ & - \frac{1}{840} e^{-3\delta\tau V_1} e^{-3\delta\tau V_7} \Bigg] \end{aligned} \tag{1.45}$$

In the project presented in Chapter 4 we have introduced [52] the *pair multi-product expansion* (PMPE) approximation. It is built using the pair form of the many-body propagator 1.39 and by approximating the two–body propagator $G^{\text{eff}}_{\text{rel}}\big(\boldsymbol{r}_{ij}, \boldsymbol{r}'_{ij}; \delta\tau\big)$ with the MPE approximation 1.45 having substituted the many-body coordinates $\mathbf{R}$ and $\mathbf{R}'$ with the two-body relative coordinates $\boldsymbol{r}_{ij}$ and $\boldsymbol{r}'_{ij}$ respectively, obtaining

$$G(\mathbf{R}, \mathbf{R}'; \delta\tau) \simeq G_{\text{PMPE}}(\mathbf{R}, \mathbf{R}'; \delta\tau) = \prod_{i<j} G_8^{\text{rel}}\big(\boldsymbol{r}_{ij}, \boldsymbol{r}'_{ij}, \delta\tau\big). \tag{1.46}$$

1.7 Estimators

In this section I describe the estimators of some physical observables used in projects presented in this dissertation.

1.7.1 One body density matrix

In homogeneous systems at $T = 0$ the one body density matrix (OBDM) ρ_1 is defined via the equation

$$\rho_1(s) = \frac{\langle \Psi_0 | \hat{\psi}^\dagger(\boldsymbol{r} + \boldsymbol{s}) \hat{\psi}(\boldsymbol{r}) | \Psi_0 \rangle}{\langle \Psi_0 | \Psi_0 \rangle}, \tag{1.47}$$

in terms of the annihilation and creation operators of particles. The first quantization expression of $\rho_1(s)$ is given by

$$\rho_1(s) = \frac{\int \mathrm{d}\boldsymbol{r}_2 \cdots \mathrm{d}\boldsymbol{r}_N \, \Psi_0^*(\boldsymbol{r} + \boldsymbol{s}, ..., \boldsymbol{r}_N) \Psi_0(\boldsymbol{r}, ..., \boldsymbol{r}_N)}{\int \mathrm{d}\boldsymbol{r}_1 \cdots \mathrm{d}\boldsymbol{r}_N \, |\Psi_0(\boldsymbol{r}_1, ..., \boldsymbol{r}_N)|^2},, \tag{1.48}$$

and is suited for an estimate with the PIGS method obtained by cutting one of the N polymers at the position of the M-th bead, i.e. dividing one polymer into two half polymers with $M+1$ beads each, and by collecting the occurrences of the distances between the two loose ends. An efficient sampling of the relevant configurations and the normalization of ρ_1 are provided by the worm algorithm, illustrated in Section 1.4.

1.7.2 Estimator of dynamical correlation functions

A correlation function in imaginary time, for two generic operators $\hat{A}$ and $\hat{B}$, is defined as

$$C^i_{AB}(\tau) \equiv \left\langle \hat{A}(\tau) \, \hat{B} \right\rangle = \begin{cases} \mathrm{Tr}\left(\frac{e^{-\beta \hat{H}}}{Z} \hat{A}(\tau) \, \hat{B} \right) & \text{for} \quad T > 0 \\ \langle \Psi_0 | \hat{A}(\tau) \, \hat{B} | \Psi_0 \rangle & \text{for} \quad T = 0 \end{cases} \tag{1.49}$$

For simplicity, here after, I will consider only the case of finite temperature. For $T > 0$ the relation 1.49 becomes

$$C^i_{AB}(\tau) = \frac{1}{Z} \mathrm{Tr}\left(e^{-(\beta - \tau)\hat{H}} \hat{A} \, e^{-\tau \hat{H}} \hat{B} \right). \tag{1.50}$$

Furthermore I will suppose that operators $\hat{A}$ and $\hat{B}$ are diagonal with respect to the base of the coordinates. Thus the imaginary-time correlation function, in coordinate representation, is given by

$$C^i_{AB}(\tau) = \frac{1}{Z} \int \mathrm{d}\mathbf{R} \, \mathrm{d}\mathbf{R}' \, G(\mathbf{R}, \mathbf{R}'; \beta - \tau) \, A(\mathbf{R}') \, G(\mathbf{R}', \mathbf{R}; \tau) \, B(\mathbf{R}), \tag{1.51}$$

where $G(\mathbf{R}_1, \mathbf{R}_2; \alpha)$ is the propagator 1.7 introduced in the first paragraph. Using Eq. 1.10, the integral 1.51 is transformed into an integral on the discretized paths. Note that the paths are closed: we start from the configuration $\mathbf{R}$ and return to $\mathbf{R}$: the *rings* are formed. The correlation function is thus

$$\begin{aligned} C^i_{AB}(\tau) = \frac{1}{Z} \int \mathrm{d}\mathbf{R}_0 \cdots \mathrm{d}\mathbf{R}_n \cdots \mathrm{d}\mathbf{R}_{M-1} \; G(\mathbf{R}_0, \mathbf{R}_1; \delta\tau) \cdots G(\mathbf{R}_{n-1}, \mathbf{R}_n; \delta\tau) \\ \times A(\mathbf{R}_n) \, G(\mathbf{R}_n, \mathbf{R}_{n+1}; \delta\tau) \cdots G(\mathbf{R}_{M-1}, \mathbf{R}_0; \delta\tau) \, B(\mathbf{R}_0), \end{aligned} \tag{1.52}$$

where n is the number of time steps such that $n\,\delta\tau = \beta - \tau$ and, therefore, $(M-n)\,\delta\tau = \tau$.

In the specific case of the density fluctuation correlation function, determined in the context of the work presented in this thesis, we have $\hat{A} = \hat{\rho}_{\boldsymbol{q}} = \sum_{j=1}^{N} e^{-i\boldsymbol{q}\cdot\hat{\boldsymbol{r}}_j}$ e $\hat{B} = \hat{\rho}_{-\boldsymbol{q}} = \hat{A}^{\dagger} = \sum_{j=1}^{N} e^{i\boldsymbol{q}\cdot\hat{\boldsymbol{r}}_j}$. Thus to determine the correlation function, in the Monte Carlo calculation we evaluate $\rho_{\boldsymbol{q}}(\mathbf{R}_n) = \sum_{j=1}^{N} e^{-i\boldsymbol{q}\cdot\boldsymbol{r}_j^{(n)}}$ and $\rho_{-\boldsymbol{q}}(\mathbf{R}_0) = \sum_{j=1}^{N} e^{i\boldsymbol{q}\cdot\boldsymbol{r}_j^{(0)}}$.

Chapter 2

Quantum Dynamics

2.1 Neutron scattering

In the study of condensed matter information can be obtained on static and dynamic properties of systems through *scattering* of particles, such as neutrons, photons, or electrons. The wavelength of these particles must be comparable with the scale of the structures that one wishes to resolve, and their energy must be of the same order of magnitude as the analyzed excitations.

An important technique for analysis of condensed matter is the *neutron scattering*, as thermal neutrons, coming from nuclear reactors, ideally satisfy the conditions to study the properties of solids and liquids. In addition, since neutrons are neutral, they have a short-range interaction with nuclei, and thus unlike electrons, are able to deeply penetrate the material sample, thus showing position and momentum of nuclei, i.e. of atoms. These characteristics make thermal neutrons excellent probes for studying many-body systems, through elastic scattering to determine spatial distributions of the atoms inside the material sample, and through inelastic scattering to determine the dynamics of atoms in the system.

In a neutron scattering experiment, an incident beam of neutron probes is collimated and monochromatized by selecting those with an initial momentum $\hbar \boldsymbol{k}_0$ and an initial energy $\hbar^2 |\boldsymbol{k}_0|^2 / (2m_\mathrm{n})$ (m_n is the mass at rest of the neutron). The beam impinges on the target sample and is diffused in the surrounding space. An analyzer selects the diffused neutrons with final momentum $\hbar \boldsymbol{k}$ and final energy $\hbar^2 |\boldsymbol{k}|^2 / (2m_\mathrm{n})$. They are then received by a detector which measure the intensity of the beam exiting the analyzer. In this way we have a measure of the intensity of the diffused beam as a function of the momentum transferred $\hbar(\boldsymbol{k} - \boldsymbol{k}_0)$ and the energy transferred $\hbar^2 \left(|\boldsymbol{k}|^2 - |\boldsymbol{k}_0|^2 \right) / (2m_\mathrm{n})$ to the target sample, and thus we can obtain information on *structural* and *dynamical* properties of the analyzed physical system.

2.1.1 Theory of neutron scattering

To give a mathematical description of a neutron scattering experiment, we consider a system made up of N spinless and structureless particles, representing atoms of the physical system under examination, and a massive particle, the neutron, which we assume to interact with the atoms through the potential

$$V_{\text{int}} = \sum_{m=1}^{N} \phi(\boldsymbol{x} - \boldsymbol{r}_m), \tag{2.1}$$

where $\boldsymbol{x}$ is the position vector of the neutron, the *probe*, and $\{\boldsymbol{r}_1, \dots, \boldsymbol{r}_N\}$ are the position vectors of atoms. That interaction can be represented with a very good approximation by the *Fermi pseudopotential*

$$\phi(\boldsymbol{x} - \boldsymbol{r}) = \frac{2\pi\hbar^2}{m_{\text{n}}} b\, \delta(\boldsymbol{x} - \boldsymbol{r}), \tag{2.2}$$

where b is a phenomenological parameter, called *scattering length*, of the atomic nucleus.

The Hamiltonian operator that governs the system dynamics is

$$\hat{H}_{\text{tot}} = \hat{H} + \hat{T}_{\text{neutr}} + \hat{V}_{\text{int}}, \tag{2.3}$$

where $\hat{H}$ is the Hamiltonian operator of the target system constituted by atoms (that we suppose are of the same atomic element),

$$\hat{H} = \hat{T} + \hat{V} = \frac{1}{2m} \sum_{i=1}^{N} \hat{\boldsymbol{p}}_i^2 + \sum_{1 \le i < j \le N} v\big(\hat{\boldsymbol{r}}_i - \hat{\boldsymbol{r}}_j\big); \tag{2.4}$$

the second operator $\hat{T}_{\text{neutr}}$ represents the kinetic energy of the probe,

$$\hat{T}_{\text{neutr}} = \frac{1}{2m_{\text{n}}} \hat{\boldsymbol{p}}^2; \tag{2.5}$$

while the last term $\hat{V}_{\text{int}}$ is the potential operator that describes the probe-target interaction (see Eq. 2.1).

Since we suppose that the neutron interacts weakly with the sample, we are led to treat the interaction $\hat{V}_{\text{int}}$ as a weak perturbation to the operator

$$\hat{H}_0 = \hat{H} + \hat{T}_{\text{neutr}}, \tag{2.6}$$

that constitutes the dominant contribution to the dynamics of the system. We assume that, at an initial instant $t = 0$, the quantum state of the system composed by the neutron and the target $|\Psi_{\text{in}}\rangle$ consists of uncorrelated states of the neutron $\left|\varphi_{\boldsymbol{k}_0}\right\rangle \equiv |\boldsymbol{k}_0\rangle$ and of the target $|\psi_{\text{in}}\rangle$ ($\{|\boldsymbol{k}\rangle\}$ is the basis of momentum states). That is $|\Psi_{\text{in}}\rangle$ can be written as the (tensor) product

$$|\Psi_{\text{in}}\rangle = |\boldsymbol{k}_0\rangle\, |\psi_{\text{in}}\rangle\,. \tag{2.7}$$

We also assume that the neutron is free and that its wave function $\varphi_{\boldsymbol{k}_0}(\boldsymbol{x}) = \langle \boldsymbol{x} | \boldsymbol{k}_0 \rangle$ satisfies the periodic boundary conditions for a cubic box of volume V, i.e.

$$\varphi_{\boldsymbol{k}_0}(\boldsymbol{x}) = \frac{e^{i\boldsymbol{k}_0 \cdot \boldsymbol{x}}}{\sqrt{V}}, \tag{2.8}$$

and that $|\psi_{\mathrm{in}}\rangle$ is an eigenstate of $\hat{H}$ 2.4. The states of the neutron and target sample are uncorrelated, since we assume that before the scattering there is no interaction between them.

The state $|\Psi_{\mathrm{in}}\rangle$ 2.7 is an eigenstate of the unperturbed Hamiltonian $\hat{H}_0$ 2.6 and during the time evolution of the perturbed system $\hat{V}_{\mathrm{int}}$ causes transitions to the final eigenstates $|\Psi_{\mathrm{f}}\rangle$, which are all factorized as $|\Psi_{\mathrm{in}}\rangle$ in Eq. 2.7,

$$|\Psi_{\mathrm{f}}\rangle = |\boldsymbol{k}\rangle\,|\psi_{\mathrm{f}}\rangle\,, \tag{2.9}$$

where $\varphi_{\boldsymbol{k}}(\boldsymbol{x}) = \langle x | \boldsymbol{k} \rangle$ is still of the form 2.8 and represents a state in which the neutron momentum is well defined and is $\hbar\boldsymbol{k}$ and $|\psi_{\mathrm{f}}\rangle$ is again a eigenstate of $\hat{H}$. Then we consider the transition $|\Psi_{\mathrm{in}}\rangle \xrightarrow{t} |\Psi_{\mathrm{f}}\rangle$. Using standard relations from first-order time-dependent perturbation theory (the so-called *first Born approximation*) we find the probability that the transition will take place in a time t

$$P_{\left(|\Psi_{\mathrm{in}}\rangle \xrightarrow{t} |\Psi_{\mathrm{f}}\rangle\right)} = 4 \left| \langle \Psi_{\mathrm{f}} | \sum_{m=1}^{N} \phi(\hat{\boldsymbol{x}} - \hat{\boldsymbol{r}}_m)\, |\Psi_{\mathrm{in}}\rangle \right|^2 \frac{\sin^2\left(\frac{(E_{\mathrm{f}}^0 - E_{\mathrm{in}}^0)t}{2\hbar}\right)}{\left(E_{\mathrm{f}}^0 - E_{\mathrm{in}}^0\right)^2}, \tag{2.10}$$

where $E_{\mathrm{f}}^0 - E_{\mathrm{in}}^0$ is the energy difference between the two eigenstates of $\hat{H}_0$ involved in the transition. Note that

$$E_{\mathrm{f}}^0 - E_{\mathrm{in}}^0 = \frac{\hbar^2 |\boldsymbol{k}|^2}{2m_{\mathrm{n}}} + E_{\mathrm{f}} - \frac{\hbar^2 |\boldsymbol{k}_0|^2}{2m_{\mathrm{n}}} - E_{\mathrm{in}}, \tag{2.11}$$

where E_{f} and E_{in} are eigenvalues of the Hamiltonian $\hat{H}$ of the atom system. We introduce the notation

$$\hbar\omega \equiv \frac{\hbar^2 |\boldsymbol{k}|^2}{2m_{\mathrm{n}}} - \frac{\hbar^2 |\boldsymbol{k}_0|^2}{2m_{\mathrm{n}}}, \tag{2.12}$$

that represents the energy lost ($\omega > 0$) or gained ($\omega < 0$) by the neutron in the transition. If the time interval t is long enough, the following approximation is valid

$$\frac{\sin^2\left(\frac{(E_{\mathrm{f}} - E_{\mathrm{in}} - \hbar\omega)t}{2\hbar}\right)}{\left(E_{\mathrm{f}} - E_{\mathrm{in}} - \hbar\omega\right)^2} \simeq t\,\frac{\pi}{2\hbar}\,\delta(E_{\mathrm{f}} - E_{\mathrm{in}} - \hbar\omega). \tag{2.13}$$

We can write the probability of transition per unit of time as follows

$$\Pi_{(|\Psi_{\mathrm{in}}\rangle \to |\Psi_{\mathrm{f}}\rangle)} = \frac{2\pi}{\hbar} \left| \langle \Psi_{\mathrm{f}} | \sum_{m=1}^{N} \phi(\hat{\boldsymbol{x}} - \hat{\boldsymbol{r}}_m) |\Psi_{\mathrm{in}}\rangle \right|^2 \delta(E_{\mathrm{f}} - E_{\mathrm{in}} - \hbar\omega). \tag{2.14}$$

Now, the particular choice of the initial and final states involved in the transition determines the factorization of the matrix element present in Eq. 2.14; and thus we have

$$\langle \Psi_{\rm f}| \sum_{m=1}^{N} \phi(\hat{x} - \hat{r}_m) \, |\Psi_{\rm in}\rangle = \frac{1}{V} \int \mathrm{d}x \; e^{-i(k-k_0)\cdot x} \, \langle \psi_{\rm f}| \sum_{m=1}^{N} \phi(x - \hat{r}_m) |\psi_{\rm in}\rangle \, , \tag{2.15}$$

where the matrix element $\langle \psi_{\rm f}| \cdots |\psi_{\rm in}\rangle$ acts in the Hilbert space of the atom system. If we introduce the Fourier transform of the neutron–target interaction,

$$\tilde{\phi}(k) = \frac{1}{V} \int \mathrm{d}x \; e^{-ik\cdot x} \phi(x), \tag{2.16}$$

we have

$$\langle \Psi_{\rm f}| \sum_{m=1}^{N} \phi(\hat{x} - \hat{r}_m) \, |\Psi_{\rm in}\rangle = \tilde{\phi}(k - k_0) \, \langle \psi_{\rm f}| \sum_{m=1}^{N} e^{-i(k-k_0)\cdot \hat{r}_m} \, |\psi_{\rm in}\rangle \, . \tag{2.17}$$

Note that the previous expression depends solely on the transferred wave vector

$$q \equiv k_0 - k. \tag{2.18}$$

The operator$\sum_{m=1}^{N} e^{-iq\cdot\hat{r}_m}$ is called *density-fluctuation operator* and is usually indicated with $\hat{\rho}_q$. From here on, for reasons of convenience, we will use this notation. Note that $\hat{\rho}_q = \hat{\rho}^{\dagger}_{-q}$. If we sum on a complete orthonormal system of final states $\{|\psi_{\rm f}\rangle\}$ of the atom system (eigenstates of $\hat{H}$), we obtain the probability per unit of time for a transition from a state $|\Psi_{\rm in}\rangle$ to any state $|k\rangle$ in which the neutron has momentum $\hbar k$

$$\Pi_{\left(|\Psi_{\rm in}\rangle \xrightarrow{q,\omega} |k\rangle\right)} = \frac{2\pi}{\hbar} |\tilde{\phi}(-q)|^2 \sum_{\psi_{\rm f}} \left|\langle \psi_{\rm f}| \hat{\rho}_{-q} \, |\psi_{\rm in}\rangle\right|^2 \delta(E_{\rm f} - E_{\rm in} - \hbar\omega) \tag{2.19}$$

Now, we use the integral representation of the Dirac delta

$$\delta(E_{\rm f} - E_{\rm in} - \hbar\omega) = \frac{1}{2\pi\hbar} \int_{-\infty}^{+\infty} \mathrm{d}t \, e^{it[\hbar\omega - (E_{\rm f} - E_{\rm in})]/\hbar} \tag{2.20}$$

and we can write

$$\langle \psi_{\rm in}| \hat{\rho}_q \, |\psi_{\rm f}\rangle \; e^{-it(E_{\rm f} - E_{\rm in}) \, /\hbar} = \langle \psi_{\rm in}| \hat{\rho}_q(t) \, |\psi_{\rm f}\rangle \tag{2.21}$$

where we have used the Heisenberg representation of the operator $\hat{\rho}_q$ at time t

$$\hat{\rho}_q(t) \equiv e^{it\hat{H}/\hbar} \hat{\rho}_q \, e^{-it\hat{H}/\hbar}. \tag{2.22}$$

Using 2.21, decomposing the module of square matrix elements in Eq. 2.14 and using the identity resolution on the states $\{|\Psi_{\rm f}\rangle\}$, we obtain

$$\Pi_{\left(|\Psi_{\rm in}\rangle \xrightarrow{q,\omega} |k\rangle\right)} = \frac{2\pi}{\hbar^2} |\tilde{\phi}(-q)|^2 \frac{1}{2\pi} \int_{-\infty}^{+\infty} \mathrm{d}t \; e^{i\omega t} \, \langle \psi_{\rm in}| \hat{\rho}_q(t) \hat{\rho}_{-q} \, |\psi_{\rm in}\rangle \, . \tag{2.23}$$

Now we move from the average with respect to the pure state $|\Psi_{\rm in}\rangle$ to the thermal average on the initial states $\{|\psi_{\rm in}\rangle\}$ of the atom system at a temperature T. We multiply 2.23 for the Boltzmann statistical weight $p_{\psi_{\mathrm{in}}} = e^{-\beta E_{\mathrm{in}}}/Z$, where Z is the partition function $Z = \sum_{\psi_{\mathrm{in}}} e^{-\beta E_{\mathrm{in}}}$, and sum on the states $\{|\psi_{\mathrm{in}}\rangle\}$:

$$\begin{aligned} \Pi_{\left(|\boldsymbol{k}_0\rangle \xrightarrow{q,\omega} |\boldsymbol{k}\rangle\right)} &= \frac{2\pi}{\hbar^2}|\tilde{\phi}(-\boldsymbol{q})|^2 \frac{1}{2\pi}\int_{-\infty}^{+\infty} \mathrm{d}t\, e^{i\omega t} \sum_{\Psi_{\mathrm{in}}} \frac{e^{-\beta E_{\mathrm{in}}}}{Z} \langle\psi_{\mathrm{in}}|\,\hat{\rho}_{\boldsymbol{q}}(t)\hat{\rho}_{-\boldsymbol{q}}\,|\psi_{\mathrm{in}}\rangle = \\ &= \frac{2\pi}{\hbar^2}|\tilde{\phi}(-\boldsymbol{q})|^2 \frac{1}{2\pi}\int_{-\infty}^{+\infty} \mathrm{d}t\, e^{i\omega t} \left\langle \hat{\rho}_{\boldsymbol{q}}(t)\hat{\rho}_{-\boldsymbol{q}} \right\rangle_T , \end{aligned} \tag{2.24}$$

where $\langle\cdots\rangle_T$ denotes the thermal average, i.e. $\mathrm{Tr}\left(e^{-\beta\hat{H}}/Z\ldots\right) = \sum_{\Psi_{\mathrm{in}}} \langle\psi_{\mathrm{in}}|e^{-\beta\hat{H}}/Z\ldots|\psi_{\mathrm{in}}\rangle$.

We can rewrite Eq. 2.24, defining the *dynamic structure factor* for finite temperature T

$$S(\boldsymbol{q},\omega) = \frac{1}{2\pi N}\int_{-\infty}^{+\infty} \mathrm{d}t\, e^{\,i\omega t} \left\langle \hat{\rho}_{\boldsymbol{q}}(t)\hat{\rho}_{-\boldsymbol{q}} \right\rangle_T . \tag{2.25}$$

We thus have, slightly modifying the notation,

$$\Pi(\boldsymbol{q},\omega) = N\,\frac{2\pi}{\hbar^2}\,|\tilde{\phi}(-\boldsymbol{q})|^2\, S(\boldsymbol{q},\omega), \tag{2.26}$$

where $\Pi(\boldsymbol{q},\omega)$ is the probability per unit of time that the neutron will interact with the target system exchanging a momentum $\hbar\boldsymbol{q}$ and an energy $\hbar\omega$ while the sample is found at thermal equilibrium at temperature T.

If we introduce in Eq. 2.24 the explicit expression of the Fourier component of the Fermi pseudopotential 2.2

$$\tilde{\phi}(-\boldsymbol{q}) = \frac{1}{V}\frac{2\pi\hbar^2}{m_{\mathrm{n}}}\, b \tag{2.27}$$

that we note to be independent of $\boldsymbol{q}$, we obtain

$$\Pi(\boldsymbol{q},\omega) = \frac{N}{V^2}\,\frac{(2\pi)^3\hbar^2}{m_{\mathrm{n}}^2}\, b\, S(\boldsymbol{q},\omega). \tag{2.28}$$

Now, to compare these theoretical results with the experimental data, we introduce the physical quantity called *partial differential cross section* that is given by

$$\frac{\mathrm{d}^2\sigma}{\mathrm{d}\Omega\,\mathrm{d}\varepsilon} = \frac{\begin{array}{c}[\text{N of neutrons diffused per unit of time in a solid angle } \mathrm{d}\Omega \\ \text{in direction of } \boldsymbol{k} \text{ and with energies in } \mathrm{d}\varepsilon \text{ around } \hbar^2|\boldsymbol{k}|^2/(2m_{\mathrm{n}})]\end{array}}{[\text{total flux of incident neutrons with momentum } \hbar\boldsymbol{k_0}]\,\mathrm{d}\Omega\,\mathrm{d}\varepsilon} \tag{2.29}$$

We find that this is proportional to the probability $\Pi(\boldsymbol{q},\omega)$, according to

$$\frac{\mathrm{d}^2\sigma}{\mathrm{d}\Omega\,\mathrm{d}\varepsilon} = \frac{V^2 m_{\mathrm{n}}^2}{(2\pi)^3\hbar^3}\frac{|\boldsymbol{k}|}{|\boldsymbol{k}_0|}\Pi(\boldsymbol{q},\omega) \tag{2.30}$$

and thus in terms of $S(\boldsymbol{q},\omega)$ we have

$$\frac{\mathrm{d}^2\sigma}{\mathrm{d}\Omega\,\mathrm{d}\varepsilon} = N\frac{|\boldsymbol{k}|}{|\boldsymbol{k}_0|}\frac{b^2}{\hbar}S(\boldsymbol{q},\omega). \tag{2.31}$$

It is important to stress that, apart from kinematic factors ($\boldsymbol{k}_0$ and $\boldsymbol{k}$), the partial differential cross section depends on the scattering length b and the dynamic structure factor $S(\boldsymbol{q},\omega)$ of the atom system, that depends only on the quantum dynamics of the isolated system.

2.2 Dynamic Structure Factor

I present some properties of the dynamic structure factor at finite temperature, introduced in the previous section

$$S(\boldsymbol{q},\omega) = \frac{1}{2\pi N}\int_{-\infty}^{+\infty} \mathrm{d}t\, e^{i\omega t}\left\langle \hat{\rho}_{\boldsymbol{q}}(t)\hat{\rho}_{-\boldsymbol{q}}(0)\right\rangle_T . \tag{2.32}$$

Most of them can be found in various texts, e.g., Refs. [53–55]. Given an orthonormal set of eigenstates of the sample-system Hamiltonian $\hat{H}$ 2.4 $\{|\psi_n\rangle\}_n$ and the relative eigenvalues $\{E_n\}_n$, we can write the dynamic structure factor in the Lehmann representation [53] as

$$S(\boldsymbol{q},\omega) = \frac{1}{N}\sum_{n,m=0}^{\infty}\frac{e^{-\beta E_n}}{Z}\left|\langle\psi_m|\,\hat{\rho}_{-\boldsymbol{q}}\,|\psi_n\rangle\right|^2 \delta[\omega-(E_m-E_n)/\hbar]. \tag{2.33}$$

We can observe that, due to the presence of the Dirac delta, $S(\boldsymbol{q},\omega)$ is non-zero when $\hbar\omega$ has the values of the transition energies $E_m - E_n$. This confers to $S(\boldsymbol{q},\omega)$ a structure of peaks, which represent the probability of transition between the energy levels E_m and E_n. Furthermore, for each n, only those eigenstates $|\psi_m\rangle$ that have a non-zero overlap with the state $\hat{\rho}_{-\boldsymbol{q}}\,|\psi_n\rangle$, contribute to the response of the atom sample system.

2.2.1 Mathematical Properties

Here I present useful mathematical properties of $S(\boldsymbol{q},\omega)$. Since the Hamiltonian of the sample system 2.4 is symmetric under time reversal transformation, its eigenfunctions can be chosen real, and since the operator $\hat{\rho}_q$ is diagonal with respect to the position basis, then the following identity holds

$$\left|\langle\psi_m|\hat{\rho}_{\boldsymbol{q}}|\psi_n\rangle\right|^2 = \left|\langle\psi_m|\hat{\rho}_{-\boldsymbol{q}}|\psi_n\rangle\right|^2. \tag{2.34}$$

Using this identity in the expression 2.33, we obtain a symmetry property for the dynamic structure factor

$$S(\boldsymbol{q},\omega) = S(-\boldsymbol{q},\omega), \tag{2.35}$$

i.e. the invariance for inversion of the transferred momentum.

Observing Eq. 2.33 one can note that $S(\boldsymbol{q},\omega)$ is real and non-negative, i.e.

$$[S(\boldsymbol{q},\omega)]^* = S(\boldsymbol{q},\omega) \quad \text{and} \quad S(\boldsymbol{q},\omega) \geq 0. \tag{2.36}$$

Another property can be easily derived directly from the eigenstate representation of $S(\boldsymbol{q},\omega)$ 2.33:

$$S(\boldsymbol{q},\omega) = e^{\hbar\beta\omega} S(-\boldsymbol{q},-\omega), \tag{2.37}$$

and using the symmetry property 2.35 we obtain

$$S(\boldsymbol{q},\omega) = e^{\hbar\beta\omega} S(\boldsymbol{q},-\omega), \tag{2.38}$$

This is called the *principle of detailed balance.*

2.2.2 Sum Rules

Despite the fact that the dynamic structure factor is a many-body observable, it is possible to derive the expressions of some of its frequency moments, i.e. integrals of the form

$$\int_{-\infty}^{+\infty} \mathrm{d}\omega\, \omega^n\, S(\boldsymbol{q},\omega). \tag{2.39}$$

Here, we consider the zero moment and the first moment ($n = 0, 1$), that are useful to determine the dynamic structure factor starting from QMC simulation data. Integrating the expression of $S(\boldsymbol{q},\omega)$ 2.32 on ω we obtain

$$\int_{-\infty}^{+\infty} \mathrm{d}\omega\, S(\boldsymbol{q},\omega) = \frac{1}{N} \left\langle \hat{\rho}_{\boldsymbol{q}}(t)\hat{\rho}_{-\boldsymbol{q}} \right\rangle_T \equiv S(\boldsymbol{q}). \tag{2.40}$$

The function $S(\boldsymbol{q})$ is the static structure factor of the system; it describes the spatial distribution of the atoms and can easily be determined during the QMC simulations.

As regards the first moment, we see that using the Lehmann representation of $S(\boldsymbol{q},\omega)$ 2.33 we can write

$$\int_{-\infty}^{+\infty} \mathrm{d}\omega\, \omega\, S(\boldsymbol{q},\omega) = \frac{1}{N} \sum_{n,m=0}^{\infty} \frac{e^{-\beta E_n}}{Z} \frac{E_m - E_n}{\hbar} \left| \langle \psi_m | \hat{\rho}_{-\boldsymbol{q}} | \psi_n \rangle \right|^2. \tag{2.41}$$

By exploiting the time-reversal symmetry property 2.34, one can easily obtain that (see, e.g., Ref. [53])

$$\frac{1}{2N\hbar} \left\langle \left[\left[\hat{\rho}_{\boldsymbol{q}}, \hat{H} \right], \hat{\rho}_{-\boldsymbol{q}} \right] \right\rangle_T = \frac{1}{N\hbar} \sum_{n,m=0}^{\infty} \frac{e^{-\beta E_n}}{Z} (E_m - E_n) \left| \langle \psi_m | \hat{\rho}_{-\boldsymbol{q}} | \psi_n \rangle \right|^2. \tag{2.42}$$

This expression can be simplified using the Heisenberg equation of motion

$$\left[\hat{\rho}_{\boldsymbol{q}}, \hat{H} \right] = i\hbar \frac{\partial \hat{\rho}_{\boldsymbol{q}}(t)}{\partial t} = \hbar \boldsymbol{q} \cdot \hat{\boldsymbol{j}}_{\boldsymbol{q}}\ , \tag{2.43}$$

where the operator $\hat{\boldsymbol{j}}_{\boldsymbol{q}}$ is the Fourier transform of the local current operator and is defined by

$$\hat{\boldsymbol{j}}_{\boldsymbol{q}} = \frac{1}{2m} \sum_{i=1}^{N} \left(\hat{\boldsymbol{p}}_i e^{-i\boldsymbol{q}\cdot\hat{\boldsymbol{r}}_i} + e^{-i\boldsymbol{q}\cdot\hat{\boldsymbol{r}}_i} \hat{\boldsymbol{p}}_i \right). \tag{2.44}$$

One can easily demonstrate that

$$\left[\hat{j}_{q}, \hat{\rho}_{-q}\right] = \frac{\hbar \boldsymbol{q}}{m} N. \tag{2.45}$$

Thus, from Eq. 2.42 using Eqs. 2.43 and 2.45 we have

$$\frac{1}{2N\hbar} \left\langle \left[\left[\hat{\rho}_{q}, \hat{H}\right], \hat{\rho}_{-q}\right] \right\rangle_T = \frac{\hbar |\boldsymbol{q}|^2}{2m}. \tag{2.46}$$

Hence, finally, the first moment of $S(\boldsymbol{q}, \omega)$ is

$$\int_{-\infty}^{+\infty} \mathrm{d}\omega \, \omega \, S(\boldsymbol{q}, \omega) = \frac{\hbar |\boldsymbol{q}|^2}{2m}. \tag{2.47}$$

2.3 Static Density Response Function

An important physical quantity strictly linked to $S(\boldsymbol{q}, \omega)$ is the *static density–density response function* $\chi(\boldsymbol{q})$. For a bibliographical reference regarding the following discussion see, for example, the Ref. [55]. Formally $\chi(\boldsymbol{q})$ is the zero frequency limit ($\omega \to 0$) of the Fourier transform $\chi(\boldsymbol{q}, \omega)$ of the *density response function* $\chi(\boldsymbol{q}, t)$,

$$\chi(\boldsymbol{q}, \omega) = \frac{1}{2\pi} \int_{-\infty}^{+\infty} \mathrm{d}t \, e^{i\omega t} \chi(\boldsymbol{q}, t). \tag{2.48}$$

$\chi(\boldsymbol{q}, t)$ is defined by

$$\chi(\boldsymbol{q}, t) \equiv -i \, \Theta(t) \, \frac{1}{V} \left\langle \left[\hat{\rho}_q(t), \hat{\rho}_{-q}(0)\right] \right\rangle, \tag{2.49}$$

where $\Theta(t)$ is the Heaviside step function, V is the volume of the system and the brackets indicate the commutator $\left[\hat{A}, \hat{B}\right] \equiv \hat{A}\hat{B} - \hat{B}\hat{A}$.

The function $\chi(\boldsymbol{q}, t)$ is also called the *retarded* response function, since it expresses the system response at time t to an external perturbation that occurred at a prior time $t = 0$. $\chi(\boldsymbol{q}, t)$ is defined and derived in the field of linear response theory [55].

The Fourier transform $\chi(\boldsymbol{q}, \omega)$ of $\chi(\boldsymbol{q}, t)$ can be expressed in terms of the eigenstates $\{\psi_n\}_n$ of the system Hamiltonian $\hat{H}$ 2.4, i.e. using the Lehman representation, as done for the expression of $S(\boldsymbol{q}, \omega)$ 2.33. We have (here η is a positive infinitesimal, that ensures the adiabatic switching on of the external perturbation and must be set to zero at the end of calculation)

$$\chi(\boldsymbol{q}, \omega + i\eta) = \frac{1}{V} \sum_{n,m=0}^{\infty} \frac{e^{-\beta E_n}}{Z} \left|\left\langle \psi_m \right| \hat{\rho}_{-q} \left| \psi_n \right\rangle\right|^2 \frac{1 - e^{-\beta(E_m - E_n)}}{\omega + i\eta - (E_m - E_n)}. \tag{2.50}$$

where η is a positive infinitesimal. Using the *Plemelj formula* [56]

$$\frac{1}{x \pm i\eta} \xrightarrow{\eta \to 0} \mathrm{P}\left(\frac{1}{x}\right) \mp i\pi \, \delta(x) \tag{2.51}$$

in 2.50 (P(…) indicates the principal part), we obtain that the imaginary part of $\chi(\boldsymbol{q},\omega)$ is given by

$$\mathrm{Im}\,\chi(\boldsymbol{q},\omega) = -\pi\,\frac{1}{V}\Big(1-e^{-\beta\omega}\Big)\sum_{n,m=0}^{\infty}\frac{e^{-\beta E_n}}{Z}\left|\langle\psi_m|\,\hat{\rho}_{-q}\,|\psi_n\rangle\right|^2\delta[\hbar\omega-(E_m-E_n)]. \tag{2.52}$$

Comparing this equation with the analogous expression of $S(\boldsymbol{q},\omega)$ 2.33 we obtain a relation that directly links $\chi(\boldsymbol{q},\omega)$ to $S(\boldsymbol{q},\omega)$

$$\mathrm{Im}\,\chi(\boldsymbol{q},\omega) = -\pi\,\rho\,\Big(1-e^{-\beta\omega}\Big)\,S(\boldsymbol{q},\omega), \tag{2.53}$$

where $\rho = N/V$ is the atom density.

From the equations 2.52 and 2.50 we obtain the spectral relation (strictly linked to the Kramers-Kronig dispersion relations)

$$\mathrm{Re}\,\chi(\boldsymbol{q},\omega) = -\frac{1}{\pi}\,\mathrm{P}\int_{-\infty}^{+\infty}\mathrm{d}\omega'\,\frac{\mathrm{Im}\,\chi(\boldsymbol{q},\omega')}{\omega-\omega'} \tag{2.54}$$

Inserting the expression 2.53 in this equation and using the principle of detailed balance 2.38 we obtain

$$\chi(\boldsymbol{q},\omega) = 2\,\rho\int_{-\infty}^{+\infty}\mathrm{d}\omega'\,\frac{\omega'\,S(\boldsymbol{q},\omega')}{\omega^2-\omega'^2}. \tag{2.55}$$

Lastly, we obtain the important expression of the static density response function $\chi(\boldsymbol{q})$ (zero-frequency limit of $\chi(\boldsymbol{q},\omega)$) in terms of the dynamic structure factor $S(\boldsymbol{q},\omega)$:

$$\chi(\boldsymbol{q}) \equiv \chi(\boldsymbol{q},\omega=0) = -2\,\rho\int_{-\infty}^{+\infty}\mathrm{d}\omega'\,\frac{S(\boldsymbol{q},\omega')}{\omega'}. \tag{2.56}$$

I.e. $\chi(\boldsymbol{q})$ is the -1-*th moment* ($n=-1$) of $S(\boldsymbol{q},\omega)$, apart from the constant multiplicative factor $-2\,\rho$, as we can see comparing 2.56 with the definition of n-th moment 2.39. This relation was used to determine $\chi(\boldsymbol{q})$ for the quantum systems investigated in the two research projects presented in Chapters 3 and 4.

$\chi(\boldsymbol{q})$ represents the static response of the system in terms of density induced by an external perturbation that oscillates in space. More precisely, if we apply a static external potential of the form

$$v_{\mathrm{ext}}(\boldsymbol{r}) = 2\,v_q\,\cos(\boldsymbol{q}\cdot\boldsymbol{r}), \tag{2.57}$$

with a wave vector $\boldsymbol{q}$, that induces a density modulation around the average value ρ, we find that such modulation of density is given by

$$\rho(\boldsymbol{r}) = 2\,\rho_q\,\cos(\boldsymbol{q}\cdot\boldsymbol{r}), \tag{2.58}$$

where

$$\rho_q = \chi(\boldsymbol{q})\,v_q + C_3\,v_q^3 + \dots\,. \tag{2.59}$$

From this equation we can see that $\chi(\boldsymbol{q})$ represents the density static linear response at wave vector $\boldsymbol{q}$.

2.4 Correlation Functions

2.4.1 Real time correlation functions

Given a quantum many-body system, such as for example a quantum liquid, the real-time correlation function for two generic operators $\hat{A}$ and $\hat{B}$ is defined by

$$C_{\mathrm{AB}}(t,t') \equiv \left\langle \hat{A}(t)\,\hat{B}(t') \right\rangle . \tag{2.60}$$

where $\hat{A}(t)$ and $\hat{B}(t')$ are the time evolved operators of $\hat{A}$ and $\hat{B}$ until the times t and t' respectively, according to the (real-time) Heisenberg representation

$$\hat{X}(t) \equiv e^{it\hat{H}/\hbar}\,\hat{X}\,e^{-it\hat{H}/\hbar}. \tag{2.61}$$

In 2.60 $\langle ... \rangle$ represents for T > 0 the thermal average, i.e. $\mathrm{Tr}\left(e^{-\beta\hat{H}}/Z\,...\right)$, or for T $= 0$ the quantum expectation value with respect to the ground state of the system $|\Psi_0\rangle$, i.e. $\langle \Psi_0|...|\Psi_0\rangle$.

To illustrate the physical meaning of the correlation functions, consider as an example, $C_{\rho(\boldsymbol{r})\rho(\boldsymbol{r}')}(t,t')$, the correlation of the *local density* operators

$$\hat{A} = \hat{\rho}(\boldsymbol{r}) \equiv \sum_{i=1}^{N} \delta(\boldsymbol{r} - \hat{\boldsymbol{r}}_i) \quad \mathrm{e} \quad \hat{B} = \hat{\rho}(\boldsymbol{r}'). \tag{2.62}$$

$C_{\rho(\boldsymbol{r})\rho(\boldsymbol{r}')}(t,t')$, called *density–density correlation function*, is proportional to the probability to find particles in position $\boldsymbol{r}$ at the time t and particles in position $\boldsymbol{r}'$ at the time t'.

In some research projects presented in this thesis we are interested in the dynamics of the many-body system in terms of wave-vector components of the density, and therefore in the *density-fluctuation–density-fluctuation correlation function* $C_{\rho_{\boldsymbol{q}}\rho_{-\boldsymbol{q}}}(t,t')$, that is the Fourier transform of $C_{\rho(\boldsymbol{r})\rho(\boldsymbol{r}')}(t,t')$, and defined by 2.60 using two *density-fluctuation operators* at opposed wave vectors

$$\hat{A} = \hat{\rho}_{\boldsymbol{q}} \equiv \sum_{j=1}^{N} e^{-i\boldsymbol{q}\cdot\hat{\boldsymbol{r}}_j} \quad \text{and} \quad \hat{B} = \hat{A}^{\dagger} = \hat{\rho}_{-\boldsymbol{q}}\,, \tag{2.63}$$

where $\left\{\hat{\boldsymbol{r}}_j\right\}_{j=1}^{N}$ are the position operators of the particles in the many-body system.

At finite temperature, if the Hamiltonian of the system is time-independent, thanks to the cyclic property of the trace and the commutativity of $e^{-it\hat{H}/\hbar}$ with $e^{-\beta\hat{H}}/Z$, the correlation function depends only on the time difference $t - t'$, thus it is customary to write, in a more convenient way,

$$C_{\mathrm{AB}}(t) \equiv \left\langle \hat{A}(t)\,\hat{B} \right\rangle . \tag{2.64}$$

Similarly, for the density-fluctuation correlation function we may use the notation $C_{\rho_{\boldsymbol{q}}\rho_{-\boldsymbol{q}}}(t) \equiv \left\langle \hat{\rho}_{\boldsymbol{q}}(t)\,\hat{\rho}_{-\boldsymbol{q}} \right\rangle$. Furthermore, $C_{\rho_{\boldsymbol{q}}\rho_{-\boldsymbol{q}}}(t)$ is customary called *intermediate scattering function* and here on we will denote it as $F(\boldsymbol{q},t)$.

2.4.2 Imaginary time correlation functions

In the same way, we can define analogous correlation functions, but in imaginary time. In place of the unitary time evolution operator $e^{-it\hat{H}/\hbar}$ we use an analogous operator, that is not unitary: the imaginary time evolution operator $e^{-\tau\hat{H}/\hbar}$. The transformation that expresses the passage from real time to imaginary time $it \rightarrow \tau$ is called *Wick rotation*. The imaginary-time correlation function is defined by

$$C^{\mathrm{i}}_{\mathrm{AB}}(\tau,\tau') \equiv \left\langle \hat{A}(\tau)\,\hat{B}(\tau')\right\rangle \tag{2.65}$$

where $\hat{A}(\tau)$ and $\hat{B}(\tau')$ are the operators $\hat{A}$ and $\hat{B}$ evolved in imaginary time until τ and τ' respectively, according to the relation

$$\hat{X}(\tau) \equiv e^{\tau\hat{H}/\hbar}\,\hat{X}\,e^{-\tau\hat{H}/\hbar} \tag{2.66}$$

and, as well as in the case of real time, the parentheses $\langle\ldots\rangle$ represent the thermal average or the expectation value with respect to the ground state.

At finite temperature, as well as above, if the Hamiltonian $\hat{H}$ is time-independent, for the cyclic property of the trace we have $C^{\mathrm{i}}_{\mathrm{AB}}(\tau,\tau') = C^{\mathrm{i}}_{\mathrm{AB}}(\tau-\tau')$ and thus we define

$$C^{\mathrm{i}}_{\mathrm{AB}}(\tau) \equiv \left\langle \hat{A}(\tau)\,\hat{B}\right\rangle . \tag{2.67}$$

Still using the cyclic property of the trace, the so-called Kubo-Martin-Schwinger (KMS) relation [57, 58] is derived for the correlation functions at $T > 0$:

$$C^{\mathrm{i}}_{\mathrm{AB}}(\tau-\tau') = C^{\mathrm{i}}_{\mathrm{BA}}(\hbar\beta-(\tau-\tau')). \tag{2.68}$$

Regarding the *imaginary-time scattering function* $C^{i}_{\rho_q\rho_{-q}}(\tau)$, that will hereafter be denoted, more briefly, with $F(\boldsymbol{q},\tau)$, we have

$$F(\boldsymbol{q},\tau) \equiv C^{\mathrm{i}}_{\rho_q\rho_{-q}}(\tau) = \left\langle \rho_{\boldsymbol{q}}(\tau)\,\rho_{-\boldsymbol{q}}\right\rangle . \tag{2.69}$$

Using the identity 2.34 derived from the time-reversal invariance of the Hamiltonian $\hat{H}$, we obtain the following symmetry of $F(\boldsymbol{q},\tau)$ with respect to the wave-vector reversal

$$F(\boldsymbol{q},\tau) = \left\langle \rho_{\boldsymbol{q}}(\tau)\,\rho_{-\boldsymbol{q}}\right\rangle = \left\langle \rho_{-\boldsymbol{q}}(\tau)\,\rho_{\boldsymbol{q}}\right\rangle = F(-\boldsymbol{q},\tau). \tag{2.70}$$

The KMS property 2.68 for $F(\boldsymbol{q},\tau)$ is

$$F(\boldsymbol{q},\tau) = F(-\boldsymbol{q},\hbar\beta-\tau). \tag{2.71}$$

Therefore, using also Eq. 2.70 we obtain the property for $F(\boldsymbol{q},\tau)$

$$F(\boldsymbol{q},\tau) = F(\boldsymbol{q},\hbar\beta-\tau). \tag{2.72}$$

This implies that $F(\boldsymbol{q},\tau)$ is symmetric with respect to $\tau = \frac{\hbar\beta}{2}$.

2.5 Analytic continuation and inversion problem

The quantum Monte Carlo (QMC) methods, like the PIMC and PIGS, presented in the first chapter, allow for calculating imaginary time correlation functions, defined in the previous section,

$$C^{\mathrm{i}}_{\mathrm{AB}}(\tau) = \left\langle e^{\hat{H}\tau}\hat{A}e^{-\hat{H}\tau}\hat{B}\right\rangle . \tag{2.73}$$

From this point on, we will denote $C^{\mathrm{i}}_{\mathrm{AB}}(\tau)$, more briefly, with $f(\tau)$.

Typically, a QMC simulation evaluates a correlation function $f(\tau)$ in discrete imaginary times $\{\tau_i\}$, $i = 1, \dots, N_\tau$, i.e. it yields a finite set of values

$$\mathcal{F} \equiv \{f_1, f_2, \dots, f_{N_\tau}\}. \tag{2.74}$$

In general, $\mathcal{F}$ is obtained through a large number of QMC estimates of $f(\tau)$, each affected by statistical noise, and those calculations are used to determine the statistical uncertainties associated with $\mathcal{F}$

$$\left\{\sigma_{f_0}, \sigma_{f_1}, \dots, \sigma_{f_{N_\tau}}\right\}. \tag{2.75}$$

These data can be used to derive the unknown spectral function $s(\omega)$ from the integral equation

$$f(\tau) = \int_{-\infty}^{+\infty} \mathrm{d}\omega\, K(\tau,\omega)\, s(\omega) \tag{2.76}$$

where, e.g. with the dynamic structure factor $s(\omega) = S(\boldsymbol{q},\omega)$ and the imaginary-time scattering function $f(\tau) = F(\boldsymbol{q},\tau)$ at finite temperature, the kernel K is $K(\tau,\omega) = e^{-\omega\tau}$.

The sum rules often provide additional assistance, either imposing exact restrictions on $s(\omega)$, or allowing to perform additional measurements in the QMC simulations,

$$\mathcal{C} \equiv \{\dots, c_{-1}, c_0, c_1, \dots, c_n, \dots\}, \tag{2.77}$$

where c_n is the estimate of the n-th moment of the spectral function $s(\omega)$

$$\langle\omega^n\rangle \equiv \int_{-\infty}^{+\infty} \mathrm{d}\omega\, \omega^n\, s(\omega). \tag{2.78}$$

For example, c_0 is an estimate of $\left\langle\hat{A}\,\hat{B}\right\rangle$ that could easily be obtained in the QMC simulations together with its statistical uncertainty.

The determination of $s(\omega)$ from $f(\tau)$ is an *inverse problem*. I explain here the concept of inverse problem. We suppose that we have a mathematical problem that describes a physical phenomenon. Generally, the description of the system is given in terms of—ordinary, in partial derivatives, and/or integral—equations that contain certain parameters. The analysis of a given physical phenomenon through a mathematical relation may be classified in three distinct types of problems:

1. the *direct problem*, given the inputs and parameters of the model which describe the physical phenomenon, we find the outputs;

2. the *reconstruction problem*, given the parameters and outputs of the model, we determine the inputs that lead to those outputs;

3. the *identification problem*, given the inputs and outputs of the model, we find the parameters that are consistent with the relation between the inputs and the outputs.

A problem of the first type is called a *direct problem*, because it is oriented according a *cause–effect* sequence (from input and parameters to outputs). In this sense, the problems of the second and the third type are called *inverse problems*, since they consist in determining unknown causes (the inputs and/or the parameters) from known effects (the outputs). In our context, an example of a direct problem would be the determination of the correlation function $f(\tau)$ (the outputs) starting with "known" data of the spectral function $s(\omega)$ (the inputs) by means a direct computation (an integration). The determination of $s(\omega)$ (the inputs) from a QMC estimate of $f(\tau)$ (the outputs) is a problem of the second type, whilst, for example, the determination of the kernel $K(\tau, \omega)$, or some of its parameters such as the temperature T, would be a problem of the third type.

A mathematical modeling of many different inverse problems can be carried out, in a unified way, using an operator formalism. Consider the following notations:

X	input-value space or *model space*
Y	output-value space or *data space*
P	*parameter space* of model system
A_p	linear or nonlinear operator from X in Y associated with $p \in P$

In the majority of cases, X and Y are separable Hilbert spaces with finite or infinite dimensions and A_P is a compact operator. With this notation, we can reformulate the three types of problems in the following way:

1. given $x \in X$ and $p \in P$, we determine $y = A_P(x)$

2. given $y \in Y$ and $p \in P$, we resolve the equation

$$A_P(x) = y, \qquad x \in X \tag{2.79}$$

3. given $y \in Y$ and $x \in X$, we determine $p \in P$ such that $A_P(x) = y$.

In some simple cases, the inverse problem can be formally transformed into a direct problem. For example, if A_p is an invertible linear operator and its inverse operator is known, then the problem is resolved by $x = A_p^{-1}(y)$. In these cases as well, the explicit determination of the inverse operator is not useful if the output y is not in the domain of definition of A_p^{-1}. This situation is frequent since the outputs, whether experimental or resulting from a numerical simulation, are affected by statistical uncertainty.

Before continuing, we will explain the concept of *ill-posed problem*. This concept was introduced for the first time by the mathematician Hadamard in 1923 in the context of Cauchy problems [59]. He defined such a Cauchy problem as *well-posed* if, and only if, for all Cauchy data there is a unique solution depending continuously on the data; otherwise the problem is *ill-posed*.

We present the same concept with a operator formalism. We introduce the following definition.

Definition. Given the operator $A : X \to Y$, the inverse operatorial equation

$$A(x) = y \tag{2.80}$$

is *well-posed* if it satisfies the following conditions, called Hadamard conditions:

1. $A(x) = y$ has a solution $x \in X$ for every $y \in Y$; (*existence*)
2. the solution x is determined in a unique way; (*uniqueness*)
3. the inverse operator A^{-1} is continuous. (*stability*)

If at least one of the Hadamard conditions is not satisfied, it is said that the operatorial equation is *ill-posed* .

Even if the inverse of the compact operator exists, it cannot be continuous unless the spaces X and Y have finite dimensions.

Inverse problems principally present two difficulties. First, the problems are often ill-posed due to the fact that the operator A_P is *smoothing*. A term that, in this context, means that the result of the operation $A_P(x)$ is *more regular* than x, in the sense that the details are smoothed in the operation. This does not mean that the details cannot be reconstructed (in many cases they can), but rather that the reconstruction must go against this smoothing. The result is that often the solution is not unique. Different inputs give rise to outputs compatible among each other. Secondly, often the output y comes from experiments or numerical simulations, and therefore is discretized and affected by an error ε. In that case, it is important to have a statistical description of the error, through the knowledge of the probability distribution $\rho_\varepsilon(y)$.

In this dissertation we deal with one of the more important and widely known inverse problems: the *Fredholm integral equation of the first kind*, that, on a normed functional space of functions $x(\omega)$, is defined as

$$y(\tau) = \int_\Omega \mathrm{d}\omega \, K(\tau, \omega) \, x(\omega), \tag{2.81}$$

where $K(\tau, \omega)$ is the integral kernel of the operator A and Ω is a simply connected subset of $\mathbb{R}^n$. To be more precise, when the output data $y(\tau)$ have a statistical uncertainty ε, in place of Eq. 2.81 we have the approximate equation

$$y_\varepsilon(\tau) \simeq \int_\Omega \mathrm{d}\omega \, K(\tau, \omega) \, x(\omega). \tag{2.82}$$

Therefore it is more proper to say that we are searching for solutions that are compatible with the data $y_\varepsilon(\tau)$.

We consider as an example of an ill-posed problem the numerical inversion of the *Laplace transform*

$$y(\tau) = \int_0^{+\infty} \mathrm{d}\omega \, e^{-\tau\omega} x(\omega). \tag{2.83}$$

This is a Fredholm integral equation of the first kind 2.81 with kernel $K(\tau, \omega) = \theta(\omega)\, e^{-\tau\omega}$. One of the reasons ill-posedness of this problem is that the kernel $K(\tau, \omega)$ is a decreasing exponential on ω. Therefore it strongly attenuates $x(\omega)$ as ω increases, thus making it more difficult to reconstruct $x(\omega)$. At theoretical level, an exact formula exists to invert the Laplace transform the *Post's inversion formula*. It establishes that the function $x(\omega)$, continuous on $[0, \infty)$ and satisfying the condition $\sup_{\omega>0} |x(\omega)|\, e^{-b\omega} < \infty$, $b > 0$, can be derived from $y(\tau)$ as

$$x(\omega) = \lim_{k\to\infty} \frac{(-1)^k}{k!} \left(\frac{k}{\omega}\right)^{k+1} y^{(k)}\left(\frac{k}{\omega}\right), \tag{2.84}$$

for $\omega > 0$, where $y^{(k)}$ denotes the k-th derivative of $y(\tau)$. This formula does not provide a practical method to invert the transform, but illustrates why this problem is ill-posed. The inversion formula requires to determine derivatives of arbitrary large orders. However they cannot be computed with data affected by statistical uncertainty and only known on a discrete set of values of τ.

A simpler and intuitive way to understand why the problem is ill-posed is by making an example. Consider a spectral function given by the sum of two Dirac deltas, e.g.

$$x_1(\omega) = \delta(\omega - \omega_0) + x_1\, \delta[\omega - (\omega_0 + \Delta\omega_1)], \tag{2.85}$$

with $x_1, \omega_0, \Delta\omega_1 > 0$, we easily obtain for $y(\tau)$

$$y_1(\tau) = e^{-\tau\omega_1} + x_1\, e^{-\tau(\omega_1 + \Delta\omega)}. \tag{2.86}$$

Then the ratio of the contributes to $y(\tau)$ of the two deltas is $x_1 e^{-\tau\Delta\omega_1}$, i.e. the second delta yields a contribute exponentially smaller than the first one. Therefore, if a second spectral function that, for example, differs from the first only in the second delta, e.g.

$$x_2(\omega) = \delta(\omega - \omega_0) + x_2 \delta[\omega - (\omega_0 + \Delta\omega_2)], \tag{2.87}$$

with $x_2, \Delta\omega_2 > 0$, the two spectral functions will have an exponentially small difference, even if x_2 (and/or $\Delta\omega_2$) significantly differ from x_1 (and/or $\Delta\omega_1$); in other words, they are exponentially indistinguishable, if the data on $y(\tau)$ are affected by statistical error.

2.6 Inversion Methods

In this section we briefly present some of the most commonly used numerical methods to deal with the ill-posed problem of the inversion of Eq. 2.76: the maximum entropy method (MEM) and the average spectrum method (ASM).

2.6.1 MEM

The maximum entropy method (MEM) [16] allows for determining the most probable spectral function $s(\omega)$ consistent with the data $\mathcal{F}$, among a large number of possibilities. This method is based on Bayesian inference. As mentioned above, the known data $\mathcal{F}$ are a finite and discrete set of values and we search for a spectral function that is also valued at discrete points $\{\omega_j\}_j$, thus it is a set of values $\mathcal{S} = \{s_j\}_j$, where $s_j = s(\omega_j)$. The MEM selects a solution that maximizes the probability to have the solution set $\mathcal{S}$ given the set of data $\mathcal{F}$, known as a posteriori probability [60, 61],

$$P(\mathcal{S} \mid \mathcal{F}) \propto \exp(\alpha S - \chi^2/2). \tag{2.88}$$

χ^2 is the usual sum of squares of the deviation from the data

$$\chi^2 = \sum_{j,k} \left(f_j - \sum_l K_{jl} s_l \right) [C^{-1}]_{jk} \left(f_k - \sum_l K_{kl} s_l \right), \tag{2.89}$$

where C_{ji} is the covariance matrix

$$C_{jk} = \frac{1}{M(M-1)} \sum_{l=1}^{M} \left(\langle f_j \rangle - f_j^{(l)} \right) \left(\langle f_k \rangle - f_k^{(l)} \right), \tag{2.90}$$

M being the number of measurements; K_{jl} is the matrix associated to the integral kernel $K(\tau, \omega)$. S is the information entropy and its form is given by

$$S = \sum_i \left(s_i - m_i - s_i \log\left(\frac{s_i}{m_i} \right) \right). \tag{2.91}$$

In this formula, the entropy is measured with respect to the default model $\{m_i\}_i$, that contains a priori information on the solution and α is a positive regularization parameter.

The solution obtained in this way is still influenced by the parameter α, that can be interpreted as a regularization parameter that controls the attenuation of the details of the solution. Large values of α lead to a result determined principally by the entropy, and thus, by the default model. Small values of α, on the other hand, lead to a solution determined principally by χ^2 and therefore, to a greater agreement with the data.

Various methods have been developed to optimally set the parameter α. One of the most accepted is the Bryan method [62].

It is recognized that the MEM approach often fails when there are many spectral characteristics close in frequency space. For example, in Ref. [63] the author shows that the MEM with the Bryan method does not succeed in reproducing the peak structure in the spectral function of ^{4}He.

2.6.2 ASM

The average spectrum method (ASM) [17] is based on the Bayesian approach like the MEM, but considers only a priori knowledge, without making other additional assumptions. As for the MEM, the purpose is to maximize the entropy of a distribution under the restrictions resulting from a priori knowledge. Instead of maximizing the entropy of the spectral function itself, the ASM maximizes the entropy of the multidimensional probability distribution of spectral functions constituted by the a posteriori probability.

The a posteriori probability is made up of a likelihood function and a weakly constraining probability function

$$P_{pr}(s) = \delta\big(\textstyle\sum_i s_i - c_0\big) \prod_i \Theta(s_i) \tag{2.92}$$

that assigns equal probabilities to all the functions that satisfy the non-negativity and the zero moment sum rule (c_0 is the zero moment of $s(\omega)$, i.e. its integral on the whole domain).

In the ASM, instead of taking only the maximum, that could overestimate the data, the final spectral function is obtained from the average spectral function on a posteriori probability distribution. The solution is the following

$$\bar{s} = \frac{\int ds\, s\, P(s \mid \bar{f})}{\int ds\, P(s \mid \bar{f})}. \tag{2.93}$$

The procedure of averaging would protect from overestimation of the data. But if the a posteriori probability has different peaks, that have the same weight, the average would become more questionable.

As documented in the literature, the average spectral function is very effective for spin lattice models [64]. Only recently the ASM method has been applied to realistic systems like quantum liquids [65].

2.7 The GIFT inversion method

2.7.1 Description of the method

In the research projects in which we studied the dynamical properties, through the extraction of the dynamical structure factor $S(\boldsymbol{q}, \omega)$ from computed data on the imaginary-time intermediate scattering function $F(\boldsymbol{q}, \tau)$, we used another inversion method, the *Genetic Inversion via Falsification of Theories* (GIFT) method. This method, developed by E. Vitali, D. E. Galli, and L. Reatto and presented in Ref. [21], was originally used to determine $S(\boldsymbol{q}, \omega)$, starting with QMC calculations of $F(\boldsymbol{q}, \tau)$ of liquid and solid ^{4}He at zero temperature. We have dealt with the inverse problem of solving of the integral equation of the form 2.76 with the kernel for $T = 0$

$$K(\tau, \omega) = \theta(\omega)\, e^{-\tau\omega}, \tag{2.94}$$

where $\theta(\omega)$ is the Heaviside function, namely

$$f(\tau) = \int_0^{+\infty} \mathrm{d}\omega\, e^{-\tau\omega}\, s(\omega). \tag{2.95}$$

In a previous research work, conducted for my master's degree thesis, the GIFT algorithm was extended to tackle the same inverse problem 2.76, but at finite temperature and, thus, accordingly with the kernel

$$K(\tau, \omega) = e^{-\tau\omega}. \tag{2.96}$$

Actually, for reasons that I will explain in Section 2.8, we implemented in the algorithm a different but equivalent expression of the kernel, that is

$$K''(\tau, \omega) = \frac{e^{-\tau\,\omega} + e^{-(\hbar\beta-\tau)\,\omega}}{1 + e^{-\hbar\beta\,\omega}}. \tag{2.97}$$

The inversion problem that we want to face, as explained in Section 2.5, is very ill-posed. We can recall here the approach, well illustrated by Tarantola [66], based on Karl Popper's concept of falsification of theories, according to which observations can be used only to *falsify* a theory. Therefore, given a space of all possible spectral function models $\mathcal{S}$, we can use the QMC data (the observations) to carry out a *falsification test* to exclude all spectral functions $s(\omega)$ that fail to agree with the observations $(\mathcal{F})$.

In addition to the a priori knowledge regarding $s(\omega)$, that we would have to enter through the parameterization of the space $\mathcal{S}$, all the information that can be obtained on the spectral function $s(\omega)$ resides in the QMC data of the correlation function, accompanied by the related uncertainties estimated during the QMC calculations. To fully exploit the information available in the data, we can use these uncertainties to generate new collections of data $\mathcal{F}^*$, that are compatible with the original data $\mathcal{F}$, and use also them to carry out the falsification test. We thus have the result of considerably reducing potential non-physical effects due to statistical fluctuations.

Once the "falsification" test is carried out on all the models, we will obtain a "population" of spectral functions that have "survived" and passed the test. It will thus be necessary to adopt a strategy to capture the common characteristics of all the spectral functions.

2.7.2 Space of Spectral Functions

The *space of the models* $\mathcal{S}$, in this implementation, contains a wide class of functions linear combination of Dirac distributions. This type of function simplifies the calculation of integrals in the numerical computing and, if the discretization of the domain is sufficiently accurate, represents a good approximation of the spectral function.

Typically, the spectral function $s(\omega)$ is real and non-negative, and the zero moment sum rule holds:

$$c_0 = \int_{-\infty}^{+\infty} \mathrm{d}\omega\, s(\omega). \tag{2.98}$$

With this requirements, the models are of the form

$$\bar{s}(\omega) = \sum_{j=1}^{N_\omega} \frac{s_j}{\mathcal{M}} \delta\big(\omega - \omega_j\big), \quad \sum_{j=1}^{N_\omega} s_j = \mathcal{M}, \tag{2.99}$$

where $\bar{s}(\omega)$ is normalized at 1, and thus differs from the physical spectral function $s(\omega)$ by a multiplicative factor c_0. $\bar{s}(\omega)$ is a sum of Dirac δ, each centered in $\omega_j = \big(j - \frac{1}{2}\big)\Delta\omega$, $j = 1, 2, \dots, N_\omega$—the intermediate points of little frequency intervals—and having *spectral weight* $\frac{s_j}{\mathcal{M}}$. N_ω is the number of subdivisions of the frequency domain on which $\bar{s}(\omega)$ is defined. The values of $\bar{s}$ are discretized and $\big\{s_j\big\}_j$ are non-negative integer numbers, i.e.

$$s_j \in \mathbb{N} \cup \{0\}, \quad j = 1, 2, \dots, N_\omega. \tag{2.100}$$

$\big\{s_j\big\}_j$ are also called the number of *quanta* of spectral weight and $\mathcal{M}$ is the total number of quanta of the spectral function model $\bar{s}(\omega)$.

2.7.3 Fitness Function/Falsification Test

As mentioned above, in the GIFT method we try to exploit the greatest amount of information contained in the QMC data, $\mathcal{F} = \{f_1, f_2, \dots, f_{N_\tau}\}$ with the relevant uncertainties $\big\{\sigma_{f_1}, \sigma_{f_2}, \dots, \sigma_{f_{N_\tau}}\big\}$ and the moments $C = \{\dots, c_{-1}, c_0, c_1, \dots\}$. Any equivalent collection of data $\mathcal{F}^*$, such that $\big|f_j - f_j^*\big|$ is of the same oder of magnitude as σ_j, could be the result of another simulation. So, the falsification test requires not only compatibility with $\mathcal{F}$, but also with a large number of equivalent $\mathcal{F}^*$. The equivalent sets of data are generated through the sampling of Gaussian distributions, centered on the original observations with variances equal to the statistical uncertainties. $\mathcal{F}^*$ is then given by

$$\mathcal{F}^* = \big\{f_1 + \varepsilon_1^*, f_2 + \varepsilon_2^*, \dots, f_{N_\tau} + \varepsilon_{N_\tau}^*\big\} = \big\{f_1^*, f_2^*, \dots, f_{N_\tau}^*\big\}, \tag{2.101}$$

where ε_j^* $(j = 1, \dots, N_\tau)$ are the random numbers sampled from a Gaussian distribution with average 0 and variance equal to $\sigma_{f_j}^2$.

To conduct the falsification test we need a measure of the compatibility between the elements of $\mathcal{S}$ and a set of equivalent data $\mathcal{F}^*$. Compatibility implies small deviations from the data, and thus a measurement can be given by

$$\chi^2_{\mathcal{F}^*}(\bar{s}) = \frac{1}{N_\tau} \sum_{j=1}^{N_\tau} \left[f_j^* - \int_{-\infty}^{+\infty} \mathrm{d}\omega\, K\big(\tau_j, \omega\big)\, c_0^*\, \bar{s}(\omega) \right]^2, \tag{2.102}$$

where K is a suitable kernel valued in $\tau_j = (j-1)\,\delta\tau, j = 1, \dots, N_\tau$, ($\delta\tau$ is the time step) and c_0^* is the zero moment, generated by the original one c_0 by sampling a Gaussian, in the same way as the values $\mathcal{F}^*$ are generated from the original data $\mathcal{F}$. The factor c_0^* is present in the expression to bring back the normalization of the model $\bar{s}(\omega)$ to that of the spectral function $s(\omega)$.

The GIFT inversion method, in order to effectively explore the space of the models $\mathcal{S}$ uses a *genetic algorithm* (GA). In fact, this type of algorithm produces a *non local* stochastic dynamic, through an *evolutionary* process, imitating the biological evolution that is observed in the natural world.

Genetic algorithms are techniques used for optimization problems. Given an initial *population* of models, called *individuals*, this is let to *evolve*, by means of operations on the individuals, towards a population consisting of individuals that better satisfy the conditions of optimization set in the algorithm.

Here we will use the word *fitness* to indicate a measure of how much a spectral function agrees with the data. The fitness of a particular $\bar{s}$ should be based on the observed data, i.e. on $\mathcal{D} = \{\mathcal{F}, \mathcal{C}\}$, but, as stated above, every collection of data $\mathcal{D}^*$ compatible with the original $\mathcal{D}$ provides an equivalent contribution to fitness. The *fitness function* is given by

$$\phi_{\mathcal{D}^*}(\bar{s}) = -\chi^2_{\mathcal{F}^*}(\bar{s}) - \gamma_n \chi^2_{\mathcal{C}^*}(\bar{s}), \tag{2.103}$$

$$\chi^2_{\mathcal{C}^*}(\bar{s}) = \sum_n \left[c_n^* - \int_{-\infty}^{+\infty} \mathrm{d}\omega\, \omega^n\, c_0^*\, \bar{s}(\omega) \right]^2 . \tag{2.104}$$

In Eq. 2.103 the free parameters $\gamma_n > 0$ are regulated such that the contribution to the fitness $\phi_{\mathcal{D}^*}$ coming from $\mathcal{F}^*$ $\left(-\chi^2_{\mathcal{F}^*}\right)$ and the one coming from $\mathcal{C}^*$ $\left(-\chi^2_{\mathcal{C}^*}\right)$ are of the same order of magnitude. In this way, we do not give more weight to a particular observation than all the others. The minus sign, placed at the two contributions to the fitness, is due to the choice to define the fitness function as increasing with the increase of the agreement with the data. A higher fitness, i.e. less negative, means greater agreement. In the case that a spectral function moment c_n is known exactly, no error is added, thus c_n^* is set to c_n, i.e. $c_n^* \equiv c_n$. The fitness $\phi_{\mathcal{D}^*}$ is used to rank the models in increasing order.

In the genetic algorithm of the GIFT method we start with a *population* of models $\bar{s}(\omega)$ built randomly. Every $\bar{s}(\omega)$ is represented by an ordered set of N_ω integers s_j of Eq. 2.100. The evolutionary process of the genetic algorithm is constituted by a sequence of generations, in which the population of models is substituted by a new population generated by the previous one. In each generation, the individuals of the population are ordered by an increasing order of fitness. Then some operations are carried out on the individuals: *selection*, *crossover* and *mutation*. These operations have the aim of modifying the individuals to make them evolve towards higher fitness, and therefore towards solutions more compatible with the data.

The *selection* is an operation that consists of choosing the individuals with large fitness from an ascending list of individuals. The k-th individual is extracted according to the formula

$$k = \lfloor N_{\bar{s}} r^{1/3} \rfloor + 1, \tag{2.105}$$

where r is a uniform random number $r \in [0, 1)$, $\lfloor x \rfloor$ is the floor function, and $N_{\bar{s}}$ is the number of individuals of the population at the current generation. The nonlinear dependency ensures that the models with greater fitness are preferentially chosen. The *selection* choose two individuals, the *mother* and the *father*. The *crossover* acts on them. This operation consists of the exchange of one part of the spectral weight quanta, out of the total of $\mathcal{M}$ quanta, generating two *children*. A random integer number p is generated between 0 and $\mathcal{M}$ and p spectral weight quanta are exchanged, selected randomly between the father and the mother. Each exchanged quantum remains in the original frequency small interval, ensuring that the most important characteristics of the parents are preserved in the children. At this point, the *mutations*, operations that shift part of the spectral weight between two small intervals, act on the children, with a given probability.

At each generation these operations are repeated on couples of individuals $N_{\bar{s}}/2$ times, thus substituting the previous generation with a new one, with the exception of the individual with the greatest fitness, that is cloned. This last operation is called *elitism*.

In addition, at each generation the number of individuals that compose the population can be reduced by a certain factor, for example by 5%, up to a minimum number, after which the size of the population remains constant until the last generation. The discarded individuals are those with the lowest fitness. In this way we can start from a large variety of individuals, without wasting computational time for spectral functions that have already failed the falsification test.

An intrinsic GIFT strategy protects against too much agreement with the data (*overfitting*), that would produce non-physical effects in the spectral function: given a $\mathcal{F}^*$, the reconstructed model $\bar{s}(\omega)$ contains some spurious information due to statistical noise, but this information is attenuated or eliminated by averaging the models reconstructed by each $\mathcal{F}^*$. Furthermore, again in order to protect from overfitting, the number of generations is selected such that $\chi^2_{\mathcal{F}^*}(\bar{s})$ at the last generation is of the magnitude of the value $\delta = \frac{1}{N_\tau} \sum_{j=1}^{N_\tau} \sigma^2_{f_j}$, i.e. the average of the variances $\left\{\sigma^2_{f_j}\right\}_{j=1}^{N_\tau}$.

2.7.4 Final Features of Spectral Function

At the end of the evolutionary process, for each set of equivalent data $\mathcal{F}^*$ a certain number of models $\bar{s}(\omega)$ remain; among these, the one with the highest fitness is selected. This is the final model reconstructed through the genetic algorithm for each $\mathcal{F}^*$, that we call $\bar{s}^{(k)}(\omega)$, where k indicates the k-th reconstruction. Each one of the models cannot represent the solution to the inverse problem, as they are determined from a particular set of QMC data affected by statistical error. Each model $\bar{s}^{(k)}(\omega)$ will contain some non-physical information due to uncertainty, that is probably different in every model, since it comes from data that is different, although equivalent. But all these models will also have some common characteristics containing physical information. Therefore, by performing an averaging operation on all of the reconstructed models, we are able capture and emphasize these common characteristics. And the non-physical information due to statistical fluctuations is attenuated or eliminated. Then we find a spectral function $s_{GIFT}(\omega)$—the result of this averaging process on all of the N_r reconstructions—which carries the physical information that the algorithm succeeded in capturing

$$s_{GIFT}(\omega) = \frac{1}{N_r} \sum_{k=1}^{N_r} c_0^{(k)} \bar{s}^{(k)}(\omega), \tag{2.106}$$

where $c_0^{(k)}$ is the c_0^* of the k-th reconstruction.

2.8 Kernel for finite temperature

Originally, the GIFT code was written to deal with the inverse problem that consisted of extracting information on the dynamic structure factor $S(\boldsymbol{q}, \omega)$ for a zero temperature quantum system, from QMC data, relating to the imaginary-time intermediate scattering function $F(\boldsymbol{q}, \tau)$. Subsequently, for the my master's degree thesis the code was extended in order to be able to deal with the analogous inverse problem for finite temperature.

A generic imaginary-time correlation function $f(\tau)$ (Eq. 2.67 on page 35) for finite temperature is given by (a part from constant factors that can be incorporated in $s(\omega)$)

$$f(\tau) = \int_{-\infty}^{+\infty} \mathrm{d}\omega \, e^{-\tau\,\omega} s(\omega). \tag{2.107}$$

Exploiting a symmetry property of $s(\omega)$, the *detailed balance principle* (Eq. 2.38 on page 31)

$$s(\omega) = e^{\hbar\beta\omega} s(-\omega), \tag{2.108}$$

$f(\tau)$ can be rewritten as

$$f(\tau) = \int_{0}^{+\infty} \mathrm{d}\omega \left(e^{-\tau\omega} + e^{-(\hbar\beta-\tau)\,\omega} \right) s'(\omega). \tag{2.109}$$

In this way, we can invert the integral equation using only the positive semi-axis of ω. The inverted spectral function $s'(\omega)$ will thus be defined only on $[0, \infty)$. We then derive the $s(\omega)$ for the negative values of ω by simply reusing the formula 2.108, i.e. $s(\omega) = e^{\hbar\beta\omega} s'(-\omega)$ for $\omega < 0$.

The expression for $f(\tau)$ 2.109 is more convenient, since the information present in $s(\omega)$ for $\omega < 0$, just for the property 2.108, is equivalent to that present in $\omega > 0$. Furthermore, from the computational standpoint, the calculation is lightened, since the domain in which to search for the structures of $s(\omega)$ is halved.

In the GIFT it is essential to obtain the zero moment c_0 of the spectral function from the QMC data, since it gives the correct normalization of $s(\omega)$. Recall that in the GIFT method the models $\bar{s}(\omega)$ are normalized equal to 1. For the case $T = 0$ we have

$$f(0) = \int_0^{+\infty} \mathrm{d}\omega \; s(\omega) = c_0, \tag{2.110}$$

that is

$$c_0 = f_1. \tag{2.111}$$

The zero moment coincides with the value of the correlation function calculated in $\tau = 0$ with QMC computations. In fact, the zero moment of the dynamic structure factor $S(\boldsymbol{q}, \omega)$ is the static structure factor $S(\boldsymbol{q})$ that is customarily determined in QMC simulations.

For $T > 0$, with respect to the case with $T = 0$, there is an inconvenience, since using Eq. 2.109 we have

$$f(0) = \int_0^{+\infty} \mathrm{d}\omega \left(1 + e^{-\hbar\beta\,\omega}\right) s'(\omega) \quad \text{and} \tag{2.112}$$

$$c_0 = \int_0^{+\infty} \mathrm{d}\omega \, s'(\omega), \tag{2.113}$$

therefore $f_1 \neq c_0$. It is thus necessary to again modify the kernel such that $f_1 = c_0$. We multiply and divide the integrand of 2.112 by $\left(1 + e^{-\hbar\beta\,\omega}\right)$ and a new spectral function is defined,

$$s''(\omega) \equiv \left(1 + e^{-\hbar\beta\,\omega}\right) s'(\omega). \tag{2.114}$$

The 2.107 thus becomes

$$f(\tau) = \int_0^{+\infty} \mathrm{d}\omega \, \frac{e^{-\tau\,\omega} + e^{-(\hbar\beta-\tau)\,\omega}}{1 + e^{-\hbar\beta\,\omega}} \, s''(\omega). \tag{2.115}$$

We thus have

$$f(0) = \int_0^{+\infty} \mathrm{d}\omega \, s''(\omega), \tag{2.116}$$

i.e. $f_1 = c_0$, with $c_0 \equiv \int_0^{+\infty} \mathrm{d}\omega \, s''(\omega)$.

At this point it could be objected that the new kernel is "worse" than the original one, making the problem even more ill-posed. Let us analyze the new kernel, that we call $K''(\tau, \omega)$. K'' differs from the previous kernel K' 2.109, by the multiplicative factor $1/\left(1 + e^{-\hbar\beta\,\omega}\right)$, which in $\omega = 0$ has the value $\frac{1}{2}$ and then grows monotonically until 1 for $\omega \to \infty$. Therefore, for small values of ω, with $\tau > 0$, $K'(\tau, \omega)$ is reduced by a factor between $\frac{1}{2}$ and 1, and then it converges for large ω to $K''(\tau, \omega)$. Thus, K' is only slightly modified.

As we can see in Fig. 2.1 on the following page, we also observe that, comparing $K''(\tau, \omega)$ with $K(\tau, \omega)$ (the kernel in Eq. 2.107) for $\omega > 0$, for small τ ($\tau \to 0$) the two kernels have a very similar course in function of ω. While for large τ, i.e. $\tau \to \hbar\beta/2$, (not

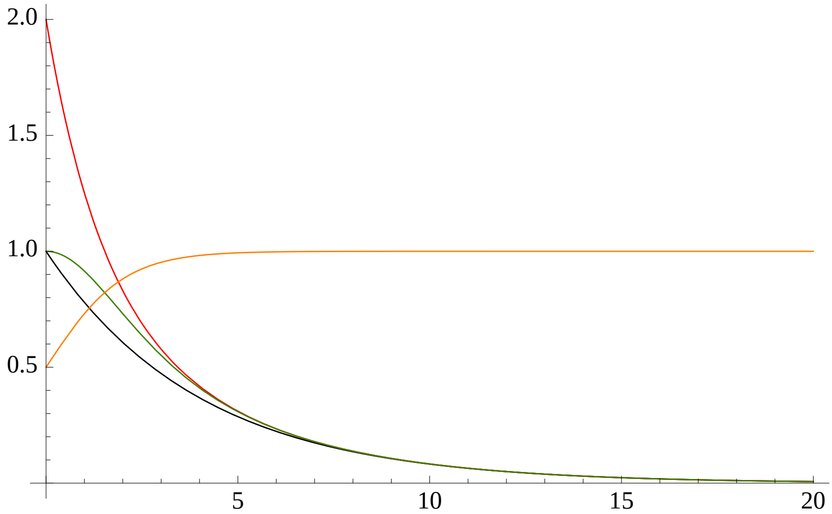

Figure 2.1 Graphics in function of ω of the kernels $K(\tau,\omega)$ (black line), $K'(\tau,\omega)$ (red line), and $K''(\tau,\omega)$ (green line) in $\tau = 0.25$ with $\hbar\beta = 1$; and the orange line is the factor $1/\left(1+e^{-\hbar\beta\,\omega}\right)$.

shown in figure) $K(\tau,\omega)$ decreases much more rapidly than $K''(\tau,\omega)$. Thus, in conclusion, the problem of inversion with the new kernel is equally ill-posed if not even less ill-posed.

Thus for the case $T > 0$ the kernel is given by

$$K''(\tau,\omega) = \frac{e^{-\tau\,\omega} + e^{-(\hbar\beta-\tau)\,\omega}}{1+e^{-\hbar\beta\,\omega}}. \tag{2.117}$$

The spectral function resulting from the inversion is given by Eq. 2.114, therefore, once $s''(\omega)$ is determined, the "true" $s(\omega)$ is obtained as

$$s(\omega) = \begin{cases} \dfrac{1}{1+e^{-\hbar\beta\,\omega}}\,s''(\omega) & \text{for} \quad \omega > 0 \\ \dfrac{e^{\hbar\beta\omega}}{1+e^{-\hbar\beta\,\omega}}\,s''(-\omega) & \text{for} \quad \omega < 0 \end{cases}. \tag{2.118}$$

CHAPTER 3

Quantum Dynamics of Hard Sphere Bosons

3.1 Introduction

The study of collective modes and dynamic properties of quantum liquids and gases has always represented a very important issue in quantum many-body theories. In particular, in the case of Bose systems, this study is fundamental in understanding the phenomenon of superfluidity and, starting from the pioneering studies of Landau and Bogoliubov in the 1940s, it has been the subject of a huge number of investigations, both theoretical and experimental [67]. Two main theoretical paradigms exist for Bose systems: the Bogoliubov's theory, that is a mean-field theory suitable for the weakly-interacting boson systems, like dilute ultracold gases, and the theory of Feynman, able to predict a qualitative energy–momentum dispersion curve proper of strongly interacting boson systems, like superfluid ^{4}He. This dispersion relation with its characteristic shape—phonon-maxon-roton—presents a minimum at finite momentum, a fundamental requirement to have superfluidity. Feynman's paradigm has been pushed until to describe with high accuracy the excitation spectrum by means of variational Monte Carlo methods.

Some of the questions concerning these approaches were: is it possible to carry the two approaches into a unifying theoretical view, able to describe collective excitations from weakly interacting to strongly interacting boson systems? And does a model system exist which is suitable to describe both interacting regimes?

A physical insight into the dynamic behavior of quantum many-body systems can be given estimating the dynamic structure factor, $S(\boldsymbol{q}, \omega)$. This quantity, indeed, contains a wealth of information about the nature and the energy spectrum of the excitations coupled with density fluctuations.

3.1.1 Bogoliubov spectrum

An important physical quantity for weakly-interacting systems is the s-wave scattering length a, a measure of the amplitude of the interaction in the scattering between two low-energy particles. We can compare $|a|$ with the average inter-particle distance, $d = n^{-1/3}$, where n is the density of the gas, or, equivalently, the so-called *gas parameter* $n|a|^3$ with unity [68].

For dilute gases at very low temperature we can safely assume that the diluteness condition $n|a|^3 \ll 1$ holds and the ground state of the many-body system can be described in terms of a macroscopic wave function [69]. In this regime, mean-field theories are expected to provide an accurate description of the system and the elementary excitations can be expressed in terms of a single quasiparticle. Therefore, the dynamic structure factor is exhausted by a single excitation peak

$$S(\boldsymbol{q},\omega) = S(\boldsymbol{q})\,\delta(\omega - \varepsilon_B(\boldsymbol{q})/\hbar)\ , \tag{3.1}$$

whose dispersion follows the Bogoliubov spectrum

$$\varepsilon_B(\boldsymbol{q}) = \frac{\hbar^2}{2m\xi^2}\sqrt{(q\xi)^4 + 2(q\xi)^2} \tag{3.2}$$

in which $\xi = 1/\sqrt{8\pi n a}$ is the healing length (for a reference on these arguments see, e.g., Ref. [68]). In the contest of the low energy excitations, ξ represents the length scale at which the transition between the phonon and free-particle regime occurs, i.e. when $\hbar q \sim mc$, where c is the velocity of sound. This result, predicted for the first time in 1947, has been confirmed experimentally in 2002 by Steinhauer *et al.*, who have been able to measure the excitation spectrum of a dilute condensate of ^{87}Rb atoms by means of Bragg spectroscopy [70].

As the density of the system increases, the interactions among the particles become more and more important and the picture provided by mean-field theories is no longer valid. Indeed, experimental measurements [71–76] of the dynamic structure factor in liquid ^{4}He, which is a well-known benchmark of a dense Bose fluid, shows a different behavior from the one predicted for dilute systems. First of all, the $S(\boldsymbol{q},\omega)$ in liquid ^{4}He presents, in addition to a sharp *quasiparticle* peak, a broad contribution at higher frequencies, usually called multiphonon branch, that indicates the possibility to induce incoherent excitations in the many-body system. Furthermore, the dispersion of the main peak of $S(\boldsymbol{q},\omega)$ differs from the Bogoliubov spectrum, Eq. 3.2, and presents a phonon-maxon-roton behavior, which is linear at low q and displays a relative minimum for a non-zero wave vector.

3.1.2 Feynman spectrum

A qualitative description of the appearance of the roton minimum in the excitation spectrum with increasing na^3 is given by means of Feynman's spectrum [77]

$$\varepsilon_F(\boldsymbol{q}) = \hbar\,\omega_F(\boldsymbol{q}) = \frac{\hbar^2 q^2}{2m\,S(\boldsymbol{q})}\ , \tag{3.3}$$

in which $S(\boldsymbol{q})$ is the static structure factor. $\varepsilon_F(\boldsymbol{q})$ is accurate for low wave vectors and energies and in general provides a useful upper bound for the energy excitation spectrum, $\varepsilon(\boldsymbol{q}) \leq \varepsilon_F(\boldsymbol{q})$. This relation is easily obtained from the f-sum rule

$$\int_0^\infty \mathrm{d}\omega\, \omega\, S(\boldsymbol{q},\omega) = \frac{\hbar q^2}{2m} \tag{3.4}$$

with the assumption that the dynamic structure factor can be written as a single delta-peak $S(\boldsymbol{q},\omega) = S(\boldsymbol{q})\delta\left(\omega - \omega_F(\boldsymbol{q})\right)$ and indicates that the emergence of a minimum in $\varepsilon(\boldsymbol{q})$ can be associated to the emergence of a maximum in $S(\boldsymbol{q})$ and thus to the formation of the microscopic local structures typical of dense fluids [78].

3.1.3 The model system

In this work, we want to study, by means of QMC methods, the dynamic properties of Bose gases at zero temperature, focusing on the crossover from weak to strong-interaction regime. To model the interactions among the particles, we use the two-body hard-sphere (HS) interaction potential

$$V(r) = \begin{cases} \infty\,, & r \leq a \\ 0\,, & r > a \end{cases}\,, \tag{3.5}$$

where the range of the potential a coincides with the s-wave scattering length. This model has been widely used to study many-body systems with short-range repulsive interactions, not only in the dilute regime, where the details of the interatomic potential are irrelevant, but also in the dense regime [2, 10, 79, 80]. The HS model, indeed, serves as a reference for those systems in which the leading part of the two-body potential is the repulsive hard-core and it has been used to characterize semi-quantitatively the static properties of superfluid ^{4}He [2, 80].

Moreover, the HS model provides one with a well defined system, where quantum correlations can be investigated from the weak to the strong-interaction regime by varying a single parameter, i.e. the reduced density in units of the HS range a.

3.2 Details on the propagator and trial wave function

In this work, we have employed for the short-time many-body propagator the pair-product (PP) propagator built using the PP form of the propagator (see Eq. 1.39 on page 21 in Chapter 1)

$$G^{\mathrm{PP}}(\mathbf{R},\mathbf{R}';\delta\tau) = G^0(\mathbf{R},\mathbf{R}';\delta\tau) \prod_{1\leq i<j\leq N} G^{\mathrm{eff}}_{\mathrm{rel}}\left(\boldsymbol{r}_{ij},\boldsymbol{r}'_{ij};\delta\tau\right) \tag{3.6}$$

using as two-body (effective) interaction propagator $G^{\mathrm{eff}}_{\mathrm{rel}}$ the *exact* two-body interaction propagator. In the case of the HS potential 3.5 a high energy expansion of the two-body

$n\,a^3$	$\delta\tau\ \left[\hbar^2/(2\,m\,a^2)\right]$	M
1×10^{-4}	4.0	1
1×10^{-2}	0.125	10
5×10^{-2}	0.025	15
1×10^{-1}	0.015	20
2.138×10^{-1}	0.01	12
3×10^{-1}	0.005	25

Table 3.1 Value of the parameters $\delta\tau$ and M of the simulations adopted for the different values of the gas paramater.

propagator due to Cao and Berne [81] provides an accurate approximation of $G^{\text{eff}}_{\text{rel}}$ holding at small time steps:

$$G^{\text{eff}}_{\text{rel,Cao}}\left(\boldsymbol{r}_{ij},\boldsymbol{r}'_{ij};\delta\tau\right) = 1 - \frac{a(r+r')-a^2}{r\,r'}\exp\left(-\frac{m}{2\hbar^2\delta\tau}\left[r\,r' + a^2 - a(r+r')\right](1+\cos\theta)\right), \tag{3.7}$$

where θ is the angle between $\boldsymbol{r}$ and $\boldsymbol{r}'$.

For the gas phase we choose the translationally invariant Jastrow function

$$\Psi_J(\mathbf{R}) = \prod_{i<j} f\left(\left|\boldsymbol{r}_i - \boldsymbol{r}_j\right|\right), \quad f(r) = \begin{cases} 0 & \text{for} \quad r \le a \\ \sin\left[k(r-a)\right]/r & \text{for} \quad r > a \end{cases}. \tag{3.8}$$

The function f is the solution of the two-body s-wave scattering problem with a HS potential and the wave vector k is chosen such as the derivative $f'(r)$ vanishes at $r = L/2$, where L is the size of the cubic simulation box, in order to fulfill the periodic boundary conditions [10], in this way the value of k turns out to depend on the size of the box.

To simulate the solid phase we instead use a trial wave function that explicitly breaks translational symmetry, obtained by multiplying the Jastrow wave function 3.8 by a one-body term, due to Nosanow [82], which localizes the particles at the lattice sites of the crystal, i.e. the Nosanow-Jastrow wave function,

$$\Psi_T(\mathbf{R}) = \prod_{i=1}^{N} e^{-(\boldsymbol{r}_i - \boldsymbol{S}_i)^2/\alpha^2} \prod_{i<j} f(|\boldsymbol{r}_i - \boldsymbol{r}_j|), \tag{3.9}$$

Here, the localization term is a Gaussian whose width α is a variational parameter and the lattice sites $\{\boldsymbol{S}_i\}_{i=1}^{N}$ correspond to an fcc crystal. α is obtained minimizing the energy as function of α at $n a^3 = 2.5\times10^{-1}$ with $M = 1$ (M is the number of beads, that will be mentioned shortly after) and the determined value has turned out to be $\alpha = 1/\sqrt{1.5}$. I notice that the above wave function is not symmetric under particle exchange. Still, as explained in Section 1.4 the particle permutations are correctly sampled during the simulation by means of the swap moves in the worm algorithm, generating in a symmetric ground-state wave function $\Psi_0(\mathbf{R})$, obtained projecting it with the PIGS method as described in Chapter 1. I remark that the proper symmetry of $\Psi_0(\mathbf{R})$ is crucial when calculating the one body density matrix (OBDM) $\rho_1(r)$.

3.3 Dynamics from the dilute to the dense regime

The calculation of the dynamic structure factor in a HS Bose system at a given gas parameter na^3 has been carried out by performing PIGS simulations with $N = 400$ particles interacting with the two-body potential given by Eq. 3.5 and confined in a cubic box with periodic boundary conditions. We have chosen the optimal values of the imaginary time step $\delta\tau$ and the number of beads M studying the convergence of the mean energy per particle for small time step $\delta\tau$ and for large evolution time τ. $\delta\tau$ and M depend both on the gas parameter and the values found and used are shown in Table 3.1 on the facing page. I note that for the computation of the imaginary-time correlation function and, thus, the extraction of $S(\boldsymbol{q}, \omega)$, we added 100 beads to the value given in table. These extra beads are necessary to evaluate the correlation function at sufficiently large imaginary times.

3.3.1 Weak-interaction regime

In the regime of weak interactions the mean field theory should provide accurate an description of the dynamics of the gas of hard sphere. So when the gas parameter assumes the very low value of 10^{-4}, the dynamic structure factor should be well approximated by Eq. 3.1, with a delta function peaked at the Bogoliubov spectrum 3.2. Applying the Laplace transform defined in 2.95 to the Bogoliubov $S(\boldsymbol{q}, \omega)$, we obtain that the intermediate scattering function $F(\boldsymbol{q}, \tau)$ is simply given by an exponential function:

$$F(\boldsymbol{q}, \tau) = S(\boldsymbol{q})\, e^{-\tau \varepsilon_{\mathrm{B}}(\boldsymbol{q})/\hbar} \,. \tag{3.10}$$

As it is shown in Fig. 3.1a, for a single wave vector $\boldsymbol{q}$, the scattering function $F(\boldsymbol{q}, \tau)$ obtained from the PIGS simulations at weak interaction regime with gas parameter $na^3 = 10^{-4}$ is very well fitted by a single exponential function. A similar agreement is obtained at all the studied wave vectors $\boldsymbol{q}$.

At the smallest value of the interaction strength, $na^3 = 10^{-4}$ (see Fig. 3.2 on page 55), the dynamic structure factor is exhausted, for all reported values of $\boldsymbol{q}$, by a single narrow peak corresponding to the excitation of a quasiparticle with energy $\hbar\omega(\boldsymbol{q})$. The dispersion of the peak with the wave vector $\boldsymbol{q}$ follows closely the Bogoliubov spectrum $\varepsilon_{\mathrm{B}}(\boldsymbol{q})$ 3.2 (see Fig. 3.2b). Let's notice that the line in the figure is not a fit to positions of the peaks but is the plot of $\omega_{\mathrm{B}}(\boldsymbol{q})$, which in units of $\hbar/\left(2m\xi^2\right)$ for $\omega(\boldsymbol{q})$ and ξ^{-1} for wave vector q, is given by

$$\varepsilon_B(\boldsymbol{q}) = \hbar\omega_{\mathrm{B}}(\boldsymbol{q}) = \sqrt{q^4 + 2q^2} \tag{3.11}$$

which is independent of the gas parameter na^3. A small damping of the quasiparticles,

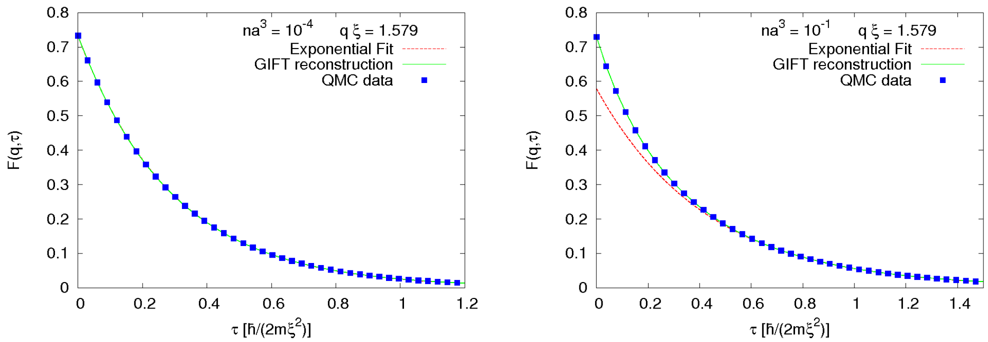

(a) $na^3 = 10^{-4}$ **(b)** $na^3 = 10^{-1}$

Figure 3.1 Scattering function $F(q, \tau)$ for two different values of the interaction strength. The (green) solid line corresponds to the GIFT reconstruction of the $S(\boldsymbol{q}, \omega)$, the (red) dashed line is the exponential fit to the long-time tail. In the left panel the exponential fit coincides with the GIFT reconstruction and is hidden it.

called Beliaev damping, was predicted in Ref. [83], resulting in a broadening of the excitation peak. We attribute the small width of the peaks in Fig. 3.2a to the limited ability of the GIFT method to determine their exact position in the inversion procedure and not to the physical processes involved with Beliaev damping. The method posses a limited resolution power, and thus it may produce broadening also when a delta-like excitation is present.

For larger values of the gas parameter, the long-time tail of $F(\boldsymbol{q}, \tau)$ can still be well fitted by an exponential function corresponding to the lowest excitation peak, (until it is a well defined peak) as one can see in Fig. 3.1b for $na^3 = 10^{-1}$. The short-time decay of the correlation function is instead dominated by higher energy multiphonon excitations, which cannot be described by a simple exponential law. This is clearly shown in Fig. 3.1b where one has to use the function $F(\boldsymbol{q}, \tau)$ reconstructed from $S_{GIFT}(\boldsymbol{q}, \omega)$ using Eq. 2.95 on page 42 to reproduce the QMC data everywhere.

3.3.2 Emergence of multiphonons

The results at $na^3 = 10^{-2}$ are shown in Fig. 3.3 on page 56. While at the smallest wave vector $S(\boldsymbol{q}, \omega)$ is still given by a narrow peak centered at the phonon energy $\hbar\omega(\boldsymbol{q}) = c\hbar q$ where c is the speed of sound (see Fig. 3.6 on page 59 These features are more evident at $na^3 = 5 \times 10^{-2}$ (see Fig. 3.4 on page 57) where, in addition, a secondary broad multiphonon peak starts to appear at large wave vectors. We notice, from Figs. 3.3b and 3.4b, that the curvature of the spectrum, for $\boldsymbol{q}$ in the range $0.8 \lesssim q \lesssim 1.2$, changes from positive

(a) $S(\boldsymbol{q}, \omega)$ at three fixed $\boldsymbol{q}$

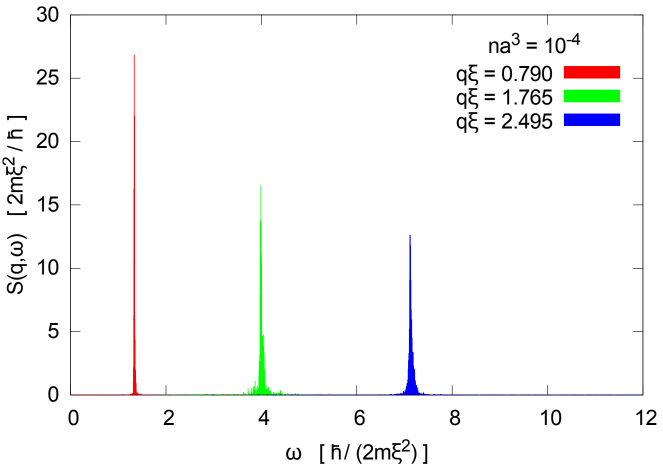

(b) Color map of $S(\boldsymbol{q}, \omega)$

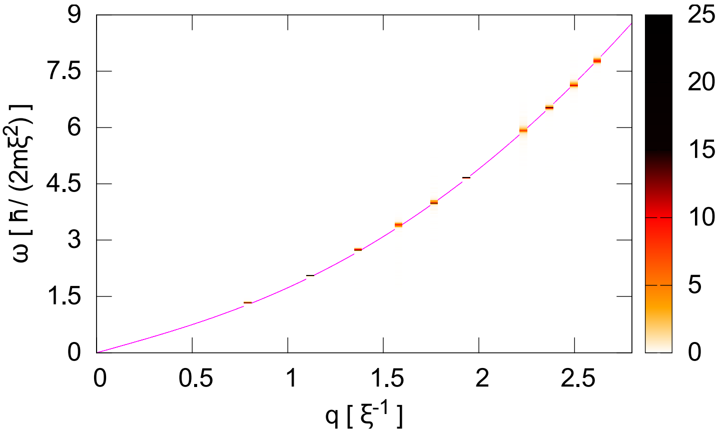

Figure 3.2 Dynamic structure factor $S(\boldsymbol{q}, \omega)$ at $na^3 = 10^{-4}$: **(a)** for three values of the wave vector q; **(b)** color map of $S(\boldsymbol{q}, \omega)$ as a function of q and the red line is the Bogoliubov dispersion 3.2 for comparison.

to negative in this interval of values of the gas parameter. A positive curvature, similar to the Bogoliubov spectrum 3.2, implies that long-wavelength phonons can decay into pairs of phonons by means of Beliaev processes. These decaying mechanisms are instead forbidden if the curvature of the spectrum is negative.

(a) $S(\boldsymbol{q},\omega)$ at three fixed $\boldsymbol{q}$

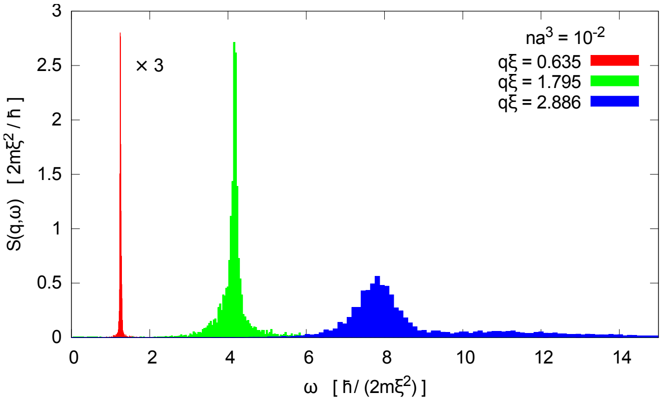

(b) Color map of $S(\boldsymbol{q},\omega)$

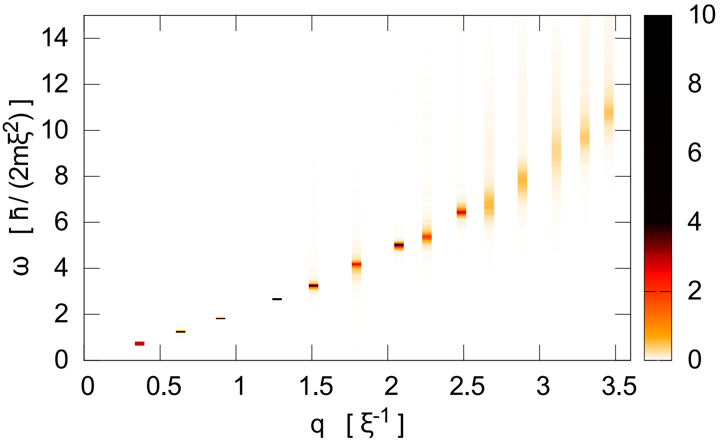

Figure 3.3 $S(q,\omega)$ at $na^3 = 10^{-2}$. **(a)** $S(\boldsymbol{q},\omega)$ for three values of the wave vector q; the plot corresponding to $q = 0.635\,\xi^{-1}$ is reduced by a factor 3 to make it visible on the scale of the other two. **(b)** Color map of $S(\boldsymbol{q},\omega)$ at different wave vectors q; the vertical bars are the representations of $S(\boldsymbol{q},\omega)$ at fixed $\boldsymbol{q}$ as function of ω.

3.3.3 Appearence of roton excitations

We also notice that, at the gas parameter $na^3 = 5 \times 10^{-2}$, the dispersion of the central position of the highest peak exhibits a shoulder in the region $1.5 \lesssim q\xi \lesssim 2$. This shoulder develops into a visible minimum at the largest interaction strength $na^3 = 10^{-1}$ (see Fig. 3.5b on page 58). Observing the Fig. 3.5b on page 58, in the region around the minimum $q\xi = 1.901$, one can clearly distinguish one relatively narrow peak at small frequency,

(a) $S(\boldsymbol{q}, \omega)$ at three fixed $\boldsymbol{q}$

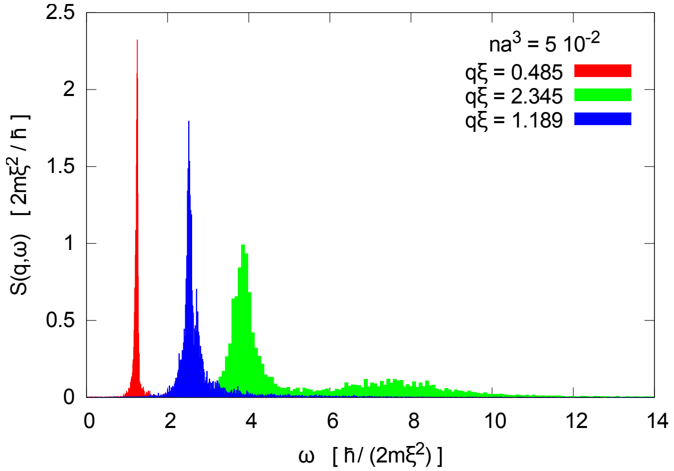

(b) Color map of $S(\boldsymbol{q}, \omega)$

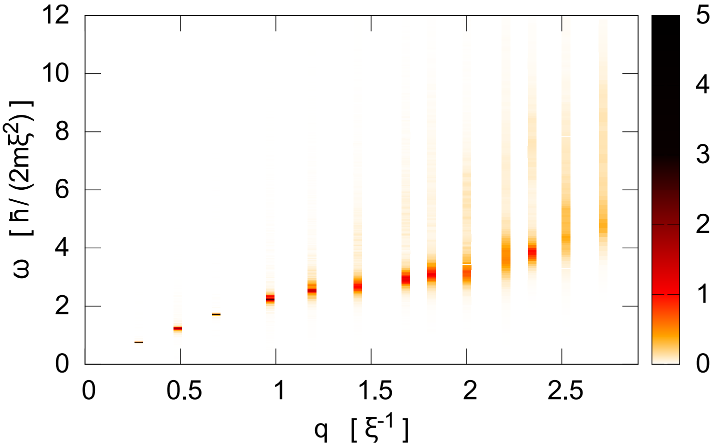

Figure 3.4 Dynamic structure factor at $na^3 = 5 \times 10^{-2}$. **(a)** $S(\boldsymbol{q}, \omega)$ for three values of the wave vector q. **(b)** Color map of $S(\boldsymbol{q}, \omega)$ at different wave vectors q; the vertical bars are the representations of $S(\boldsymbol{q}, \omega)$ at fixed $\boldsymbol{q}$ as function of ω.

corresponding to the excitation of a single quasiparticle, from a broad multiphonon peak at higher frequency. We note also that a strong damping is present at excitation energies greater than the double of the energy of rotons, occurring, in this case, at high wave vectors ($q\xi \gtrsim 2.3$), suggesting a mechanism of decaying of high-energy quasi-particle excitations into two, or more, roton quasi-particle excitations.

(a) $S(\boldsymbol{q},\omega)$ at three fixed $\boldsymbol{q}$

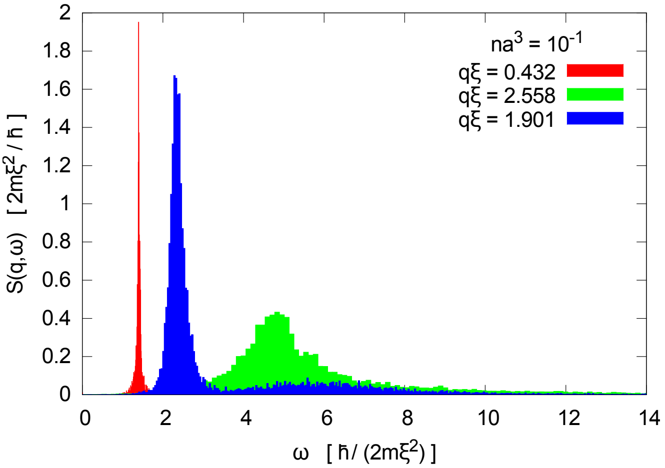

(b) Color map of $S(\boldsymbol{q},\omega)$

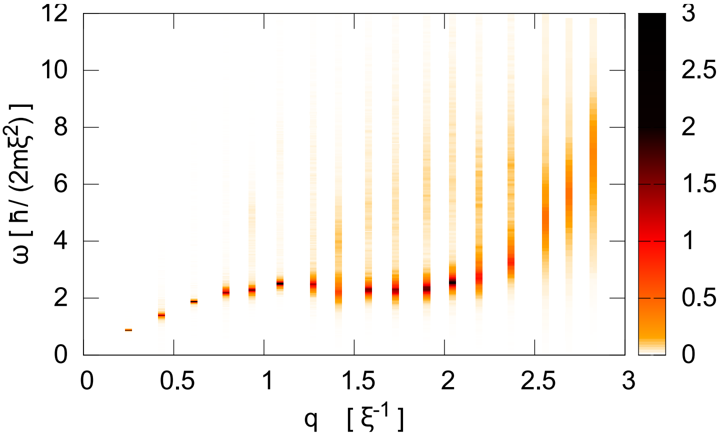

Figure 3.5 Dynamic structure factor at $na^3 = 10^{-1}$. **(a)**$S(\boldsymbol{q},\omega)$ for different values of the wave vector q. **(b)** Color map of $S(\boldsymbol{q},\omega)$ at different wave vectors q; the vertical bars are the representations of $S(\boldsymbol{q},\omega)$ at fixed $\boldsymbol{q}$ as function of ω.

3.3.4 All regimes

To summing up the results shown until here, the dispersion of the central position of the highest peak in $S(\boldsymbol{q},\omega)$ is reported in Fig. 3.6 on the next page as a function of the wave vector $\boldsymbol{q}$ for different values of the gas parameter. As we already pointed out, at $na^3 = 10^{-4}$ the dispersion curve is in good agreement with the prediction of Bogoliubov theory 3.2 holding for dilute systems. For larger values of na^3 deviations start to appear

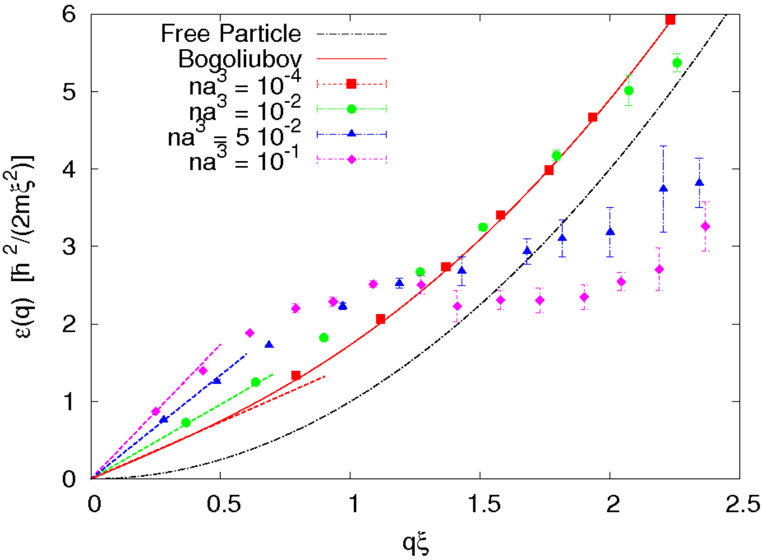

Figure 3.6 Dispersion of the central position of the highest peak in $S(\boldsymbol{q},\omega)$ for different values of the gas parameter. The error–bars represent the 1/2–height widths of the peaks. The solid line is the Bogoliubov prediction and the dot–dashed line corresponds to the free-particle dispersion $(q\xi)^2$. The dashed lines show the phonon dispersion $c\hbar q$, where the speed of sound c is calculated from the equation of state [84].

both in the phonon region ($q\xi < 1$), where the excitation energy is higher than $\varepsilon_B(\boldsymbol{q})$, and in the single-particle region ($q\xi > 1$), where $\hbar\omega(\boldsymbol{q}) < \varepsilon(\boldsymbol{q})_B$. The roton minimum becomes clearly visible for the largest value of the interaction strength. Our results show that no long–range attractive tail in the interaction potential is needed to observe a roton minimum in the density fluctuation spectrum.

We also point out that, for all values of the gas parameter, the dispersion of the main peak in $S(\boldsymbol{q},\omega)$ at the smallest wave vectors is in good agreement with the phonon dispersion $\hbar\omega(\boldsymbol{q}) = c\hbar q$, where c is the speed of sound which we determine from the compressibility relation $mc^2 = n\frac{\mathrm{d}\mu}{\mathrm{d}n}$, involving the chemical potential $\mu = \frac{\mathrm{d}E}{\mathrm{d}N}$. In practice, we calculate the value of c as a function of the gas parameter by using the fit to the equation of state $E(n)$ of the HS gas found in ref. [84].

3.3.5 Comparison with superfluid ^{4}He

Particular interest has to be devoted to the study of the HS system at the gas parameter $na^3 = 2.138 \times 10^{-1}$. The HS gas at this density has been used as a reference system for the simulation of superfluid ^{4}He at equilibrium in a previous work which considers the hard-wall potential as the leading part of the He-He interaction and the attractive tail as

(a) $S(\boldsymbol{q},\omega)$ at three fixed $\boldsymbol{q}$

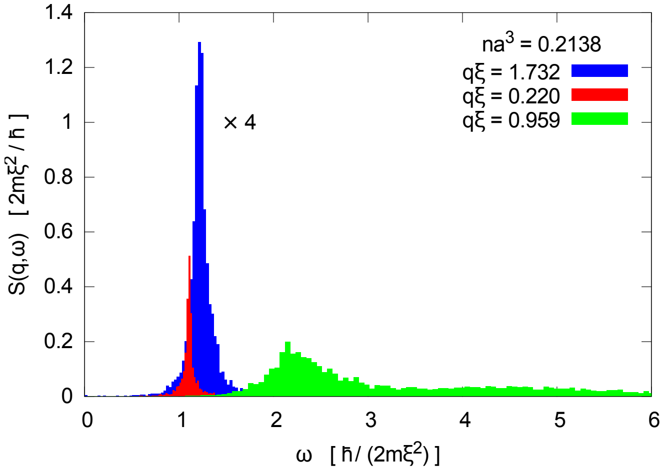

(b) Color map of $S(\boldsymbol{q},\omega)$

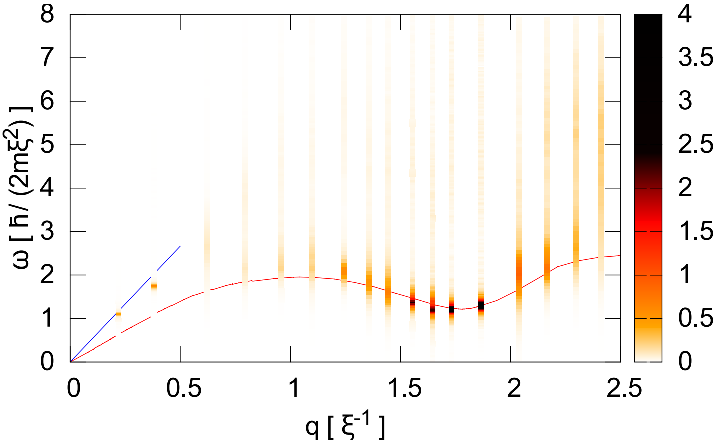

Figure 3.7 Dynamic structure factor at $na^3 = 2.138 \times 10^{-1}$. **(a)** $S(\boldsymbol{q},\omega)$ of HS for three values of the wave vector q. **(b)** Color map of $S(\boldsymbol{q},\omega)$ at different wave vectors q; the vertical bars are the representations of $S(\boldsymbol{q},\omega)$ at fixed $\boldsymbol{q}$ as function of ω. The red line represents the experimental dispersion of the elementary excitations in liquid ^{4}He at saturated vapor pressure [85] and the blue line represent the phonon dispersion $\omega(\boldsymbol{q}) = cq$, with c obtained from the equation of state of a HS gas [84]

.

a weak perturbation [2]. The value $na^3 = 2.138 \times 10^{-1}$ is obtained from the experimental density of liquid ^{4}He at saturated vapour pressure and from the s-wave scattering length

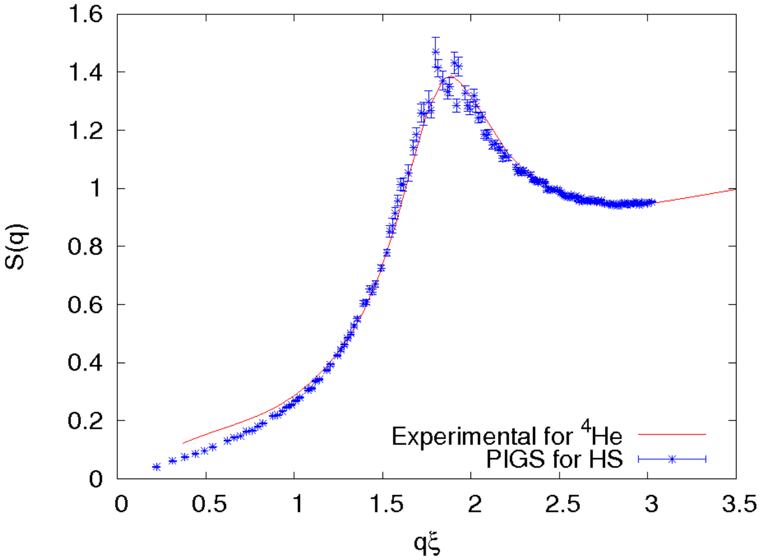

Figure 3.8 Static structure factor $S(\boldsymbol{q})$ for the HS gas at $na^3 = 2.138 \times 10^{-1}$ (blue symbols). The red solid line represents the static structure factor measured in liquid ^{4}He at $T = 1$ K by neutron scattering experiments [86].

of the repulsive part of the Lennard-Jones potential which models the He-He interaction.

Results for $S(\boldsymbol{q}, \omega)$ in the HS gas at $na^3 = 2.138 \times 10^{-1}$ are showed in Fig. 3.7 on the facing page: we see that the spectral function presents a sharp quasiparticle peak for small values of $\boldsymbol{q}$ and in the region where the excitation spectrum displays the minimum, $1.5 \lesssim q\xi \lesssim 2$, while it is broader for wave vectors between these two regimes, $0.5 \lesssim q\xi \lesssim 1.5$, the region of the quasi-particle excitations called maxons. As one can see in Fig. 3.7a, looking at the green plot of $S(\boldsymbol{q}, \omega)$ with wave vector in the maxon region, the broadening is very wide indicating a strong damping of the collective modes, unlike what occurs at equilibrium in the superfluid ^{4}He. As observed above about the spectrum at $na^3 = 10^{-1}$, I notice that this damping occurs for excitations with energy greater than two times the roton energy, signaling a decaying of excitations into two or more rotons with wave vectors which (vectorial) sum equals to the wave vector of the high-energy excitation.

In Fig. 3.7b, we also compare the spectra obtained in our work with the dispersion curve for elementary excitations in superfluid ^{4}He at low temperature, obtained from inelastic neutron scattering experiments [85], conveniently rescaled in the units of ξ^{-1} for the wave vector and of $\hbar/(2m\xi^2)$ for the frequency. At small $\boldsymbol{q}$, we see that the dispersion of the main peak of $S(\boldsymbol{q}, \omega)$ is linear, as we expect from the phonon dispersion law $\hbar\,\omega(\boldsymbol{q}) = c\hbar q$; the value for the speed of sound c obtained from our result is in agreement with the one calculated from the equation of state for a HS gas [84], but it is larger than the value obtained from the experimental measurements on superfluid ^{4}He, indicating, as one should expect, that the attractive part of the He–He potential plays a relevant role in determining the velocity of sound in the system. On the contrary, the dispersion of the main peak of $S(\boldsymbol{q},\omega)$ is in good agreement with the experimental excitation spectrum in the roton region and for higher momenta. This result evidences that the energy–momentum dispersion in roton region is largely dominated by the repulsive part of the interaction potential; in fact the behavior of the system in the roton wave-vector region is characterized by correlations on the scale of the interparticle distance $n^{-1/3}$. I would like to note that also at large wave vectors, in the post-roton region, $S(\boldsymbol{q},\omega)$ broadens due to the damping occurring for the same reason described above.

In Fig. 3.8 on the previous page, we show the PIGS results for the static structure factor $S(\boldsymbol{q})$ of the HS gas at $na^3 = 2.138 \times 10^{-1}$ and we compare these with experimental measurements in liquid ^{4}He at $T = 1\,\mathrm{K}$ and saturated vapor pressure [86]. We can see that the agreement is excellent for $q\xi \gtrsim 1$, indicating that the HS model is able to reproduce the microscopic structure of the ^{4}He system at distances comparable and smaller than the mean interparticle separation. Deviations between the PIGS results and the experimental curve are instead visible in the range $q\xi \lesssim 1$, which arise from the inability of the HS model to describe the long-range correlations among the ^{4}He atoms. Thermal effects are not expected to affect the comparison since, at such low temperature, they are negligible for $q \gtrsim 0.3\,\text{Å}^{-1} = 0.277\,\xi^{-1}$ (see ref. [87]).

In conclusion, these remarkable results indicate clearly that the structure and the density fluctuation spectrum of superfluid ^{4}He, for wave vectors larger and on the order of the inverse mean interparticle distance, can be well described in terms of the hard-core repulsive potential alone.

3.3.6 Static structure factors and Feynman spectrum

We also report in Fig. 3.9 on the facing page the results on the static structure factor $S(\boldsymbol{q})$, for the values of the gas parameter considered in this project. At densities larger than $na^3 \gtrsim 0.1$, a peak starts to develop for wave vectors on the order of $2\pi n^{1/3}$, signaling the appearance of local shell structures typical of a dense gas. A similar feature in $S(\boldsymbol{q})$ is exhibited by superfluid ^{4}He, where the well-known roton minimum in the spectrum of excitations is occurring. The speed of sound c enters also in the linear slope $S(\boldsymbol{q}) \simeq \frac{q}{2mc}$, characterizing the static structure factor at small momenta and arising from phonon excitations. Fig. 3.9 on the next page shows that our QMC results for $S(\boldsymbol{q})$ well reproduce this asymptotic law. Only at the lowest density, $na^3 = 10^{-4}$, the smallest values of $\boldsymbol{q}$ set by the size of the simulation box appear to be already slightly outside the phonon regime.

We can use the data on $S(\boldsymbol{q})$ to test the Feynman approximation 3.3, explained above, from a quantitative point of view. We compare in Fig. 3.10 on page 64 the accurate result

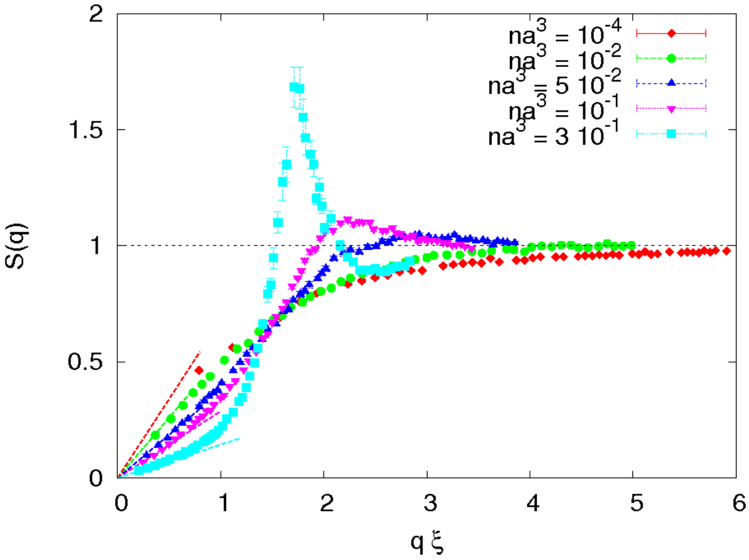

Figure 3.9 Static structure factor $S(\boldsymbol{q})$ for HS system at various densities in the gas phase. The dashed lines at small momenta correspond to the linear slope $S(\boldsymbol{q}) = q/(2mc)$, where c is the speed of sound calculated from the equation of state [84] at the corresponding densities indicated in legend.

for $\varepsilon(\boldsymbol{q})$, obtained from the GIFT estimation of the dynamic structure factor, with the approximated result $\varepsilon_F(\boldsymbol{q})$ obtained from the PIGS results for $S(\boldsymbol{q})$, according to Eq. 3.3. We can see that the Feynman's approach is able to describe accurately the dynamics of the HS gas only for small values of the wave vector q. At large q, instead, we notice a discrepancy between the Feynman's prediction $\varepsilon_F(\boldsymbol{q})$ and the GIFT results, which becomes larger as the gas parameter increases. From this comparison, we can conclude that the assumption of describing the dynamic structure factor in terms of a single peak is accurate only in the phonon region, while the secondary multiphonon branch gives a relevant contribution at large wave vectors, especially for strongly interacting systems.

3.3.7 Static density response function

In our study, we also calculate the static density response function $\chi(\boldsymbol{q})$. This quantity describes the linear response in density to a weak perturbation which is spatially modulated with a wave vector $\boldsymbol{q}$. In the limit $q \to 0$, $\chi(\boldsymbol{q})$ converges to the isothermal compressibility [68]. From the knowledge of the dynamic structure factor, the static density response function can be obtained using the following formula:

$$\chi(\boldsymbol{q}) = -2n \int_0^\infty \mathrm{d}\omega \, \frac{S(\boldsymbol{q},\omega)}{\omega} \,. \tag{3.12}$$

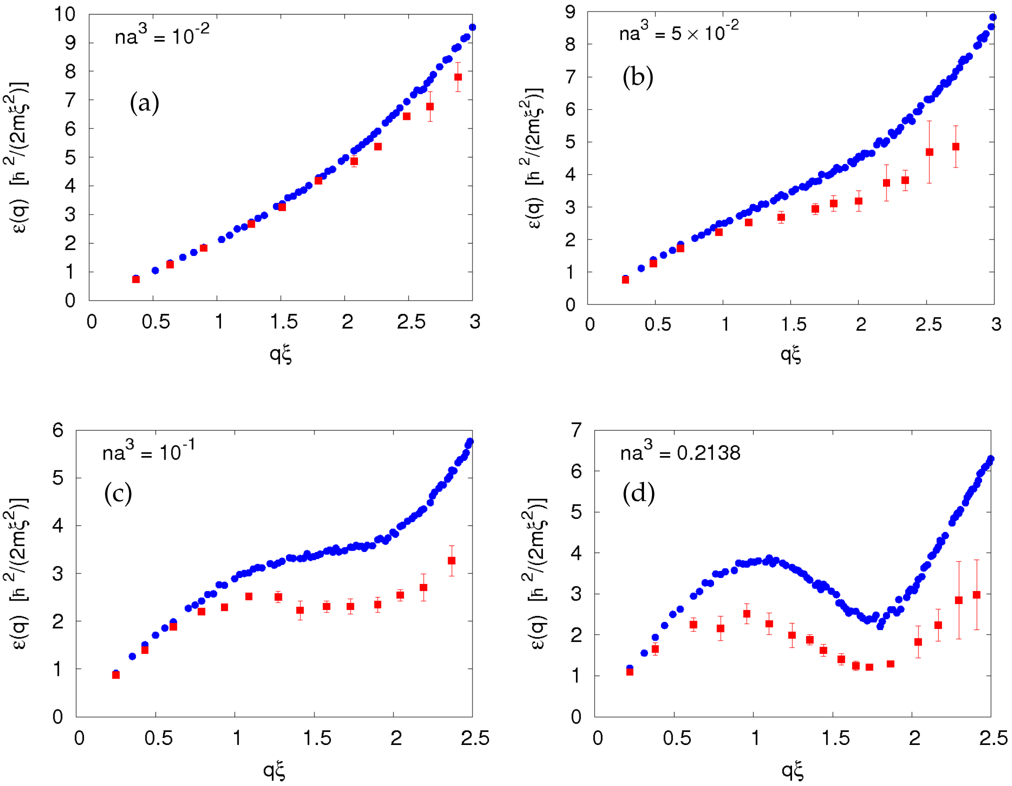

Figure 3.10 Spectrum of the elementary excitations $\varepsilon(\boldsymbol{q})$ of the HS-gas for different values of the gas parameter: $na^3 = 10^{-1}$ (panel a), $na^3 = 5 \times 10^{-2}$ (panel b), $na^3 = 10^{-1}$ (panel c), $na^3 = 2.138 \times 10^{-1}$ (panel d). GIFT results (red squares) are compared with the estimation of $\varepsilon_F(\boldsymbol{q})$ provided within the Feynman approximation 3.3 (blue circles). Where not shown, statistical uncertainties are below the symbol size.

In Fig. 3.11 on the next page we present the static density response function calculated from the reconstructed dynamic structure factors of the HS system for different gas parameters. In the weakly interacting regime ($na^3 = 10^{-4}$), $\chi(\boldsymbol{q})$, for the available wave vectors, is monotonically decreasing, consistently with the behavior of the dilute gas. Comparing our numerical results with the curve for $\chi(\boldsymbol{q})$ obtained within the mean-field approximation based on the Bogoliubov dispersion 3.2, that is

$$\chi(\boldsymbol{q}) = \frac{2m\xi^2}{\hbar}\frac{2}{(q\xi)^2 + 2}\,, \tag{3.13}$$

we notice an excellent agreement at large q, while at small q we find that the QMC estimates are systematically slightly below the mean-field prediction. This discrepancy may

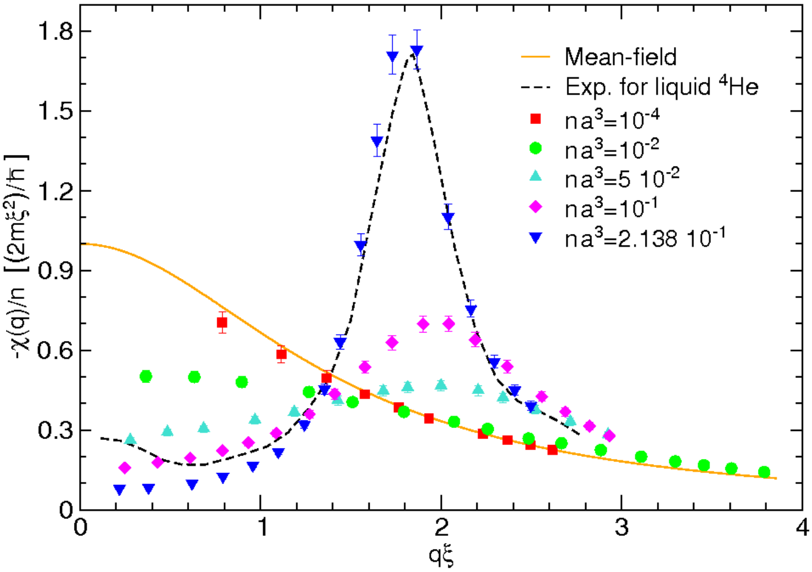

Figure 3.11 Static density response function $\chi(\boldsymbol{q})$ for the HS gas at different values of the gas parameter. The orange solid line is the mean-field result for $\chi(\boldsymbol{q})$ and the black solid line is the experimental static density response function of superfluid ^{4}He at SVP [88]. Where not shown, statistical uncertainties are below the symbol size.

be due to finite-size effects, which are not easy to evaluate since the set of the wave vectors q achievable in our QMC simulations depends on the geometry of the box and thus a calculation of $\chi(\boldsymbol{q})$ at the same q but with different sizes of the box is not straightforward. However, the statistical uncertainties of our results do not allow to exclude a statistical origin of such discrepancy.

By increasing the gas parameter, we observe a decreasing of the value of $\chi(\boldsymbol{q})$ at small q, which indicates a decreasing of the compressibility of the gas, while at intermediate values of q, we can see the emergence of a peak, which becomes clear for $na^3 = 10^{-1}$, i.e. the same gas parameter at which the roton minimum appears in $\varepsilon(\boldsymbol{q})$. The behavior displayed by the static density response function confirms that in a strongly interacting many–body Bose system, characterized by the presence of a hard-core interaction, the preferred modulation of the system, revealed by a peak in $\chi(\boldsymbol{q})$, corresponds to a wave vector in the vicinity of the roton minimum. Such peak is a precursor of a Bragg–like peak which appears during crystallization [89].

As we did for the dispersion relation of the elementary excitations, it is interesting to compare our numerical result for the static response function of the HS gas at na^3 =2.138 × 10^{-1} with the experimental measurements for superfluid ^{4}He at SVP [88]. As we can see in Fig. 3.11, there is a significant difference for $q\xi \lesssim 1.4$, which reflects a discrepancy in the compressibility, and thus in the speed of sound (see Fig. 3.6 on page 59), between the HS gas and superfluid ^{4}He. On the contrary, we can notice that, for momenta in the roton and post-roton regions, the agreement between the two curves is good. This result confirms the hypothesis that superfluid ^{4}He behaves like a HS system for wave vectors corresponding to the inverse of the mean interatomic distance and above [78].

3.3.8 Solid and metastable phases

For values of the gas parameter larger than the melting density, $n_m a^3 = 0.288(1)$, the thermodynamically stable phase is the crystal, while the gas state can only survive as a metastable phase (see Fig. 3.14 on page 69). In Fig. 3.12 on the facing page we show the dynamic structure factor in the metastable gas phase at $na^3 = 3 \times 10^{-1}$. We notice that the distribution of spectral weight is in general very broad and extends to relatively high frequencies. Only in the roton region a narrow quasiparticle peak is present accompanied by multiphonon excitations at higher frequencies. More details about the spectrum of excitations in the metastable gas phase can be extracted from Fig. 3.13 where we plot the dispersion of the central position of the highest peak as a function of the wave vector $\boldsymbol{q}$. The roton minimum is clearly evident at energies significantly lower than in the gas phase at $na^3 = 10^{-1}$ (see Fig. 3.6 on page 59). The small error bars indicate that the peak is indeed well defined in the region around the roton minimum corresponding to the energy gap Δ. The width of the peak increases dramatically as soon as the excitation energy is above the threshold 2Δ in agreement with the theoretical explanation in terms of two-roton quasiparticle decay processes. As already observed, this broadening occurs also at lower gas parameters for the wave vector regions in which the excitation energy is two times the roton energy gap.

Similarly to Fig. 3.6, the points corresponding to the smallest wave vectors available in our simulation box $q = 2\pi/V^{1/3}$ agree with the phonon dispersion $\hbar\omega(\boldsymbol{q}) = \hbar c q$, where the speed of sound c is estimated from the equation of state.

The wave vector dispersions of the highest peaks of $S(\boldsymbol{q}, \omega)$ in the fcc crystal phase at $na^3 = 3 \times 10^{-1}$ are shown in Fig. 3.13 on page 68 along three independent spatial directions. The three spectra agree at small momenta, where they all converge to the energy $\hbar\omega(\boldsymbol{q}) = c_L \hbar q$ of longitudinal phonons propagating with the speed c_L, while at larger values of $\boldsymbol{q}$ they differ significantly and the spectral intensities associated to them have a vanishing energy at different points corresponding to the wave vectors of the reciprocal lattice. Here, the spectral function is exhausted by the elastic peak at $\omega = 0$ and the static structure factor $S(\boldsymbol{q})$ diverges with the number N of particles in the system. We notice that, when the wave vector lies in the (1,1,1) direction and explores the diagonal of the elementary cell, the smallest non-zero wave vector of the reciprocal lattice is at $q \simeq 1.7/\xi$. The roton minimum in the metastable gas phase at the same value of the density of the solid is found very near this value of $\boldsymbol{q}$. The broad signals obtained in the central re-

(a) $S(\boldsymbol{q}, \omega)$ at three fixed $\boldsymbol{q}$

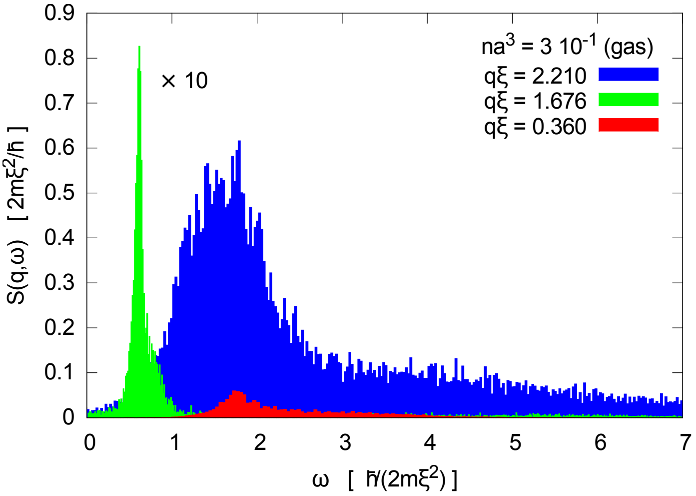

(b) Color map of $S(\boldsymbol{q}, \omega)$

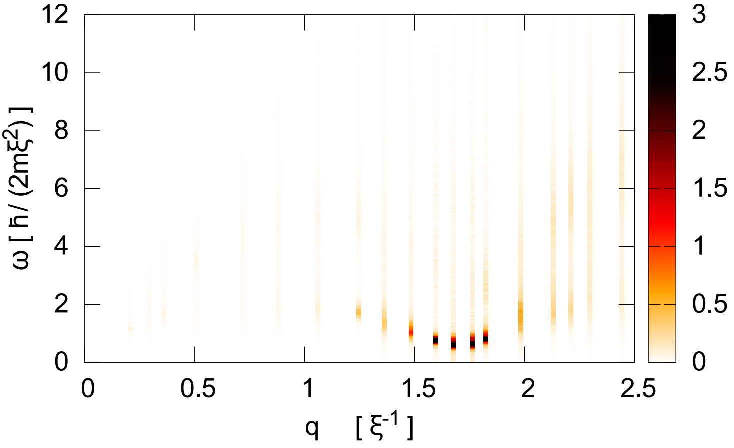

Figure 3.12 Dynamic structure factor at $na^3 = 3 \times 10^{-1}$. **(a)** $S(\boldsymbol{q}, \omega)$ for three values of the wave vector q. The signal corresponding to $q = 1.676/\xi$ is rescaled by a factor 0.1. **(b)** Color map of $S(\boldsymbol{q}, \omega)$ as a function of q; we set to 1 the maximum value of the color scale in the contour plot, in order to show the contributions at low spectral weight.

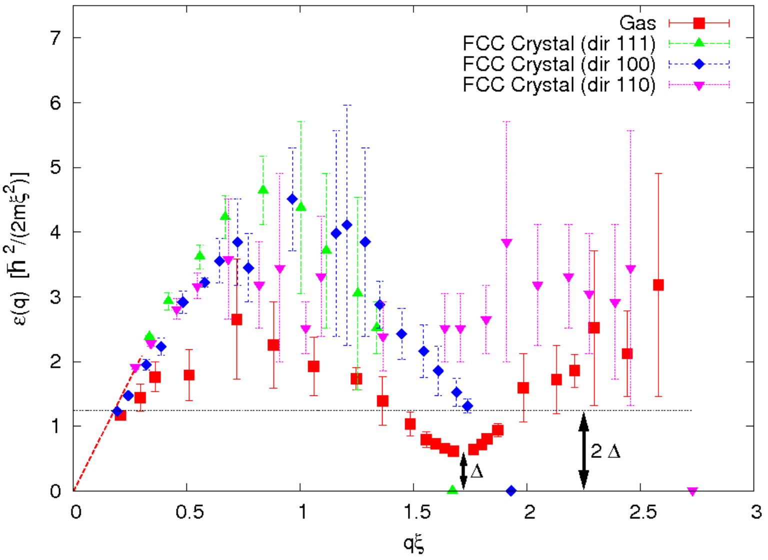

Figure 3.13 Dispersion of the central position of the highest peak in $S(q,\omega)$ at $na^3 = 3 \times 10^{-1}$ in the metastable gas phase (red squares) and in the fcc crystal phase: direction (1,1,1) green up triangles, direction (1,0,0) blue diamonds, direction (1,1,0) magenta down triangles. Similarly to Fig. 3.6 on page 59, the dashed line shows the phonon dispersion $\hbar cq$ in the gas phase. The horizontal dotted line corresponds to twice the roton gap Δ.

gion of the Brillouin zone presumably arise from the fact that the energies of the three branches are not well separated from the higher phonon bands and the GIFT method cannot resolve the different contributions to the dynamic structure factor.

3.4 Other Static properties

Simulations are carried out starting from configurations distributed according to the gas and solid wave functions, respectively Eqs. 3.8 and 3.9. Different system sizes are simulated: up to $N = 300$ in the gas and to $N = 500$ in the solid, and the corresponding energies are extrapolated to the thermodynamic limit using a linear $1/N$ fit.

3.4.1 Equations of state of gas and solid phases

The results for the energy of the two phases, in the region close to the gas–to–solid phase transition, are shown in Fig. 3.14 on the next page. The PIGS method has been shown to be able to generate the correct ground state of the system irrespective of the starting configuration and of the trial wave function utilized [34, 90]. However, for values of the gas parameter close to the gas–to–solid transition, we are able to stabilize the metastable

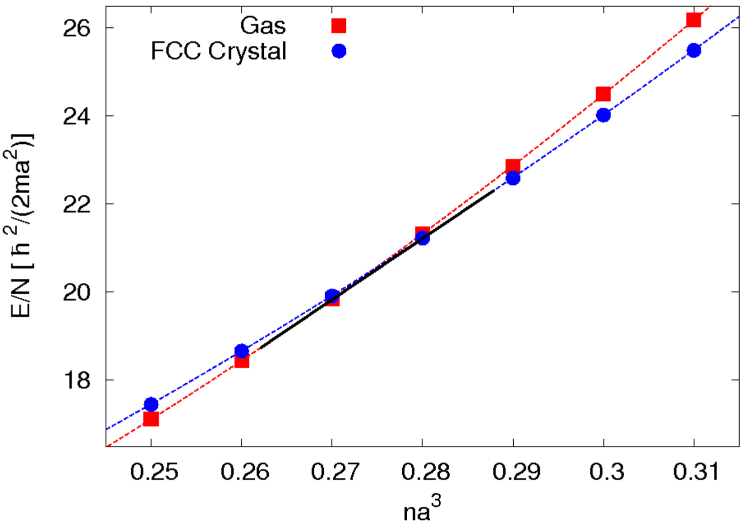

Figure 3.14 Equation of state of the gas (red symbols) and of the fcc crystal (blue symbols) as a function of the gas parameter na^3. Dashed lines are polynomial fits to the PIGS results for the two phases: for the gas phase, the PIGS data is fitted with the equation $E_G = A_G(na^3 - \rho_G)^2 + E_{0,G}$, with $A_G = 357.5(51)$, $\rho_G = 0.0686(29)$, $E_{0,G} = 5.35(21)$; for the solid phase, the PIGS data is fitted with the equation $E_S = A_S(na^3 - \rho_S)^2 + E_{0,S}$, with $A_S = 272.7(60)$, $\rho_S = 0.0342(54)$, $E_{0,S} = 4.76(37)$ (the values of A_G, $E_{0,G}$, A_S and $E_{0,S}$ are in units of $\hbar^2/(2ma^2)$, the parameters ρ_G and ρ_S are dimensionless). The black solid line corresponds to the double tangent construction and its low and high density ending points indicate respectively the values of the freezing (n_f) and melting (n_m) densities.

solid and gas phase (see Fig. 3.14) thanks to a proper choice of the initial configuration and of the number of beads M. From the value of the static structure factor $S(\boldsymbol{G})$ calculated at the reciprocal lattice vectors $\boldsymbol{G}$, we check that the configurations obtained from the PIGS method are belonging to the solid or to the gas branch. By applying the Maxwell construction to the equation of state of the gas and of the solid we accurately determine the freezing, $n_f a^3 = 0.262(1)$, and melting densities, $n_m a^3 = 0.288(1)$, which are in agreement with previous findings [2, 80, 91]. Recently, the freezing and the melting densities of the HS system have been determined in another PIGS calculation [92]: the results obtained in this work are in good agreement with ours. We remark that, in the range of densities studied, the energies of the bcc and hcp crystal are found to coincide, within our statistical uncertainty, with the ones reported in Fig. 3.14 for the fcc solid.

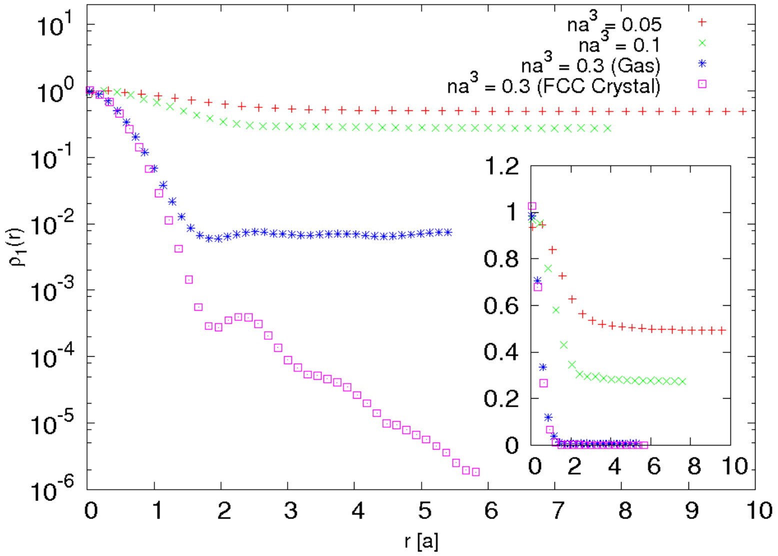

Figure 3.15 Radial dependence of the OBDM for different values of the gas parameter in the gas and in the solid phase. The same curves are shown in logarithmic scale (main figure) and in linear scale (inset).

3.4.2 One body density matrix

In Fig. 3.15 we show the data corresponding to the OBDM both in the gas and in the solid phase. In the gas, the plateau reached at large distances corresponds to the condensate fraction $n_0 = N_0/N$, where N_0 is the number of particles occupying the $\boldsymbol{k} = 0$ single-particle state. We notice that n_0 decreases by increasing the density, but remains finite in the gas branch even in the metastable region. On the contrary, in the solid the condensate fraction vanishes, showing that off-diagonal long-range order in the OBDM does not survive when translational symmetry is broken in the HS system. It has been recently shown that in repulsive models of bosons with a soft core, n_0 can remain finite in the crystal phase realizing the so called supersolid state [93, 94].

3.5 Conclusions

In this work, we have estimated the dynamic structure factor and the spectrum of elementary excitations for Bose HS gases at zero temperature, ranging from the dilute to the dense regime, by means of *ab-initio* calculations based on QMC methodologies. The numerical approach followed, which makes use of the GIFT algorithm to perform the analytical continuation of the "exact" PIGS results for the imaginary time correlation functions, is one of the most powerful methods presently available and allow us to get very accurate results for the spectral functions, even for strongly interacting systems, where it is difficult to describe properly all the relevant correlations arising among the quantum particles. We have been able to see, in the dispersion of the elementary excitations, a crossover from the Bogoliubov spectrum, predicted in mean-field theories and accurate for weakly interacting gases, to the phonon-maxon-roton spectrum, experimentally seen in dense Bose liquids, such as superfluid ^{4}He. We also show that, for large values of the wave vector of the density fluctuation, the dynamic structure factor presents a broad multiphonon contribution at high frequencies, which becomes relevant as the density of the system increases, making quantitatively inaccurate the Feynman's approximation for the spectrum of the elementary excitations. Remarkably, for $na^3 = 2.138 \times 10^{-1}$, the gas parameter corresponding to superfluid ^{4}He at equilibrium density, the hard-sphere model turns out to describe accurately the energy–momentum dispersion relation and the static density response of superfluid ^{4}He in the roton region; this suggests that, for wavelengths comparable to interatomic distances, the low–energy dynamic properties are dominated by the hard-core repulsive part of the interaction potential.

CHAPTER 4

Freezing of superfluid ^{4}He and dynamics of normal quantum liquids

4.1 Introduction

One of the approaches for investigating the superfluid–solid phase transition in helium-4 is the *density-functional theory* (DFT) of freezing [23, 95]. A DFT computation, though, requires inputs provided by other techniques, e.g. quantum Monte Carlo (QMC) methods: the static density-response function $\chi(\boldsymbol{r} - \boldsymbol{r}')$ and the equation of state of the system. DFT is known to successfully describe the freezing of various classical liquids [23]; however, it has been widely discussed and verified that DFT gives unphysical results when applied to superfluid ^{4}He, even when reliable input is obtained with QMC simulations [96, 97].

The DFT of freezing approaches the problem from the liquid side and views the crystal as a liquid with modulated density [95]. Within this approach the free energy of an inhomogeneous system is uniquely determined from the properties of its homogeneous counterpart. Different theories were developed to approximate the free energy functional; the most common are a second order truncation (SOT) theory of Ramakrishnan-Yussouff type [97, 98] and a non-perturbative theory called modified weighted density approximation (MWDA) [91]. In the first approach, the difference in free energy ΔF between the solid and the liquid phase is obtained by a Taylor expansion truncated to second order with respect to the density modulation. Whilst MWDA gives ΔF using a weighted density so that a subset of higher order terms beyond SOT are included. For superfluid ^{4}He at $T = 0$ and freezing density $\rho_{\mathrm{fr}} = 0.0262\,\text{Å}^{-3}$, the SOT method gives a too stable solid and fails to obtain superfluid phase [97, 99], whereas the MWDA approach give a too stable superfluid and fails to result in solid phase [100].

In our work carried out in collaboration with T. Minoguchi, and published in Ref. [52], we introduced a modification regarding the input required by the MWDA. Since the bulk solid ^{4}He has zero condensate [7, 39, 101], we proposed to consider the solid as a modulated "normal" liquid instead of a modulated superfluid. Therefore, we had assumed the input for the MWDA to be that of a liquid made of distinguishable ^{4}He atoms, that is a

Boltzmann liquid (or liquid of *boltzmannons*), at temperature well below that of superfluid transition T_λ and density near to that of freezing ρ_{fr}.

One could think that a more natural way to calculate the input quantities of normal liquid ^{4}He, with zero condensate, is to simulate the system at $T > T_\lambda$. We must not forget, though, that we simulate finite systems, and if we investigate the system at temperature just above T_λ, the superfluid fraction will be finite (i.e. the winding number will be finite), that is the system will be still superfluid. And if we move to higher temperature to avoid the finite size effects, we will go away from the solid phase, as the liquid–solid transition line goes to pressures much higher. So to prevent superfluidity staying at low temperature, we had removed the Bose symmetry.

We performed path integral Monte Carlo (PIMC) simulations (see Chapter 1 for details) to obtain the equation of state of the Boltzmann liquid and the static density-response function $\chi(q)$ at density $\rho_\ell = 0.0253\,\text{Å}^{-3}$ (the reason for this choice will be explained below) in the metastable liquid phase, always at temperature $T = 1\,\mathrm{K}$. These quantities were exploited by our collaborator to perform the MWDA calculations. In the next section, I will explain how we computed those quantities for a liquid ^{4}He system in which the Bose condensate is suppressed and illustrate the results. In Section 4.3 I will give details about the MDWA DFT approach, the obtained results and their discussion. In the last section, I will draw our conclusions.

4.2 Simulations of the *Boltzmann liquid*

As mentioned above we computed with PIMC method $\chi(q)$ and the energy per particle, defined later, $e(\rho)$, that are needed for the MWDA calculations, and also the static and dynamics structure factors $S(\boldsymbol{q})$ and $S(\boldsymbol{q},\omega)$, for a system of distinguishable particles (Boltzmann liquid). To simulate such system we have to prevent the exchanges between ^{4}He atoms. In practice we have to switch off the Metropolis moves—permutations, swaps—operated within our PIMC implementation with the Worm algorithm and explained in detail in Section 1.4 which guarantee the Bose symmetry.

In order to obtain a suitable input for the MWDA calculations, our PIMC simulations were aimed at computing properties of the Boltzmann liquid ^{4}He near the superfluid freezing density, $\rho_{\mathrm{fr}} = 0.0262\,\text{Å}^{-3}$, at $T = 1\,\mathrm{K}$, a temperature below the λ point. To simulate effectively the Boltzmann liquid near the freezing point, we used $N = 179$ atoms, thus inserting a vacancy into a possible hcp solid, for which $N = 180$ atoms form a commensurate solid, and enhancing the liquid phase. As interaction potential we adopted an Aziz potential [104]. We found that above $\rho_\ell = 0.0247\,\text{Å}^{-3}$, well below ρ_{fr} of the real system, the system underwent solidification. This showed, in agreement with the results reported by Boninsegni et al. [12], that Bose symmetry has a fundamental role, together with zero-point motion, in determining the liquid–solid phase boundary. However, since

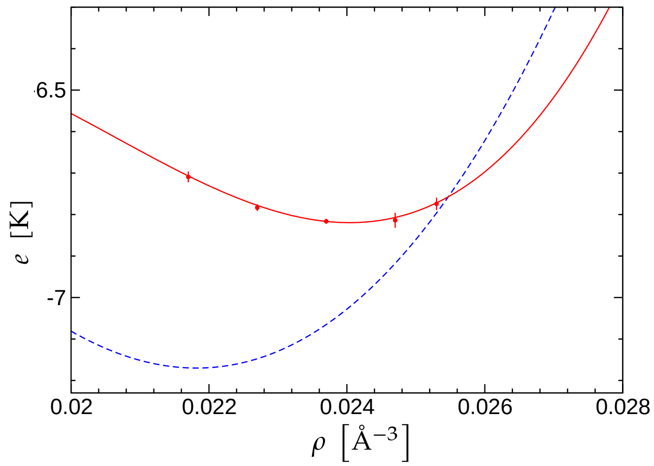

Figure 4.1 Internal energy per particle $e(\rho)$ versus density computed at $T = 1\,\text{K}$ for the Boltzmann liquid ^{4}He. The two rightest points are relative to the boltzmannon system in metastable liquid phase. The red line is the quadratic fit of the data (see text). The blue line is the experimental data [102] at $T = 50\,\text{mK}$, which is very close to superfluid ^{4}He at zero temperature [103].

we needed to obtain the required input at densities of freezing, i.e. near $\rho_{\text{fr}} = 0.0262\,\text{Å}^{-3}$, we considered the simulation of the system in metastable liquid phase using the following procedure. We started the simulations from liquid-like configurations obtained rescaling in density (by shortening proportionally all distances between ^{4}He atoms) configurations of a liquid system simulated at lower density. After the equilibration stage, the disordered phase was found persistent, with no sign of crystallization as inferred from the static structure factor (see Fig. 4.2 on the next page) and from visual examinations of the ring-polymer configurations during the simulation. Metastable phase of the Boltzmann liquid turned out to be accessible for densities up to $0.0253\,\text{Å}^{-3}$. At higher densities the system starts homogeneous nucleation processes within a few thousand Monte Carlo (MC) steps.

For the purpose of determining the equation of state as MWDA input, we computed the energy per particle $e(\rho) = E(\rho)/N$ of the Boltzmann liquid ^{4}He at several values of the density, obtaining the results shown in Fig. 4.1. We fitted the computed data using a cubic polynomial,

$$e(\rho) = e_0 + \alpha\left(\frac{\rho}{\rho_0} - 1\right)^2 + \beta\left(\frac{\rho}{\rho_0} - 1\right)^3, \tag{4.1}$$

with the fit parameters, $e_0 = -6.8192(32)\,\text{K}$, $\rho_0 = 0.023\,994(86)\,\text{Å}^{-3}$, $\alpha = 13.6(19)\,\text{K}$ and $\beta = 17(24)\,\text{K}$; the fitting curve is also shown in Fig. 4.1.

Through the PIMC simulations we computed also at the same densities ρ the static structure factor $S(\boldsymbol{q})$. In Fig. 4.2 on the next page $S(\boldsymbol{q})$ is shown for two densities. As it

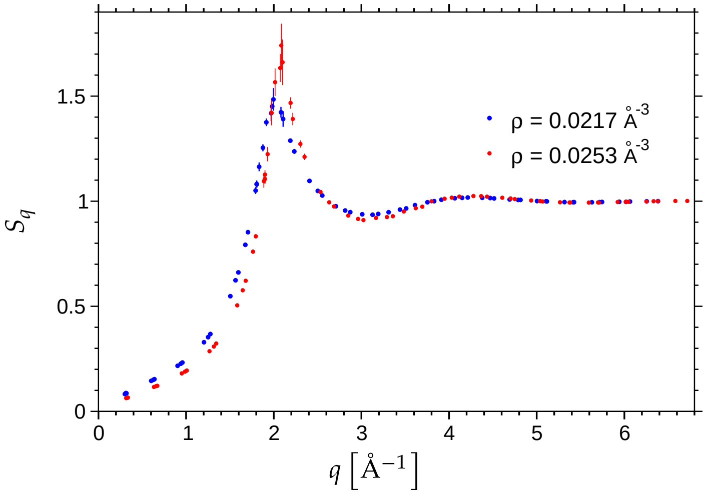

Figure 4.2 Static structure factor of Boltzmann liquid at $T = 1\,\text{K}$ and at density $\rho = 0.0217\,\text{Å}^{-3}$ (blue points) and $\rho = 0.0253\,\text{Å}^{-3}$ (red points).

is reported in the literature [4], the effect of the Bose statistics in the radial distribution function $g(r)$ is minimal. In fact, we obtained for the Boltzmann liquid an $S(\boldsymbol{q})$ similar to that presented in literature [4].

The density response function $\chi(\boldsymbol{q})$, required for the MWDA calculations, as explained in Section 2.3, is obtained from the dynamic structure factor $S(\boldsymbol{q},\omega)$, by an integration over ω of $S(\boldsymbol{q},\omega)$ divided by ω,

$$\chi(\boldsymbol{q}) = -2\rho \int_{-\infty}^{+\infty} \mathrm{d}\omega\, \frac{S(\boldsymbol{q},\omega)}{\omega}\,, \tag{4.2}$$

i.e. $\chi(\boldsymbol{q})$ is proportional to the first inverse moment of $S(\boldsymbol{q},\omega)$. $S(\boldsymbol{q},\omega)$ is extracted from the intermediate scattering function $F(\boldsymbol{q},\tau)$ defined in Chapter 2, computed with the PIMC method, by means of the genetic inversion via falsification of theories (GIFT) method, as widely explained in Chapter 2, extended for this work to finite temperature (see Section 2.8). To compute $F(\boldsymbol{q},\tau)$ needed to obtain $\chi(\boldsymbol{q})$, we carried out PIMC simulations of the boltzmannon liquid in metastable phase at density $\rho = 0.0253\,\text{Å}^{-3}$. We would have been interested in studying higher densities, but among the explored densities (see the points in Fig. 4.1) this is the higher density we was able to simulate the system in the metastable phase.

In Fig. 4.3 and in Fig. 4.4 I show $S(\boldsymbol{q},\omega)$ for some wave vectors (the values of q are reported in the legends) as example of spectral functions recovered with GIFT and used to calculate $\chi(\boldsymbol{q})$. As one can see in Fig. 4.3 on the facing page, $S(\boldsymbol{q},\omega)$ presents for small $\boldsymbol{q}$ ($q \simeq 0.32, 0.33$) three closely-spaced sharp structures, in which the second and the third are very close together. Conformations with three structures also appear for many of the wave vectors at which $S(\boldsymbol{q},\omega)$ is extracted, as one can also see in Fig. 4.4.

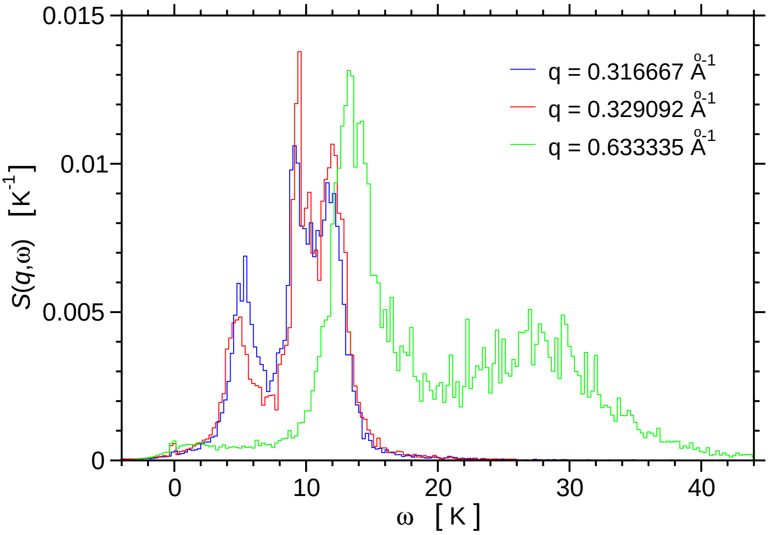

Figure 4.3 Dynamic structure factor of Boltzmann liquid at $T = 1\,\mathrm{K}$ and at density $\rho = 0.0253\,\text{Å}^{-3}$ for three different low wave vectors q.

In order to try to give a physical meaning to these patterns, we can suppose that the most part of spectral weight of $S(\boldsymbol{q},\omega)$, at small wave vectors q, is associated with phonon-like excitations. In fact, as one can see in Fig. 4.2 $S(\boldsymbol{q})$ is roughly linear at small wave vectors, and since a sound shall be present in this system, we can exploit the result relative to $S(\boldsymbol{q})$ to estimate the velocity of sound. We can approximate $S(\boldsymbol{q})$ to a straight line through the origin for $\boldsymbol{q} \to 0$, i.e. $S(\boldsymbol{q}) \simeq \hbar q/(2mv_s)$, where v_s is the velocity of first sound. With this assumption we have fitted $S(\boldsymbol{q})$ at the first three wave vectors, which are very near to each other, with a straight line through the origin and we have obtained $v_s = 403(2)\,\mathrm{m\,s^{-1}}$, that is a reasonable value for ^{4}He near the freezing density ($v_s \sim 370\,\mathrm{m\,s^{-1}}$ from Fig. 10 in Ref. [105]). Now, we make the rough approximation that the dynamic density fluctuations at low q are dominated by a single collective mode, the phonon mode. To estimate the energy of phonon excitations, we can exploit the value of the velocity of sound so calculated by approximating the excitation energies with a linear dispersion $\varepsilon(\boldsymbol{q}) = \hbar v_s q$. In this way, for the first two wave vectors $q = 0.316\,667\,\text{Å}^{-1}$ and $q = 0.329\,092\,\text{Å}^{-1}$, we obtain respectively the values $\varepsilon(\boldsymbol{q}) = 9.75(5)\,\mathrm{K}$ and $\varepsilon(\boldsymbol{q}) = 10.14(5)\,\mathrm{K}$. We have actually found that these values fall on the higher structure of $S(\boldsymbol{q},\omega)$, as we can see in Fig. 4.3. However, we note that this structure (or one of the others) doesn't have the most spectral weight of $S(\boldsymbol{q},\omega)$ (i.e. the area under $S(\boldsymbol{q},\omega)$, see Fig. 4.3). So, even only at small q, the interpretation of the pattern of

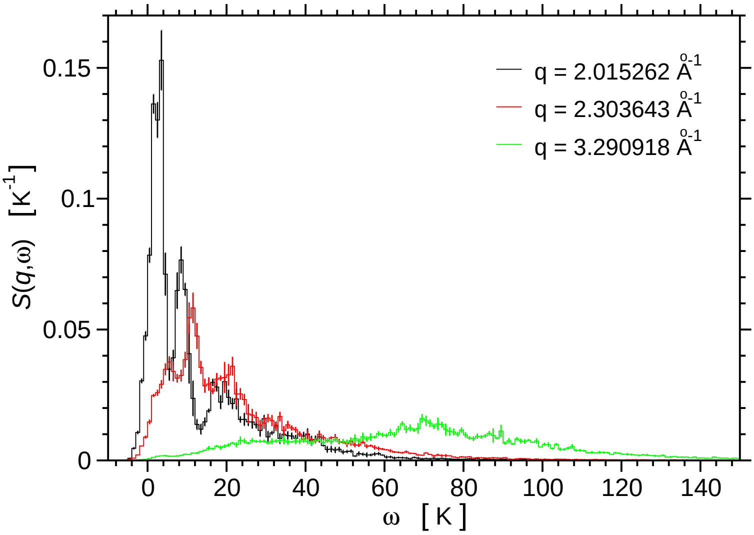

Figure 4.4 Dynamic structure factor of Boltzmann liquid at $T = 1\,\mathrm{K}$ and at density $\rho = 0.0253\,\text{Å}^{-3}$ for three different wave vectors q.

$S(\boldsymbol{q},\omega)$ is quite complicated. On the other hand, the GIFT algorithm cannot allow access to the exact form of $S(\boldsymbol{q},\omega)$. The structures are close to each other, so it is dangerous to attempt to deduce some more quantitative information, since we cannot be completely confident with the shape of $S(\boldsymbol{q},\omega)$ obtained in this case.

The static density-response function $\chi(\boldsymbol{q})$ calculated for Boltzmann liquid ^{4}He at density $\rho = 0.0253\,\text{Å}^{-3}$ is shown in Fig. 4.5 on the next page with blue points both in linear scale and logarithmic scale. In the same figure I also show $\chi(\boldsymbol{q})$ for superfluid ^{4}He at $T = 0$, obtained in a previous work [99]. It is interesting to note that the peak of $\chi(\boldsymbol{q})$ for the liquid of boltzmannons is nearly twice that of the superfluid ^{4}He at $T = 0$. This implies that, either the Boltzmann statistics or the lack of Bose statistics destabilize the system against density deformations at a finite wave number. This feature is what we need to improve the MWDA results at freezing in order to predict the experimentally observed solid phase. Indeed, it is reasonable to suppose that the removal of the particle permutations contributes to localize the particles and therefore favors the crystallization. Moreover, I also remind the reader that the static density response function $\chi(\boldsymbol{q})$ represents the response of the system to an external periodic perturbation with wave vector $\boldsymbol{q}$, that tends to localize particles, as it occurs in crystals. Hence, the particles are more localized if $\chi(\boldsymbol{q})$ is higher for wave vectors $\boldsymbol{q}$ corresponding to the wave lengths ($\lambda = 2\pi/q$), on the scale of the interatomic distances.

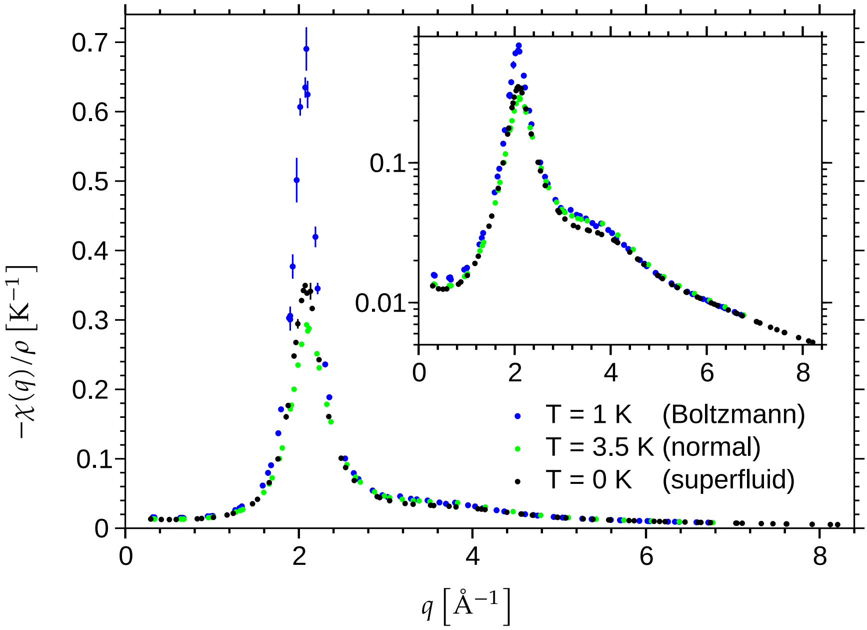

Figure 4.5 Static density-response function for Boltzmann liquid at density $\rho = 0.0253\,\text{Å}^{-3}$ and $T = 1\,\mathrm{K}$ (blue points) and at $\rho = 0.026\,\text{Å}^{-3}$ and $T = 3.5\,\mathrm{K}$ (green points), and superfluid at $\rho = 0.026\,\text{Å}^{-3}$ and $T = 0\,\mathrm{K}$ [99](black points). (inset) Same figure of the large one but in logarithm scale.

Previously, in order to improve the MWDA results obtained at $T = 0$ [100], we had considered to simulate ^{4}He in the normal liquid phase, to obtain the input for DFT calculations, for the reasons discussed above in the first section. So, we have first simulated the system at $T = 2.5\,\mathrm{K}$, i.e. at $T > T_\lambda$, but, as discussed in Section 4.1, due to finite size effects this system has still a non-zero superfluid fraction. Then we simulated the normal liquid at $T = 3.5\,\mathrm{K}$, but it produced a $\chi(\boldsymbol{q})$ with a peak even smaller than that of superfluid at $T = 0$, as one can see in Fig. 4.5. Actually at this temperature the liquid-solid transition line tends to go far away toward higher pressures, and as a result the density response softens. While in order for MWDA to predict the freezing of superfluid ^{4}He, a higher density response to modulation is necessary. The temperature has the effect to reduce the system response. From Fig. 4.5 we can observe, furthermore, that the peak $\chi(\boldsymbol{q})$ for the Boltzmann liquid ^{4}He at $T = 1\,\mathrm{K}$, i.e. at $T < T_\lambda$, is more than twice as high as that of the normal liquid at $T = 3.5\,\mathrm{K}$.

4.3 MWDA calculation for the freezing of the Boltzmann liquid

I report here a summary of the DFT calculations carried out by our collaborator (T. M.).

The MWDA [106, 107] gives a recipe to approximate the free energy $F[\rho]$ of the solid (system with modulated density $\rho(r)$) in terms of the known correlation free energy of the homogeneous liquid $F_{\mathrm{c}}[\rho_\ell] = N f_{\mathrm{c}}(\rho_\ell)$ (ρ_ℓ is the constant density of a homogeneous liquid):

$$F[\rho] = F_{\mathrm{id}}[\rho] + F_{\mathrm{c}}[\rho] \simeq F_{\mathrm{id}}[\rho] + F^{\mathrm{MWDA}}[\rho] = F_{\mathrm{id}}[\rho] + N f_{\mathrm{c}}(\tilde{\rho}), \tag{4.3}$$

where $\tilde{\rho}$ is an effective (constant) liquid density obtained from the modulated density $\rho(r)$ through an appropriate weighted average, that will be defined below; F_{id} is the free energy functional of the non-interacting system (ideal gas) at a generic modulated density; and F_{c} is the correlation free energy functional, which 4.3 is approximated by MWDA. The weight function yielding $\hat{\rho}$ is self-consistently determined to make the second order functional derivative of $F_{\mathrm{c}}^{\mathrm{MWDA}}[\rho]$, evaluated on the uniform liquid density, to coincide with the difference of static density-density response functions given below,

$$\left.\frac{\delta^2 F_{\mathrm{c}}^{\mathrm{MWDA}}[\rho]}{\delta\rho(\boldsymbol{r}_1)\delta\rho(\boldsymbol{r}_2)}\right|_{\rho(r)=\rho_\ell} = -\left[\chi^{-1}(\boldsymbol{r}_1 - \boldsymbol{r}_2;\rho_\ell) - \chi_{\mathrm{id}}^{-1}(\boldsymbol{r}_1 - \boldsymbol{r}_2;\rho_\ell)\right], \tag{4.4}$$

where

$$\chi_{\mathrm{id}}^{-1}(\boldsymbol{r}_1 - \boldsymbol{r}_2;\rho_\ell) = \left.\frac{\delta^2 F_{\mathrm{id}}[\rho]}{\delta\rho(\boldsymbol{r}_1)\delta\rho(\boldsymbol{r}_2)}\right|_{\rho(r)=\rho_\ell} \quad \text{and} \quad \chi^{-1}(\boldsymbol{r}_1 - \boldsymbol{r}_2;\rho_\ell) = \left.\frac{\delta^2 F[\rho]}{\delta\rho(\boldsymbol{r}_1)\delta\rho(\boldsymbol{r}_2)}\right|_{\rho(r)=\rho_\ell} \tag{4.5}$$

are the inverse of density static response functions, respectively, of the ideal gas and the uniform liquid at density ρ_ℓ.

Consider a density modulation which is characterized by a set of Gaussian functions periodically located in space

$$\rho(\boldsymbol{r}) = \sum_i \left(\frac{\alpha}{\pi}\right)^{3/2} e^{-\alpha|\boldsymbol{r}-\boldsymbol{R}_i|^2}. \tag{4.6}$$

In order to study the freezing of ^{4}He, $\{\boldsymbol{R}_i\}_i$ are assumed to be the crystalline lattice sites of an fcc lattice, which is known to be an accurate approximation of the ^{4}He hcp crystal. The distortion of the liquid is thus defined by two parameters: the atomic localization α and the density ρ_{s}, average of the density $\rho(\boldsymbol{r})$ 4.6 for the solid ^{4}He. Denton et al. considered the case of a classical liquid [106] and a zero temperature hard sphere (HS) boson system [107] and gave a self-consistent equation to determine $\tilde{\rho}$ as a function of $(\rho_{\mathrm{s}}, \alpha)$. Eq. 4.4 implies that the density static-response function of the non-uniform liquid implicitely depends on that of the uniform liquid. In the case of the freezing of a superfluid, however, we need to take special care in treating the relation 4.4, because the Bose condensate changes (i.e. decreases) with increasing the density modulation amplitude $|\delta\rho|$. In fact, it is known that Bose condensate is zero in perfect solid ^{4}He [7, 39, 101]. To better describe the problem under investigation, the relation 4.4 was employed, with

$\chi(\boldsymbol{r}_1-\boldsymbol{r}_2;\rho_\ell)$ set to be the density static-response function of the Boltzmann liquid ^{4}He and $\chi_{\rm id}(\boldsymbol{r}_1-\boldsymbol{r}_2;\rho_\ell)$ that of the non-interacting case of the same system.

Concerning the freezing of a Boltzmann liquid at finite temperature, we obtain an equation similar to the one of Denton et al. [106, 107] to find $\tilde{\rho}$. That is, in Fourier space,

$$\tilde{\rho}(\rho_{\rm s};\alpha)=\rho_{\rm s}\left[1+\frac{1}{2f_{\rm c}'(\tilde{\rho})}\sum_{\boldsymbol{G}\neq 0}{\rm e}^{-\frac{G^2}{2\alpha}}\left(-\chi^{-1}(G;\tilde{\rho})+\chi_{\rm id}^{-1}(G;\tilde{\rho})\right)\right], \tag{4.7}$$

where $\{\boldsymbol{G}\}$ are the reciprocal lattice vectors of the fcc crystalline lattice and $G=|\boldsymbol{G}|$. The thermal effects are included in $\chi(G;\rho)$, $\chi_{\rm id}(G;\rho)$ and $f_{\rm c}'(\rho)$, which is the first derivative of the correlation free energy per particle with respect to ρ. To be more explicit, we recall from Section 2.3 the expression of $\chi(\boldsymbol{q})$ in terms of dynamic structure factor $S(\boldsymbol{q},\omega)$:

$$\chi(G;\rho)=-2\rho\int_{-\infty}^{+\infty}{\rm d}\omega\,\frac{S(G,\omega;\rho)}{\omega}\,. \tag{4.8}$$

One can observe that in the Boltzmann system the intensity of $S(\boldsymbol{q},\omega;\rho)$ at the reciprocal vectors $\{\boldsymbol{G}\}$ distributes broadly over ω, so we need a full integration with respect to ω to obtain $\chi(G;\rho)$ at $\rho=0.0253\,\text{Å}^{-3}$. As for the ideal gas response, by putting

$$S(q,\omega;\rho)=\delta\left(\omega-\frac{\hbar q^2}{2m}\right), \tag{4.9}$$

we have

$$\chi_{\rm id}^{-1}(q;\rho)=-\frac{\hbar^2q^2}{4\,m\,\rho}\,. \tag{4.10}$$

Since the Helmholtz free energy (and its derivative with respect to density) is hard to obtain through PIMC computations, and was not calculated in the present study, we neglect thermal effect and approximate the free energy to the internal energy per particle:

$$f(\rho)\simeq e(\rho)\,. \tag{4.11}$$

This approximation may be justified by comparing the $\chi(\boldsymbol{q})$ of the Boltzmann system at different temperatures, say $T=1\,\rm K$ and $T=3.5\,\rm K$; the zero-wave-vector limit of the $\chi(\boldsymbol{q})$ is in fact related to the thermal compressibility and, as displayed in Fig. 4.5 on page 79, both functions have the same small $\boldsymbol{q}$ behavior within 12% of accuracy. The energy $e(\rho)$ of Boltzmann liquid can be easily computed with PIMC and is shown in Fig. 4.1. If we neglect the overlapping of Gaussians [107] we obtain

$$f_{\rm id}=\frac{3\,\hbar^2\alpha}{4\,m}\,. \tag{4.12}$$

To obtain $F[\rho]$ at given average density $\rho_{\rm s}$: (i) we substitute $\tilde{\rho}(\rho_{\rm s};\alpha)$ in Eq. 4.3 along with

$$F_{\rm id}[\rho_{\rm s}]=\frac{3\,\hbar^2\alpha\,\rho_{\rm s}}{4\,m\,V}\,; \tag{4.13}$$

(ii) and minimize $F[\rho]$ with respect to α. To perform the second procedure, however, $\chi(q;\rho)$ is needed for various densities ρ. Here we have $\chi(q;\rho)$ at just one density, $\rho = 0.0253\,\text{Å}^{-3}$, and the procedure (i) is presently all we can do. We are interested in $\rho_s = 0.029\,\text{Å}^{-3}$, which is the average density of solid ^{4}He at melting. With use of $\chi(q;\tilde{\rho})$ at $\tilde{\rho} = 0.0253\,\text{Å}^{-3}$, we obtain $\alpha = 0.387\,\text{Å}^{-2}$. Here we have taken the summation in Eq. 4.7 over $\{\boldsymbol{G}\}$ up to 12th shell. It turns out that $f = -3.35\,\text{K}$, which is the $F[\rho_s]$ per particle: the Gaussian deformed Boltzmann liquid at average density $\rho_s = 0.029\,\text{Å}^{-3}$ with $\alpha = 0.387\,\text{Å}^{-2}$ has free energy $f = -3.35\,\text{K}$.

As shown in Fig. 4.1 on page 75, the uniform superfluid energy per particle at $\rho_\ell = 0.0262\,\text{Å}^{-3}$, which is the experimentally observed freezing density at zero temperature, is $-6.5\,\text{K}$, which is much lower than f of the modulated Boltzmann liquid. This roughly means (although a rigorous conclusion should be made with Gibbs free energy) that a spontaneous deformation from superfluid at $0.0262\,\text{Å}^{-3}$ to Boltzmann liquid at $\rho_s = 0.029\,\text{Å}^{-3}$, with Gaussian deformation $\alpha = 0.387\,\text{Å}^{-2}$, cannot occur at 1 K. The real solid at melting has $\alpha = 2.14\,\text{Å}^{-2}$ [108], which cannot be accessed with the Boltzmann liquid input currently obtained. In a previous work [100], $\chi(\boldsymbol{q})$ and $e(\rho)$ of superfluid ^{4}He were employed for the same density modulation $\rho_s = 0.029\,\text{Å}^{-3}$ and $\alpha = 0.387\,\text{Å}^{-2}$, but at $T = 0$, and they found that $f = -2.5\,\text{K}$, which is higher than the case of Boltzmann liquid distortion by about 1 K. This means that Bose condensate prevents distortion of density, which is consistent with a recent observation [12].

4.4 Conclusions and perspectives

From our results we obtain that Boltzmann liquid ^{4}He, compared to superfluid ^{4}He, is more compressible and energetically more susceptible to density distortions of any spatial modulation with wave vector $\boldsymbol{q}$. This property is indeed what improves the MWDA approach to better describe the freezing of ^{4}He.

We extracted the dynamic structure factor for Boltzmann liquid ^{4}He. $S(\boldsymbol{q},\omega)$ presents particular structures with three peaks in many regions of the wave vector q. With the computed PIMC data on the intermediate scattering function $F(\boldsymbol{q},\tau)$ and with the current GIFT method we are not confident enough with the recovered spectral functions, hence we cannot provide satisfying physical interpretations of all the features appeared in $S(\boldsymbol{q},\omega)$. Thus in future it would very interesting to investigate these unexplained features with more extensive PIMC computations. For example, we could estimate imaginary-time intermediate scattering functions more statistical precise and evaluated at finer imaginary times. In this way, eventual spurious effects in the extracted spectral functions due to the statistical uncertainties should reduce and, so, we would be more confident with the computed dynamic structure function.

Chapter 5

Supercooled mixtures of *para*-hydrogen and *ortho*-deuterium

5.1 Introduction

A fundamental open problem in condensed matter physics is that of understanding the stability of supercooled liquids with respect to crystallization [22]. Given that crystallization competes with glass formation, it is important to comprehend the mechanisms that govern the crystal growth in supercooled liquids, to allow for clarifying the nature of the transition to glass [25–29]. To date, colloidal suspensions have generally been used in experimental studies that have sought to provide microscopic insights into the supercooled liquid dynamics and crystallization [109, 110]. With this systems, the large particle size makes possible to follow the crystal growth on the laboratory time scale. There are various drawbacks to this approach, however, starting with disperse systems and sedimentation. These phenomena make it difficult to interpret the data obtained [110, 111]. Another possibility is to access the details of the crystallization process in simple atomic and molecular counterparts. This is challenging, because the time scales of the experiments are shorter by orders of magnitude.

It has been shown in theoretical studies that a further degree of complexity in the behavior of supercooled liquids is added by the inclusion of quantum effects; this produces new exotic phenomena such as superfluidity [112, 113] or enhanced dynamical slowing down Yet again, until recently [30]), studies of the interplay between quantum effects and structural transformations in non-equilibrium liquids had been precluded by the experimental difficulties in supercooling a quantum liquid to very low temperatures.

To make progress in the understanding of these phenomena, the experimental groups of Frankfurt and Madrid, with which we collaborated, performed experimental studies (see Ref. [30]) to investigate the dynamics of crystallization of supercooled liquid p-H_2–o-D_2 mixtures. These experiments showed a strong slow-down of crystallization with increasing molar fraction of o-D_2 molecules in p-H_2 supercooled liquid. Since the two isotopic species of molecular hydrogen have the same interaction potentials and differ only in masses, this slow-down is purely due to quantum effects. To understand these results we provided our theoretical contribution by studying static structural properties in the supercooled metastable phase by means of Path Integral Monte Carlo simulations.

The properties exhibited by binary liquid mixtures are generally fundamentally different from their corresponding pure substances, and a common strategy to inhibit crystallization is to mix a few components. Indeed, the simplest theoretical models to investigate crystallization and glassy behavior in supercooled liquids are classical binary systems of particles that interact via a simple Lennard-Jones (LJ) pair potential [114–118]. Since p-H_2 and o-D_2 molecules have an even rotational quantum number J [119], their ground-state wave function is spherically symmetric. Thanks to this feature a p-H_2–o-D_2 mixture provides a neat molecular binary system in which the pair interactions can be described by the same isotropic LJ potential [119]. Isotopic p-H_2–o-D_2 mixtures thus offer a combination of intrinsic molecular simplicity and the possibility to experimentally explore quantum behavior in supercooled liquids. In fact, it is well-established that quantum effects influence the equilibrium thermodynamic and structural properties of the hydrogen liquids and solids [120]. The magnitude of quantum effects can be quantified by the dimensionless parameter, called de Boer parameter [121–123],

$$\Lambda = \frac{\hbar}{(\sigma\sqrt{m\,\varepsilon})}, \tag{5.1}$$

where $\hbar$ is the reduced Planck's constant. Λ represents the (effective) de Broglie wavelength of a particle of mass m relative to the parameters σ and ε of the reference LJ potential (σ represents hard-core radius and ε is the potential well depth).

For p-H_2 and o-D_2 molecules one finds $\Lambda \simeq 0.28$ and $\Lambda \simeq 0.2$, respectively, which are larger than the typical values for classical behavior by one order of magnitude. The quantum nature of condensed p-H_2 and o-D_2 has allowed for predicting various interesting effects that are specific to supercooled hydrogen liquids such as superfluidity of p-H_2 [112, 113] and the creation of structural quantum glass in p-H_2–o-D_2 mixtures [124].

In the second section I illustrate the experiment, the results and an initial discussion; in the third section I present the performed simulations and the results about the static correlations; in the fourth I present the analysis of the symmetries of local structures via the so-called local bond order parameters; in the fifth I give a description of the experiments and simulations regarding the mixtures of p-H_2, or o-D_2, with neon; and in the last section I draw the conclusions.

5.2 The experiment

In the experiment in order to reach a supercooled liquid state they employed the experimental technique developed by the Frankfurt group that is described in Ref. [125]. I briefly describe the experiment. The liquid at equilibrium pressure and temperature is injected into vacuum through a 5 µm-diameter glass capillary nozzle. The expanding liquid cools rapidly well below the melting temperature, until it undergoes a first-order phase transition triggered by the homogeneous crystal nucleation. This produces a continuous solid filament several cm long [125]. A pivotal characteristic of this approach is represented by the one-to-one correspondence between the distance along the jet propagation direction z and the time t, that is $t = z/v$, where v is the velocity of the liquid jet. The crystallization kinetics of p-H_2–o-D_2 liquid jets with different o-D_2 content was probed via Raman light scattering by recording as a function of z (and thus as a function of time) the spectra of the fundamental vibrational transition, which allows distinguishing liquid and solid phases of both the p-H_2 and o-D_2 components. The high spatial resolution of this technique basically provides a direct access to the crystallization kinetics on the sub-microsecond time scale [125]. The isotopic species p-H_2, and o-D_2 were produced by continuous catalytic conversion from 99.9999 %, and 99.9 %, purity natural H_2, and D_2, respectively, resulting in 99.8 %, and 97.5 %, purity p-H_2, and o-D_2, respectively, the rest being represented by odd-J molecules. The experimental investigations were performed on the pure p-H_2 and o-D_2 liquid jets, as well as jets of p-H_2–o-D_2 mixtures with o-D_2 mole fractions of 1.0(2) %, 3.2(4) %, 4.6(6) %, 9.1(12) %, 16.7(8) %, 51.6(14) %, 83.9(7) %, 95.7(11) %, and 97.6(6) %. The mixtures were prepared at room temperature by a continuous mixing of the two isotopic gases at the specific ratios set by two mass flow controllers, one for each species, working at a minimum flow rate of $\simeq$ 20 nml min^{-1}(in SI units $\simeq$ 15 µmol s^{-1}). The o-D_2 mole fraction was further checked by the Raman intensity ratios in the gas (if available) and the condensed phases in the vibrational region, confirming the molar flow ratios.

The experimental results are presented in Fig. 5.1 on the following page. In Fig. 5.1a vibrational Raman spectra for three representative p-H_2–o-D_2 mixtures are shown, clearly indicating the transition from liquid (L) to solid (S) phase. The shift to lower wave numbers of the vibrational band, corresponding to the liquid, with increasing distance from the orifice reflects the evaporative cooling of the expanding filament [125]. The average filament temperature at the onset of crystallization grows linearly with the o-D_2 mole fraction, and is shown by the upper x-axis of Fig. 5.2 on page 87. In Fig. 5.1b we plot the time evolution of the p-H_2 and o-D_2 solid fractions extracted from the respective vibrational Raman spectra with the o-D_2 mole fraction ranging from 0 % (pure p-H_2 jet, lower curve) to 100 % (pure o-D_2 jet, upper curve). The most striking feature visible in Fig. 5.1b is the remarkable slow-down of the crystallization kinetics with increasing o-D_2 mole fraction. For example, the presence of only 3 % o-D_2 molecules leads to nearly twice the time required for the complete freezing of the jet when compared to the pure p-H_2 case ($\simeq$ 7.9 µs), as shown in Fig. 5.2. The slowest crystal growth is observed in the case of the nearly equimolar mixture, which fully crystallizes in $\simeq$ 23.3 µs, i.e. three times more slowly than the pure p-H_2 jet. By further increasing the amount of o-D_2 the duration of

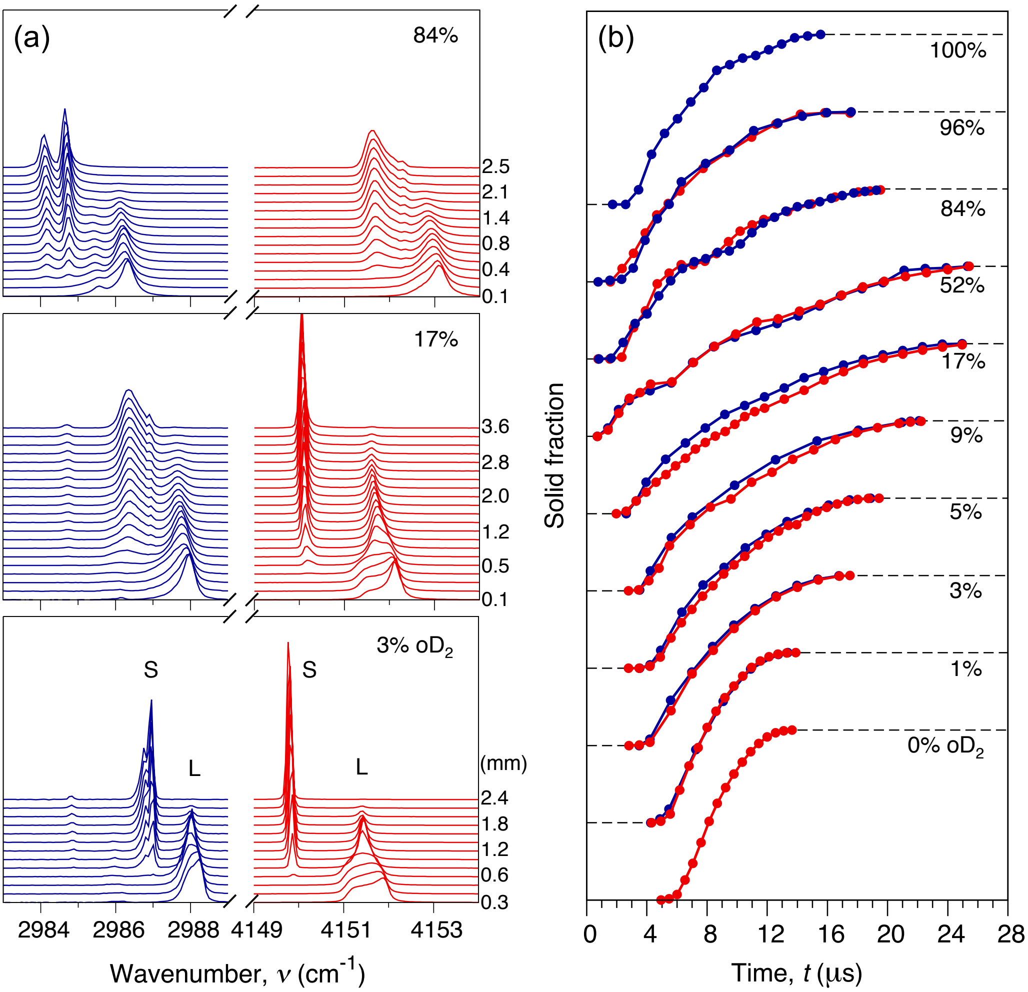

Figure 5.1 (a) Normalized vibrational Raman spectra measured as a function of the distance z from the orifice (right scale) for the o-D$_2$ (blue, left) and p-H$_2$ (red, right) components for three representative mixtures. In the bottom panels L and S indicate the vibrational bands corresponding to the liquid and solid phases, respectively. The double-line shape of the o-D$_2$ bands, which is especially evident in the case of the 84 % o-D$_2$ mixture, is due to the inevitable presence of less than 3 % of $J = 1$ pD$_2$ molecules, with a 50-fold enhancement in the Raman scattering intensity with respect to the $J = 0$ molecules [126]. For the 3 and 17 % o-D$_2$ mixtures this enhancement is much smaller and the $J = 1$ bands are barely visible in the spectra. (b) Time evolution of the solid fractions extracted from the vibrational bands for p-H$_2$ (red points) and o-D$_2$ (blue points), with the time axis defined as $t = z/v$, where v is the jet velocity. The solid fractions range from 0 to 1, as indicated by the dashed lines on the left and on the right of the experimental curves, respectively.

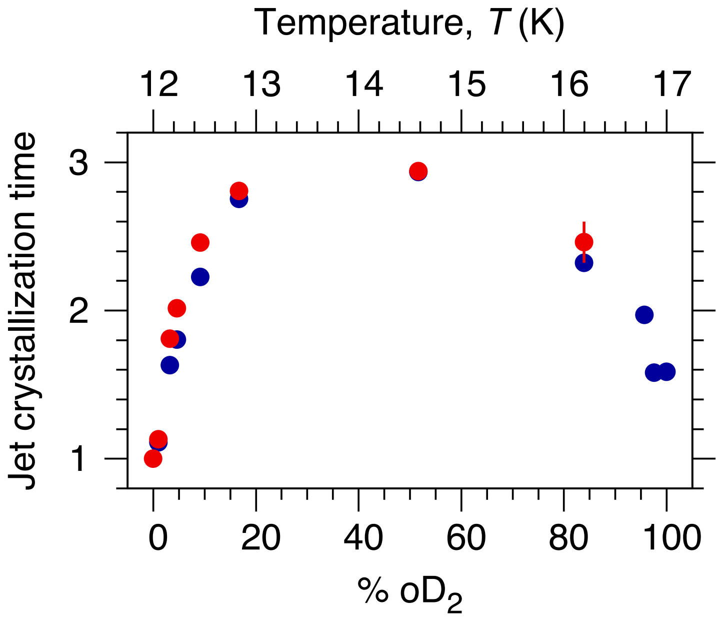

Figure 5.2 Total duration of the jet crystallization process as determined from the p-H_2 (red symbols) and o-D_2 (blue symbols) solid fraction curves of Fig. 1(b). The plotted data indicate relative times with respect to the pure p-H_2 jet crystallization time of 7.9 ± 0.4 μs. The upper x-axis indicates the experimental average filament temperature at the onset of crystallization.

the crystallization process then gradually decreases down to $\simeq 12.6$ μs for the pure o-D_2 jet.

A second important feature exhibited by the experimental data of Fig. 5.2 is the filament's tendency to start crystallizing at earlier times with increasing o-D_2 mole fraction, up to the case of the nearly equimolar mixture. This effect initially appears to be in conflict with the subsequent slower crystal growth. However, we can rationalize this behavior in terms of a higher probability for nucleation triggered by purely statistical clustering of o-D_2 molecules, which reside at a much deeper supercooling than the p-H_2 molecules with respect to their own melting points. The fact that the beginning of crystallization in mixtures with a higher content of o-D_2 again shifts slightly towards later times is the result of the increasingly higher temperature of the filament (see Fig. 5.2).

The observed dependence of the jet-crystallization time on composition as displayed in Fig. 5.2 is surprising, given the isotopic nature of the p-H_2–o-D_2 mixtures. Due to the negligibly small mixing enthalpy [127], which determines the departure of a real mixture from the ideal case, there is no experimental evidence for a phase separation in H_2-D_2 mixtures at equilibrium neither in the liquid nor in the solid [127]; this rules out possible effects related to the presence of strongly partitioning species, as observed in supercooled binary metallic alloys [128]. The possibility of competition between different crystal structures [115, 118] also seems unlikely as both p-H_2 and o-D_2 crystallize into equilibrium hcp crystals [119].

The classical theory of crystal growth [129] is the natural framework to attempt to interpret the experimental crystallization rates found. The crystal growth rate as a function of the temperature T is given by [28]

$$u(T) = k(T)\left[1 - \exp\left(-\frac{\Delta G(T)}{k_B T}\right)\right], \tag{5.2}$$

where $k(T)$ is the crystal deposition rate at the liquid–crystal interface, $\Delta G(T)$ is the difference in Gibbs free energy (per molecule) of the liquid and the crystal, and k_B is Boltzmann's constant. For the case of the nearly ideal p-H_2–o-D_2 mixtures $\Delta G(T)$ can be computed starting from the experimental heat capacity data for the pure p-H_2 and o-D_2 systems [125]: one can find that, for a given temperature, the factor $1 - \exp\left[-\frac{\Delta G(T)}{k_B T}\right]$ varies only slightly with the amount of o-D_2 or p-H_2. Thus, the data gathered suggests that the deposition rate $k(T)$ must be strongly dependent on composition in order to explain the measured crystallization rates. Identifying this dependence is a challenging task, however, since the coefficient $k(T)$, which reflects collective processes in the liquid, is generally expressed on an empirical basis [25, 26, 129]. Our experimental collaborators showed previously [125] that the crystallization of a pure p-H_2 filament can be described by the collision-limited model, in which the deposition rate scales as $k(T) \propto \sqrt{T/m}$. They can estimate the relative duration of the crystallization processes in the pure o-D_2 and p-H_2 jets as the inverse of the ratio between the two deposition rates, i.e. $k_{\text{p-H}_2}(T)/k_{\text{o-D}_2}(T)$. By using the values of m and of T, whose estimates are reported on the top axis of Fig. 5.2, for the two pure systems we obtain a value of $k_{\text{p-H}_2}(T)/k_{\text{o-D}_2}(T)$ of $\simeq 1.2$, which is in qualitative consistent with the the experimental value of $\simeq 1.6$ (Fig. 5.2). However, the kinetic model describe above is not able to describe the observed dependence of the crystal growth rate on composition, as in this case one would rather expect a monotonic increase of the jet crystallization time with o-D_2 mole fraction.

5.2.1 Liquid filament temperature estimation

I report here details carried out by our collaborators on the estimation of the liquid filament temperature of the mixtures at the onset of crystallization. The estimation was obtained starting from the experimental Raman shifts of the p-H_2 vibrational liquid peak. Figure 5.3a shows the time evolution of the Raman shift of the liquid peak for some representative mixtures investigated here. The arrows indicate the onset of crystallization, whose wavenumber shifts to higher values with increasing o-D_2 mole fraction, an effect that is directly related to the increasing density. The wavenumber at the onset of crystallization is plotted in Fig. 5.3b as a function of the o-D_2 mole fraction, clearly showing a linear dependence. Since the (average) filament temperature is directly related to the

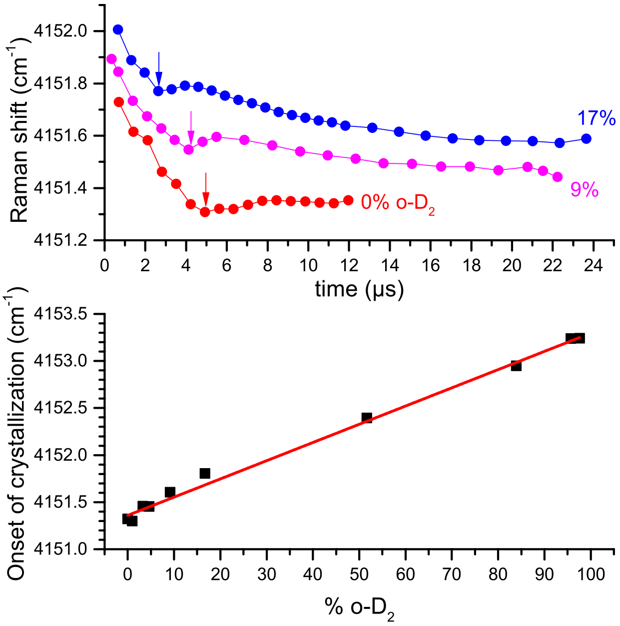

Figure 5.3 (a) Temporal evolution of the Raman shift of the p-H_2 vibrational liquid peak for three representative liquid mixtures. The arrows indicate the onset of crystallization. (b) Vibrational liquid peak wavenumber at the onset of crystallization plotted as a function of the o-D_2 mole fraction. The solid line is a linear fit.

vibrational liquid peak position [125], in a first approximation one can assume a linear dependence of the temperature on the o-D_2 mole fraction or relative fraction x, $T(x) = a+bx$. The filament temperature for the pure p-H_2 case ($x = 0$) was determined experimentally [125], and is $\simeq$ 12 K at the onset of crystallization, and thus $a = 12\,\text{K}$. Since a good agreement was found between the experimental liquid filament temperature and that computed according to a simple evaporative cooling model [125], the latter was used to estimate the average temperature of the pure o-D_2 filament ($x = 1$) to be $\simeq$ 17 K, or $b = 5\,\text{K}$.

5.3 The simulations

Examining the bulk structural features of the supercooled hydrogen liquids offer important insights into the behavior of supercooled liquids [27, 114, 116, 130]. To access static structural properties of the non-equilibrium p-H_2–o-D_2 quantum liquid mixtures, we carried out path integral Monte Carlo (PIMC) simulations (see Chapter 1). We simulated systems of up to 300 molecules in boxes with periodic boundary conditions with 0 %, 3 %, and 10 % of o-D_2 content at $T = 13\,\text{K}$, 50 % o-D_2 at $T = 14.5\,\text{K}$, and 90 %, 97 %, and 100 % o-D_2 at $T = 17\,\mathrm{K}$.

5.3.1 Local bond order parameters

In order to characterize the configurations sampled for the disordered quantum binary mixtures and detect possible differences between the local structures originated around p-H_2 and o-D_2 molecules, we used the local bond order (LBO) analysis introduced by Steinhardt et al. [131], which offers a way to express the (geometric) distribution of direct bonds between a particle and its nearest neighbors. One first introduces the bond orientational order parameter of the l-fold rotational symmetry for each particle i as a $(2l+1)$-dimensional vector $\boldsymbol{q}_l(i)$, whose components are

$$q_{l\,m}(i) = \frac{1}{N_{\mathrm{nb}}(i)} \sum_{j=1}^{N_{\mathrm{nb}}(i)} Y_{l\,m}\big(\boldsymbol{r}_{i\,j}\big), \tag{5.3}$$

where l is an integer label, m is an integer running from $-l$ to l, $Y_{l\,m}(\boldsymbol{r})$ are the spherical harmonics, $\boldsymbol{r}_{i\,j}$ is the vector, the "bond", from particle i to particle j and $N_{\mathrm{nb}}(i)$ is the number of neighbors of the particle i. From the vectors $\boldsymbol{q}_l(i)$ one can construct the rotational invariants that we employed for our LBO structural analysis [131, 132]

$$q_l(i) = \sqrt{\frac{4\pi}{2\,l+1} \sum_{m=-l}^{l} |q_{l\,m}(i)|^2}, \tag{5.4}$$

and

$$w_l(i) = \sum_{\substack{m_1=m_2=m_3=-l\\ m_1+m_2+m_3=0}}^{l} \begin{pmatrix} l & l & l \\ m_1 & m_2 & m_3 \end{pmatrix} q_{l\,m_1}(i)\, q_{l\,m_2}(i)\, q_{l\,m_3}(i), \tag{5.5}$$

where the term in parenthesis in 5.5 is the Wigner 3-j symbol. We used also an improved version of $q_l(i)$, the averaged local bond order parameters [133], which is defined in the same way as $q_l(i)$ in Eq. 5.4, but in place of $q_{l\,m}(i)$ one uses the vector $Q_{l\,m}(i)$, that is constructed averaging $q_{l\,m}(i)$ on the first neighbors and the particle i itself,

$$Q_l(i) = \frac{1}{N_{\mathrm{nb}}(i)+1}\left(q_{l\,m}(i) + \sum_{j=1}^{N_{\mathrm{nb}}(i)} q_{l\,m}(j) \right). \tag{5.6}$$

We select the first neighbors through a Delaunay triangulation. This method is free of any parameter and guarantees a univocal choice of the nearest neighbors molecules.

In order to apply the LBO analysis to a PIMC simulation we had to choose which position vector $\boldsymbol{r}_i$ should be used for the quantum particle i. Since quantum particles are highly delocalized, the positions of the beads in the ring-polymer are subject to very large fluctuations that would deteriorate the LBO analysis. We computed the LBO parameters using as $\boldsymbol{r}_i$ the center of mass of the beads of each ring-polymer; this procedure had been

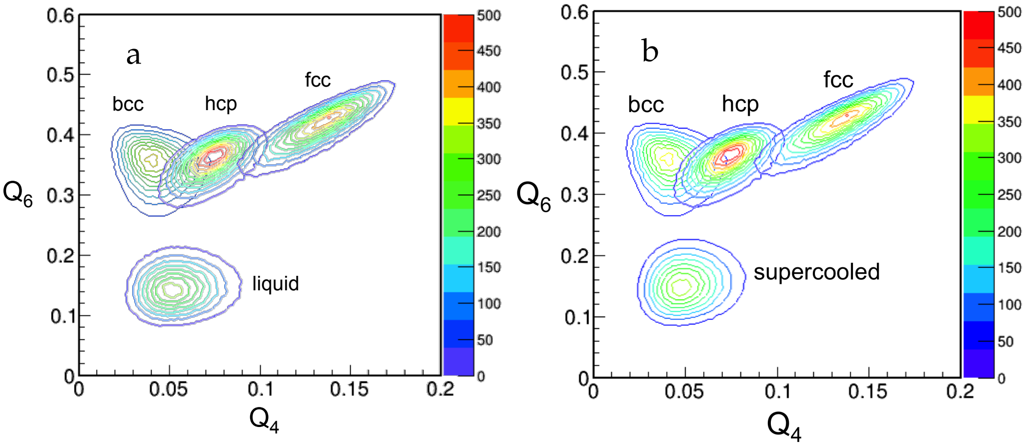

Figure 5.4 Probability distributions $p(Q_4, Q_6)$ of p-H_2 simulated in different phases. (both panels) Three overlapped distributions $p(Q_4, Q_6)$ for the bcc, hcp, and fcc crystal phases at $T = 12\,K$ and $\rho = 0.0240\,Å^{-3}$. (a) $p(Q_4, Q_6)$ for p-H_2 in equilibrium liquid phase at $T = 17\,K$ is shown. (b) $p(Q_4, Q_6)$ for p-H_2 supercooled liquid at $T = 13\,K$ and $\rho = 0.0232\,Å^{-3}$ is also shown for comparison.

used also in a previous application of LBO analysis to an even more quantum system: overpressurized ^{4}He at zero temperature [103].

Depending on the choice of l, all the above bond order parameters are sensitive to different crystal symmetries. As shown by Lechner and Dellago [133], the parameter Q_6 is excellent to distinguish the crystal structures from disordered liquid-like configurations, whereas Q_4 allows distinguishing between different types of crystal structures, e.g. bcc, hcp, fcc. To illustrate these features, for example, in Fig. 5.4a I show the contour plots of the three-dimensional surfaces of the probability distributions $p(Q_4, Q_6)$ on the plane Q_4, Q_6 computed for the bcc, hcp and fcc crystal phases of p-H_2 and the stable liquid phase (above the freezing point). Note that the use of periodic boundary conditions compatible with a specific crystal lattice allows stabilization and also simulation of crystals that do not correspond to the equilibrium solid phase.

5.3.2 Simulations of the metastable liquid phase

We recall that a supercooled liquid is in a metastable phase against freezing at temperature below the melting point. In order to simulate such systems, we adopted a strategy to avoid crystallization [113]. The implemented strategy consisted of two steps. First, we performed a simulation of a system of hydrogen molecules fictitiously interacting via the pair potential of the helium atoms (we did not change the masses of the p-H_2 and o-D_2 molecules). Due to the weaker attractive well of the He–He interaction, the equi-

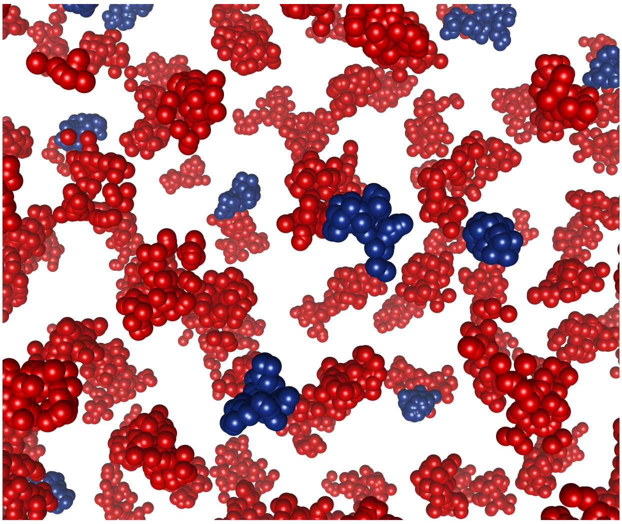

Figure 5.5 A snapshot of a ring-polymer configuration generated by a PIMC simulation of a mixture with 10 % o-D_2 at $T = 13\,\mathrm{K}$. The red and blue clusters of particles are the ring-polymers representing the p-H_2 and o-D_2 molecules, respectively.

librium state of this fictitious system is a disordered phase. Once a disordered state has equilibrated, we turn on the true interaction potential and let the system equilibrate for the second time. We verified that the configurations sampled by the Metropolis algorithm after this second equilibration remained disordered, at least for many thousands of Monte Carlo steps, allowing for a reliable characterization of the system. Moreover, we verified that the results, obtained from statistical independent simulations, were always compatible with each other. This indicates that the physical properties measured in the so-obtained disordered phases are dependent only on the temperature and the density of the mixture, but not on the particular sampled Monte Carlo stochastic trajectory. We point out that the simulated disordered phases can be regarded as representative of the experimental supercooled systems at the initial stages following the free expansion into vacuum, and also during the stage of crystallization, but only in regions of the liquid still without crystals. As such, the stochastic dynamics arising from the Metropolis algorithm in the PIMC method cannot be regarded as a representation of the real crystallization process. For this reason we limited our analysis to the characterization of disordered systems and we did not consider the characterization of crystallization processes which could be present at later stages in our PIMC simulations.

In order to check the validity of the chosen procedure to avoid crystallization, we computed the probability distribution $p(Q_4, Q_6)$ of the parameter pair (Q_4, Q_6) associated to each molecule (p-H_2 or o-D_2) of the configurations sampled during our PIMC simulations of supercooled liquid mixtures; an example is shown in Fig. 5.4b for pure p-H_2 at

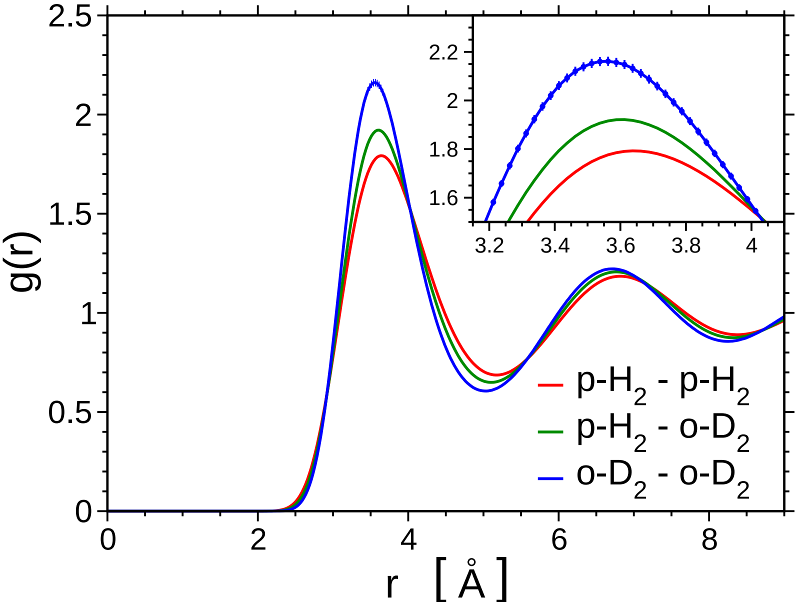

Figure 5.6 Partial radial distribution functions of p-H_2–o-D_2 mixutres with 10 % of o-D_2 at $T = 13\,\text{K}$, $\rho = 0.0235\,\text{Å}^{-3}$.

$T = 13\,\text{K}$ and $\rho = 0.0232\,\text{Å}^{-3}$. We can compare this distribution of the p-H_2 liquid in supercooled phase with the one of p-H_2 in stable liquid phase in Fig. 5.4a and with the crystal-like distribution $p(Q_4, Q_6)$, that are repeated in Fig. 5.4b for an easier comparison. The probability distribution for supercooled p-H_2 results well separated from the distributions computed for any crystal lattice. It indicates the absence of any crystallization sign in the simulated supercooled systems. Similar results were obtained for all quantum binary mixtures considered in the present study.

5.3.3 Quantum delocalization in isotopic mixtures

In Fig. 5.5 on the facing page we show a snapshot of the classical ring-polymers onto which the quantum particles are mapped computed for the 10 % o-D_2 mixture. The degree of spatial extension of the polymers, each corresponding to a p-H_2 (in red) or o-D_2 (in blue) molecule, is representative of their quantum delocalization, i.e., in other words, of the spatial quantum fluctuations of the molecules due to the zero point motion, whose magnitude, in the real system, is reduced by the temperature, respect to the pure zero-point motion at ground-state. The Fig. 5.5 shows that the polymers associated to the o-D_2 molecules are more compact than those associated to the p-H_2 molecules.

We can explain this difference if we recall the quantum–classical mapping coming out from the path integral formalism, exploited in the PIMC method, described in Chapter 1. The spatial correlations among adjacent beads belonging to the same ring-polymer mainly origin from the kinetic part of the imaginary-time propagator, defined in Eq. 1.32 (page 19), that we re-write here,

$$G^0(\mathbf{R},\mathbf{R}';\delta\tau) = \frac{1}{(4\pi\lambda\,\delta\tau)^{dN/2}}\exp\left(-\frac{(\mathbf{R}-\mathbf{R}')^2}{4\lambda\,\delta\tau}\right), \tag{5.7}$$

where $\delta\tau = \beta/M = 1/(TM)$ (we remember that M is the number of imaginary-time steps) and $\lambda = 1/(2\,m)$, that corresponds to the imaginary-time propagator of a system of N free particles. Thus these correlations, a sort of harmonic springs connecting adjacent beads, depend, via λ, on the mass m of the quantum particle. For a given temperature, therefore, the masses contribute in setting the springs strength, thus determining the average spatial extension of the ring-polymers: the higher is the mass, the tighter are the springs and the more compact are the ring-polymers.

This difference in magnitude of the quantum delocalization affects the local structural properties, as shown in Fig. 5.6 on the previous page, where I plot the three partial radial pair distribution functions for the average static density correlations. We see that the o-D_2–o-D_2 correlation exhibits a higher first peak, which is also shifted towards smaller distances than for the p-H_2–p-H_2 and p-H_2–o-D_2 correlations, indicating significant differences in the average distance between neighboring particles of the two isotopic species. Similar results are found for all the simulated mixtures as we can see in Fig. 5.7 on the facing page. As consequence, the statistical weight contained in the expectation value of a physical observable (see Eq. 1.6 on page 12) turns out to depend on the masses of the particles and this affects the values of properties like, for example, the radial distribution function.

This is different from a classical system where the kinetic term in the Hamiltonian does not modify the probability of the spatial configurations[134]. To be specific, consider a classical binary mixture of N_A particles of type A and N_B particles of type B, which have different masses, m_A and m_B, but all interacting via an identical pair potential $v(r)$, i.e. $v_\mathrm{AA}(r) = v_\mathrm{AB}(r) = v_\mathrm{BB}(r) = v(r)$. In this classical model the partial radial distribution function relative, for example, to the AA-pairs in the thermodynamic limit reads

$$g_\mathrm{AA}(r) = \frac{V^2}{Z}\int \mathrm{d}\boldsymbol{r}_{\mathrm{A},3}\cdots\mathrm{d}\boldsymbol{r}_{\mathrm{A},N_\mathrm{A}}\,\mathrm{d}\boldsymbol{r}_{\mathrm{B},1}\cdots\mathrm{d}\boldsymbol{r}_{\mathrm{B},N_\mathrm{B}}\,e^{-\beta U\left(\boldsymbol{r}_{\mathrm{A},1},\dots,\boldsymbol{r}_{\mathrm{A},N_\mathrm{A}},\boldsymbol{r}_{\mathrm{B},1},\dots,\boldsymbol{r}_{\mathrm{B},N_\mathrm{B}}\right)}, \tag{5.8}$$

where Z is the configurational partition function

$$Z = \int \mathrm{d}\boldsymbol{r}_{\mathrm{A},1}\cdots\mathrm{d}\boldsymbol{r}_{\mathrm{A},N_\mathrm{A}}\,\mathrm{d}\boldsymbol{r}_{\mathrm{B},1}\cdots\mathrm{d}\boldsymbol{r}_{\mathrm{B},N_\mathrm{B}}\,e^{-\beta U\left(\boldsymbol{r}_{\mathrm{A},1},\dots,\boldsymbol{r}_{\mathrm{A},N_\mathrm{A}},\boldsymbol{r}_{\mathrm{B},1},\dots,\boldsymbol{r}_{\mathrm{B},N_\mathrm{B}}\right)}, \tag{5.9}$$

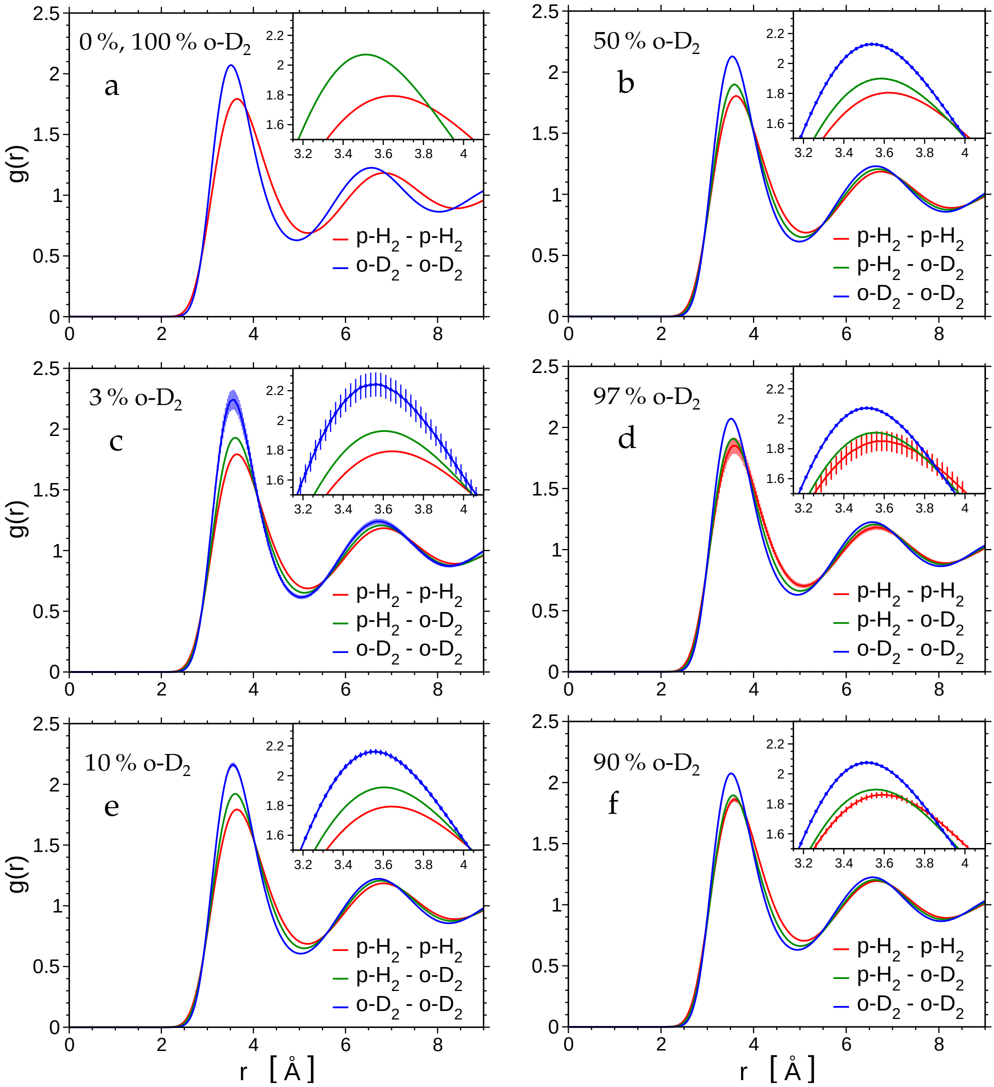

Figure 5.7 Partial radial distribution functions $g(r)$ for the pure p-H$_2$ and o-D$_2$ systems and for different mixtures: (a) the pure p-H$_2$ and o-D$_2$ systems computed at $T = 13\,\text{K}$, $\rho = 0.0232\,\text{Å}^{-3}$ and $T = 17\,\text{K}$, $\rho = 0.0263\,\text{Å}^{-3}$, respectively; (b) 50 % o-D$_2$ mixture at $T = 14.5\,\text{K}$, $\rho = 0.024\,75\,\text{Å}^{-3}$; (c) 3 % o-D$_2$ mixture at $T = 13\,\text{K}$, $\rho = 0.0233\,\text{Å}^{-3}$; (d) 97 % o-D$_2$ mixture at $T = 17\,\text{K}$, $\rho = 0.0262\,\text{Å}^{-3}$; (e) 10 % o-D$_2$ mixture at $T = 13\,\text{K}$, $\rho = 0.0235\,\text{Å}^{-3}$; (f) 90 % o-D$_2$ mixture at $T = 17\,\text{K}$, $\rho = 0.0260\,\text{Å}^{-3}$.

V the volume and U the total potential energy

$$U\left(\boldsymbol{r}_{\mathrm{A},1}, \dots, \boldsymbol{r}_{\mathrm{A},N_\mathrm{A}}, \boldsymbol{r}_{\mathrm{B},1}, \dots, \boldsymbol{r}_{\mathrm{B},N_\mathrm{B}}\right) = \frac{1}{2} \sum_{i,j=1\,(i\neq j)}^{N_\mathrm{A}} v\left(\left|\boldsymbol{r}_{\mathrm{A},i} - \boldsymbol{r}_{\mathrm{A},j}\right|\right) + \\ + \frac{1}{2} \sum_{i=1}^{N_\mathrm{A}} \sum_{j=1}^{N_\mathrm{B}} v\left(\left|\boldsymbol{r}_{\mathrm{A},i} - \boldsymbol{r}_{\mathrm{B},j}\right|\right) + \frac{1}{2} \sum_{i,j=1\,(i\neq j)}^{N_\mathrm{B}} v\left(\left|\boldsymbol{r}_{\mathrm{B},i} - \boldsymbol{r}_{\mathrm{B},j}\right|\right). \tag{5.10}$$

In Eq. 5.8 all degrees of freedom, but those of 2 particles of type A, $\boldsymbol{r}_{A,1}$ and $\boldsymbol{r}_{\mathrm{A},2}$, are integrated over In the same way, $g_{\mathrm{BB}}(r)$ is obtained by integrating over all the coordinates, but those of two particles of type B. $g_{\mathrm{AB}}(r)$ is obtained in an analogous way, leaving out of the integration two particles of different type. It is readily evident that, due to the fact that the configurational probability in Eq. 5.8 does not depend on the masses of the particles, the partial radial distribution functions are all identical, $g_{\mathrm{AA}}(r) = g_{\mathrm{AB}}(r) = g_{\mathrm{BB}}(r)$, independently on the relative mole fractions of the components. On the contrary, the path integral formalism immediately shows that in a similar quantum binary mixture, where the components have different masses but interact via an identical pair potential, this is no more true; the effect is purely quantum and it origins in the different degree of quantum delocalization of the two types of particles.

In Fig. 5.7 the partial radial distribution functions for various p-H_2–o-D_2 supercooled liquid mixtures are displayed; they correspond to 0 %, 100 %, 3 %, 10 %, 50 %, 90 %, and 97 % o-D_2 mole fractions. Note that the six panels in Fig. 5.7 refer to different densities and temperatures as indicated in the caption. These results indicate that, due to a lower degree of quantum delocalization, the *effective size* of an o-D_2 molecule is inferior than the *effective size* of a p-H_2 molecule: on average the intermolecular distance in a pair of neighbor o-D_2 molecules is smaller than the one in a pair of neighbor p-H_2 molecules. The position of the first peak in $g_{\mathrm{AB}}(r)$ is found at intermediate values with respect to the previous ones. Contrarily to the hypothetical classical case, also the intensity and the width of the first peaks in the partial radial distribution functions are remarkably different.

The PIMC simulations show that as a result of the mass-induced quantum delocalization the p-H_2 and o-D_2 molecules exhibit different "effective sizes", thus illuminating the origin of the measured growth rates. Classical molecular dynamics simulations of binary particle systems with a given size ratio [115, 118, 135] have indeed showed a correlation between composition and crystallization kinetics that is strikingly similar to that observed in the experiments performed in our collaborative work. In particular, for binary hard-sphere mixtures it was shown that the crystal growth becomes extremely slow for mole fractions of one of the two components in the range 20 %–50 % [135]. A similar result was found in the simulation of a model binary LJ system [115], indicating in particular the failure of the mixture to crystallize, i.e. the formation of an amorphous state, for mole fractions of the smaller particles of 20 %–50 %, whereas otherwise rapid ordering was observed. The similarity between those numerical results and the experimental data, which exhibit a maximum in the jet crystallization time for o-D_2 mole fractions in the range 20 %–50 % (Fig. 5.2 on page 87), is interesting, hinting at a common mechanism responsible for the crystallization slow-down. However, a microscopic understanding of how composition and particle size ratio frustrate the crystal growth in binary mixtures is still lacking [115, 118, 135]. Much of knowledge about crystallization and vitrification

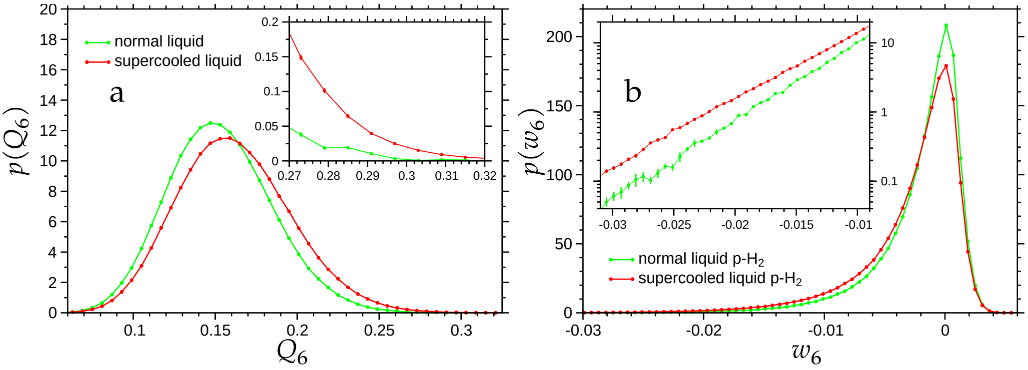

Figure 5.8 (a) Probability distributions $p(Q_6)$ for p-H_2 in equilibrium liquid phase at $T = 17\,K$ and $\rho = 0.0240\,Å^{-3}$ (green line), and for p-H_2 supercooled liquid at $T = 13\,K$ and $\rho = 0.0232\,Å^{-3}$ (red line); (inset) a zoomed view of the tails at high Q_6. (b) Probability distributions $p(w_6)$ for the same systems shown in the figure **a**. (inset) a zoomed view in logarithm scale of the tails at low w_6.

comes from simulations of hard spheres [135], Lennard-Jones particles or metals [115]. These model systems often employ simplified interaction potentials, so that their validity is limited. Real atomic/molecular systems are often too complex to be simulated with dynamical processes and only static properties of liquid and solid states are obtainable.

5.4 Local bond order analysis

A number of simulations studies [114, 116, 117, 130] have suggested that crystallization might be hindered by the emergence of locally preferred structures in the bulk supercooled liquid that eventually are incompatible with long-range crystalline order [136]. One important example is the icosahedron with its five-fold symmetry [137], which has been recently found to be a fundamental geometrical characteristic in the structure of bulk metallic glasses [138]. To explore this point we performed a microscopic structural analysis based on the local bond order parameters method [27, 117, 130] of our simulated p-H_2–o-D_2 mixtures. We focus here on the parameter w_6, which is most sensitive to the icosahedral-like order, but this analysis does not rule out the presence of local order with different symmetries in the metastable liquid.

In Fig. 5.8a we show the distributions of the single parameter Q_6 for para-hydrogen in the two liquid phases, the normal and the supercooled; they are also present in the distributions $p(Q_4, Q_6)$ shown in Fig. 5.4. We observe a distinct difference between the two distributions: the one of the supercooled liquid is characterized by a greater average of Q_6 and a longer tail toward high Q_6 respect to the distribution of the normal liquid. Since high values of Q_6 indicate greater tendency to crystallize, this discrepancy shows that the

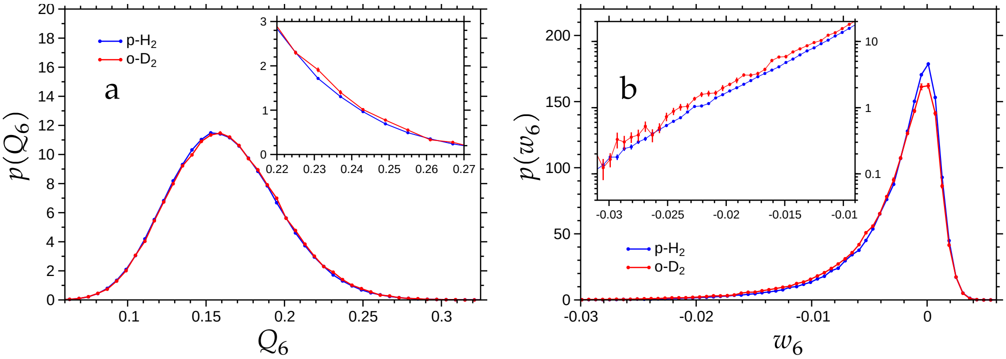

Figure 5.9 (a) Probability distributions $p(Q_6)$ for the p-H$_2$ (red) and o-D$_2$ (blue) molecules in a supercooled p-H$_2$–o-D$_2$ liquid mixture with 10 % o-D$_2$ mole fraction at $T = 13$ K and $\rho = 0.0235$ Å^{-3}; (inset) a zoomed view of the tails at high Q_6. (b) Probability distributions $p(w_6)$ for the same mixture shown in figure **a**. (inset) An enlarged view of the tail on a logarithmic scale to emphasize the difference between the two isotopic species at low values of w_6.

supercooled liquid is "closer" to the crystallization compared to the normal liquid, as we would expect.

Another important local bond order parameter is w_6: it can used to characterize the tendency to form icosahedral-like structures in the system (see e.g. Ref. [132]). A similar comparison to that just described about the probability distributions $p(Q_6)$, but concerning the probability distribution $p(w_6)$ is shown in Fig. 5.8b. The distribution $p(w_6)$ relating to supercooled liquid has a lower peak and a tail at low w_6 longer compared to the case of normal liquid. This behavior reveals a greater tendency to form local structures of icosahedral symmetry. These comparisons can be observed also in Fig. 5.10 on the facing page where we show the plots in color map of the three-dimensional surfaces of the probability distributions $p(w_6, Q_6)$ on the plane w_6, Q_6, for normal liquid p-H$_2$ (Fig. 5.10a) and for the supercooled liquid 10 % o-D$_2$ mixture (Fig. 5.10b).

We show in Fig. 5.9a the plots of the probability distribution $p(Q_6)$ computed separately for the p-H$_2$ and o-D$_2$ molecules for the 10 % o-D$_2$ mixture. We can see that the descending part of $p(Q_6)$ at high values of Q_6 of the curve relating to the molecules of o-D$_2$ is just slightly higher than the one relative to the p-H$_2$ molecules, suggesting that a very small tendency to crystallize is present around the o-D$_2$ molecules compared to the molecules of p-H$_2$. In Fig. 5.9b we plot the probability distribution $p(w_6)$ computed separately for the p-H$_2$ and o-D$_2$ molecules for the 10 % o-D$_2$ mixture. We see a slightly larger tendency for o-D$_2$ to populate more negative values of w_6 than for p-H$_2$, denoting an enhanced probability for local non-crystalline order around an o-D$_2$ molecule. Similar results are found for all other simulated mixtures.

As for the case of classical systems [130], we find that this tendency to non-crystalline order increases with the degree of supercooling. If a correlation between local order and

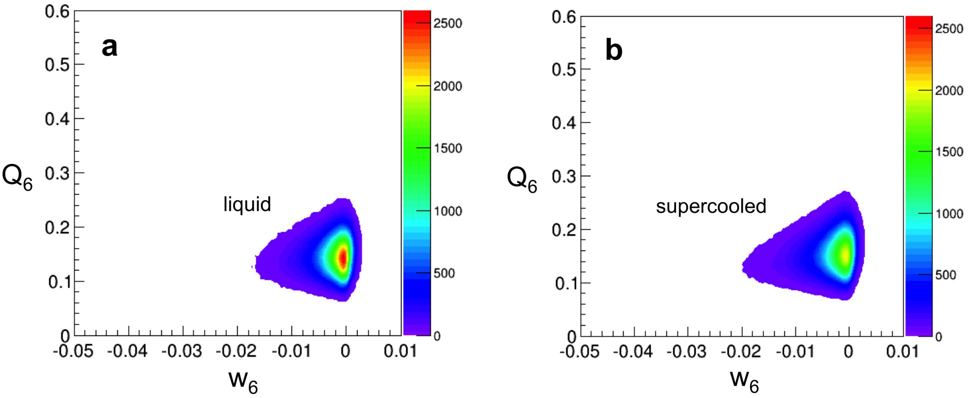

Figure 5.10 Probability distributions $p(w_6, Q_6)$ computed (a) for equilibrium pure p-H_2 liquid at $T = 17\,\mathrm{K}$ and $\rho = 0.0232\,\text{Å}^{-3}$ and (b) for a supercooled p-H_2–o-D_2 liquid mixture with 10 % o-D_2 mole fraction at $T = 13\,\mathrm{K}$ and $\rho = 0.0235\,\text{Å}^{-3}$. The fact that $p(w_6, Q_6)$ in (b) broadens toward lower negative values of w_6 evidences that the amount of icosahedral-like local order increases with the degree of supercooling.

crystal deposition rate could be established, then a difference in the packing efficiency for the two isotopic species as revealed by our structural analysis might provide a physical basis to explain the observed dependence of the crystal growth rate on the o-D_2 mole fraction; the rearrangement of local non-crystalline structures in the supercooled melt at the liquid/crystal interface would tend to lower the particle diffusivity, thus slowing down the crystal growth [29].

5.5 Crystallization dynamics in mixtures of p-H_2 and o-D_2 with Ne

The experimental groups of Frankfurt and Madrid have recently carried out further experiments in which the kinetics of crystallization of p-H_2–Ne and o-D_2–Ne mixtures has been investigated.

Neon is a noble gas with a mass 10 times that of molecular hydrogen and also its interaction potential is symmetric and very close to that of hydrogen molecule, with the same well depth ε and just 1.06 times smaller radius σ of the LJ potential. In Fig. 5.11 on the next page are shown interaction potentials between a pair of Ne atoms, and between a Ne atom and p-H_2 (or o-D_2) molecule, adopted in our PIMC simulations.

From private communications, we know that the experiments have shown the slow-down of crystallization with increasing content of Ne in p-H_2 or o-D_2 as well, but this effect is greatly enhanced with respect to the isotopic mixtures. In addition, they have found a greater slow-down in the o-D_2–Ne mixtures respect to the p-H_2–Ne mixtures.

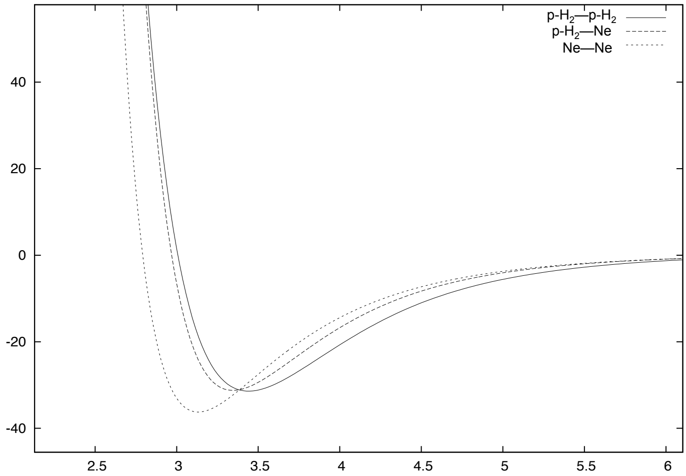

Figure 5.11 Potentials of interaction p-H_2–p-H_2, p-H_2–Ne, and Ne–Ne.

5.5.1 Simulations of p-H_2–Ne and o-D_2–Ne mixtures

Also in this case we have contributed PIMC simulations to characterize static structural properties of the metastable p-H_2–Ne and o-D_2–Ne liquid mixtures. We have simulated systems of 300 molecules in boxes with periodic boundary conditions with 3 % of Ne in the p-H_2–Ne mixture at $T = 13\,\mathrm{K}$ and in the o-D_2–Ne mixture at $T = 17\,\mathrm{K}$. The chosen temperatures are suggested by the experimental measures.

In Fig. 5.12 on the facing page I show our result on the three partial radial pair distribution functions for both mixtures. We see that the Ne–Ne correlation in both cases exhibits a first peak, which is very high, much more than the first peaks relative to the other partial radial distributions in the same system, but also higher than the first peaks of the partial correlations in p-H_2–o-D_2 mixtures. We note also that the Ne–Ne peak is shifted towards smaller distances, indicating significant differences in the average distance between neighboring particles of the two species.

We have performed also the same statistical analysis on the local bond order parameters carried out for the p-H_2–o-D_2 mixtures. We have focused the analysis on the distribution of the w_6 parameter, that is computed for each of the p-H_2 and o-D_2 molecules, and the Ne atoms. As explained before, w_6 is useful to monitor the relative tendency to icosahedral order around the molecules or atoms.

I report the results of the analysis by showing in Fig. 5.13 the probability distribution $p(w_6)$ computed for the p-H_2 and o-D_2 molecules, and for the Ne atoms. We can see, in particular looking at the tails of the distributions towards more negative values of w_6, that around the Ne atoms (light and dark green lines) there is a much greater tendency to

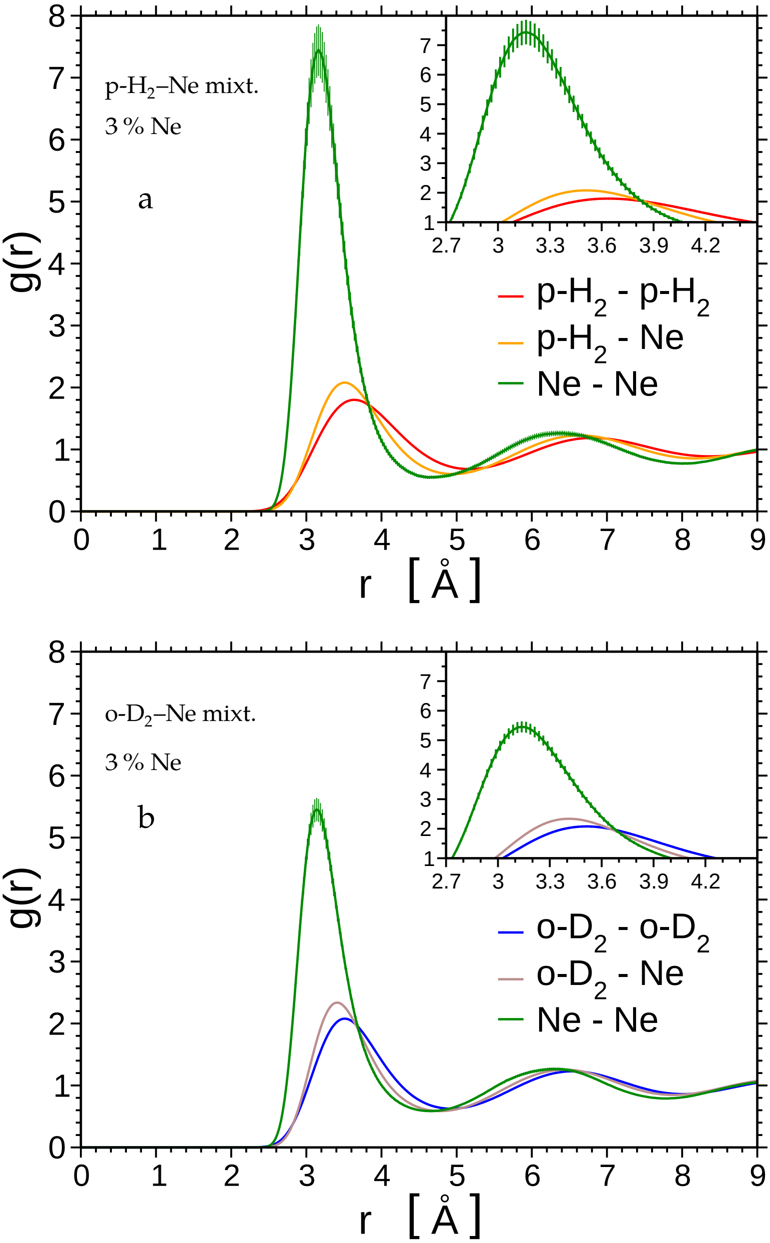

Figure 5.12 Partial radial distribution functions $g(r)$ for mixtures with 3 % of Ne: (a) p-H_2–Ne mixture (b) o-D_2–Ne mixture

the icosahedral order than around the hydrogen isotopic molecules (red and blue lines), especially in comparison with that found in the hydrogen mixtures. As mentioned above,

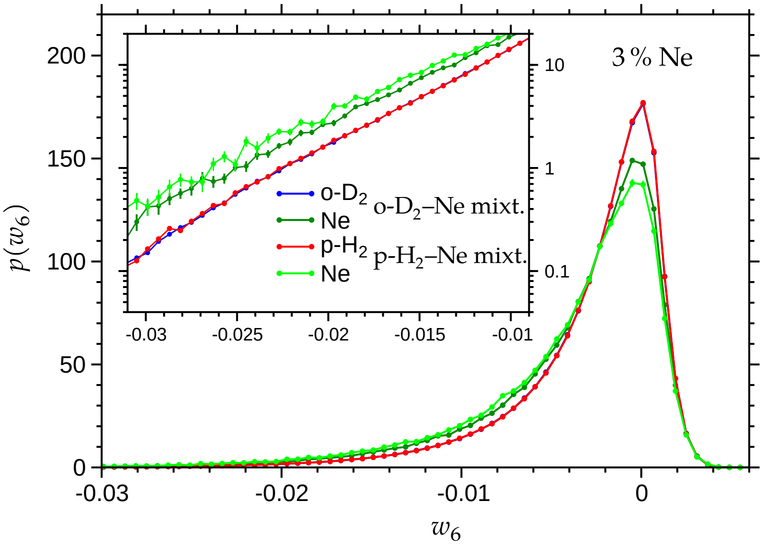

Figure 5.13 Probability distributions $p(w_6)$ for the mixture (inset) An enlarged view of the tail on a logarithmic scale to emphasize the differences at low values of w_6.

from private communications we know that our experimental collaborators have found a greater slow-down in the mixtures with Ne, therefore to find a greater tendency to the icosahedral order gives more importance to our results. We note also that the icosahedral order around the Ne atoms is greater in the p-H_2–Ne mixture (light green line) than in o-D_2–Ne mixtures (dark green line).

5.6 Conclusions

The experimental results show that composition and particle size ratio play a central role in the kinetics of crystallization of simple nearly-ideal molecular binary mixtures. These results add new knowledge for understanding the principles that govern the stability of supercooled liquids against crystallization.

The work exposed in this Chapter provides a first evidence for slow-down of crystallization that is purely of quantum origin. Indeed, we showed that the static density correlations in the supercooled liquid p-H_2–o-D_2 mixtures evidence a difference in the mass-induced quantum delocalization of the two hydrogen isotopic molecules. This suggests that it is only this difference that introduces frustration of crystallization. We found also that around the o-D_2 molecules there is a greater tendency to the icosahedral order respect with the p-H_2 molecules, indicating a possible factor that contributes to frustration of crystallization.

The results on the mixtures with Ne atoms, that are more localized than the hydrogen isotopic molecules, confirm the relevance of effects of the different quantum delocalization of the mixture components.

CHAPTER 6

^{4}He Nanodroplets doped with Ar$^+$ ion

6.1 Introduction

In this chapter it is presented a PIMC study of structural properties of helium-4 nanodroplets doped with a positive argon ion, Ar$^+$ [139]. This work was motivated by a recent experimental study of Bartl et al. [31], which investigated ^{4}He nanodroplets doped with ions of noble gases, Ar$^+$, Kr$^+$, and Xe$^+$, and observed a rich spectrum of anomalies in the abundance distribution indicating the formation of different types of structures. In particular, for the Ar$^+$@^{4}He$_n$ complexes they found three *magic numbers*, 12, 32 and 44, that were interpreted as evidence of three distinct solvation shells containing 12, 20 and 12 helium atoms, from the first to the third shell, respectively. Their interpretation was also supported by the previous PIMC study of Galli et al. [32] regarding Na$^+$ ion doped ^{4}He nanodroplets. The authors found a solid structure around the ion consisting of 3 concentric solvation shells of ^{4}He atoms. For $n > 30$, the ^{4}He atoms were found to be placed at the vertices of platonic solids.[1] The first inner shell is an icosahedron (12 atoms); the second one is a dodecahedron with 20 atoms placed on the faces of the icosahedron of the first shell; the third shell is again an icosahedron composed of 12 atoms placed on the faces of the dodecahedron of the second shell.

The main goal of this project has been to perform, via PIMC simulations, an accurate study of the structures and energetics of ^{4}He nanodroplets doped with an Ar$^+$ ion, for different numbers of ^{4}He atoms, and eventually confirm, the interpretation given in the experimental work.

The chapter is organized as follows: in Sec 6.2 we give a brief background on the topic; in Sec. 6.3 we provide the Hamiltonian of the system and some details of the PIMC computation; in Sec. 6.4 the results of the work and their discussion are presented; in the last Section we provide the conclusions and draw future perspectives about the project.

---

[1] Platonic solids are the convex regular polyhedra with congruent faces of regular polygons and the same number of faces meeting at each vertex

6.2 Background

Thanks to their unique properties nanodroplets of helium have been extensively studied in the last two decades and itself constitutes a very active field of research. Helium droplets can act as a matrix where neutral or charged molecules and atoms and chemical reactions [140, 141] can be investigated by means of high resolution spectroscopy; together they are techniques called Helium Nanodroplet Isolation (HENDI) spectroscopy (for reviews see e.g. Refs [142–149]). Such matrices have also very recently started to be used for the synthesis of clusters, nanoparticles and nanowires [150–152]. Moreover, they provide unique environments to investigate superfluidity in finite systems via rotation of embedded dopants [142, 144–146, 148].

The use of charged impurities in ^{4}He has a long history started with their adoption in bulk superfluid ^{4}He as one of the first microscopic probes that were employed to study the phenomena of superfluidity in liquid ^{4}He [153–156]. A *negatively charged* impurity, such as an electron or a He anion, He$^-$, forms a nanoscopic bubble in the liquid due to the Pauli repulsion between electrons of the neutral ^{4}He atoms and the impurity. On the contrary, a *positive* ion generates in the solvent a region of increased density due to the strong electric field originating from the ion itself, i.e. the effect called *electrostriction*. The local density is estimated to be so large that ^{4}He should solidify around the ion. This is the phenomenological *snowball* model developed by Atkins [157] and widely exploited in the interpretation of the earlier experiments of positive charge carriers in bulk superfluid ^{4}He. [155, 156].

A similar snowball is expected to be present also if the ion is captured inside a droplet of ^{4}He; actually, many experiments performed with various positive ions have been interpreted in terms of the formation of a snowball [142, 148, 158].

One of the main properties analysed to investigate the structure and the size of the snowball surrounding the core ion is the number of the ^{4}He atoms in the solvation shells, n. Experimentally, one of the approaches consists in deducing n from measures of partial pressures of the $X^+@^4He_n$ complexes in the gas phase at thermal equilibrium. These type of experiments provide also information about the dissociation energies D_n, defined as $D_n = E_{n-1} - E_n$, and rapid drops in D_n would indicate the closure of solvation shells. Such type of measurements are limited to very small complexes [159]. Another method to determine the number of helium atoms in the solvation shells is to look for anomalies in the abundance distributions, I_n, of $X^+@^4He_n$ complexes measured under non-equilibrium conditions and often the anomalies correlates with anomalies in D_n. In fact in these experiments the observed complexes are products of dissociations caused by ionization of larger precursor ions. The dissociation is a statistical process and the final statistical distribution of the products versus their size is related to the dissociation energies D_n especially for small droplets. In this way the anomalies in D_n, signals of closures of the solvation shells, are reflected in the measured abundance distribution I_n.

As anticipated in the introduction to this Chapter, in a recent experimental study, Bartl et al. [31], investigated ^{4}He nanodroplets doped with ions of the noble gases, Ar$^+$, Kr$^+$ and Xe$^+$, and observed a rich spectrum of anomalies in I_n, indicating the formation of different types of structures. In particular, the Ar$^+$@^{4}He$_n$ complexes showed evidence for three distinct solvation shells containing 12, 20 and 12 helium atoms, going from the first to the third shell. Other previous experimental works found evidence of a first shell with 12 atoms surrounding the Ar$^+$ ion. [160–164].

On the theoretical point of view, quantum Monte Carlo (QMC) methods have been extensively used in the past to obtain microscopic studies of positive ions in bulk and in nanodroplets of ^{4}He [32, 148, 165–169]. The first zero-temperature QMC studies of ^{4}He nanodroplets with impurities were carried out with variational Monte Carlo (VMC) methods, using a family of accurate trial wave functions, called Shadow Wave Functions (SWF) [170–172]. These studies confirmed the formation of a snowball around the ion, as predicted by the Atkins' model, and found that the solid structure is characterized by formation of well-defined shells of ^{4}He atoms. And the size of the snowball, the number of atoms in the shells and the kind of local order were found to depend on the specific ion. An earlier PIMC study was performed on ^{4}He$_{100}$@Na$^+$ and a triple shell structure was found; the first shell was found to be solid-like while the third one was liquid-like. This was different from the SWF result and in disagreement with a later PIMC work performed by Galli et al. [32]. Gianturco and collaborators [165, 166, 168, 169] carried out extensive studies of small ^{4}He clusters doped with alkali mono-atomic and bi-atomic ions (Li$^+$, Na$^+$, K$^+$) at $T = 0$ K. They employed the VMC method and ab initio potential energy curves to optimize a trial wave function; in a second step, they applied the diffusion Monte Carlo (DMC) method in order to obtain the energy and the geometric distribution of the cluster. They found a rigid solvation shell of icosahedral symmetry for Na$^+$@^{4}He$_{12}$ and a first shell of 10 helium atoms for Li$^+$.

The same three magic numbers found in Ref. [31] have been observed in a Path Integral Monte Carlo (PIMC) study of Na$^+$@^{4}He$_n$ complexes with a number of atoms greater than 30 [32]. Such numbers correspond to a highly ordered snowball with three ordered shells compatible with an icosahedron, in the first and third shells and a dodecahedron in the second shell. Furthermore, they found that the type of solid order around the ion depends mainly on the position of the minimum of the ion–^{4}He potential and that the degree of localization of the ^{4}He atoms varies with the depth of this minimum.

6.3 Methodology

6.3.1 The Model

The Hamiltonian operator of the system has the form

$$\hat{H} = \frac{1}{2\,m_4}\sum_{i=1}^{n}\hat{p}_i^2 + \frac{\hat{p}_{\mathrm{Ar}}^2}{2\,m_{\mathrm{Ar}}} + \sum_{i=1}^{n} v_{\mathrm{Ar}}(|\hat{\boldsymbol{r}}_{\mathrm{Ar}} - \hat{\boldsymbol{r}}_i|) + \sum_{1\leq i<j\leq n} v_{\mathrm{He}}\left(\left|\hat{\boldsymbol{r}}_i - \hat{\boldsymbol{r}}_j\right|\right) \tag{6.1}$$

where n is the number of ^{4}He atoms in the nanodroplet, m_4 is the mass of a ^{4}He atom, m_{Ar} is the mass of the Ar$^+$ ion, v_{He} and v_{Ar} are the He–He and Ar$^+$–He interaction potentials, $\{\hat{\boldsymbol{r}}_i, \hat{\boldsymbol{p}}_i\}_{i=1}^n$, $\hat{\boldsymbol{p}}_{\mathrm{Ar}}$ and $\hat{\boldsymbol{r}}_{\mathrm{Ar}}$ are, respectively, the position and momentum operators of the ^{4}He atoms and Ar$^+$ ion.

As pair interaction potentials we have employed for the He–He interaction the well tested HFDHE2 potential, determined by Aziz et al. [104], and for the Ar$^+$–He interaction the ground state $X^2\Sigma_{1/2}$ adiabatic *potential curve* of the MAL1 interaction potential, that is an accurate semi-empirical interaction potential obtained by Carrington et al. [173], whose experimental parameters has been provided by microwave spectroscopy measurements. In Fig. 6.1 on the next page, we plot the two adopted potentials, v_{He}, v_{Ar} and, by comparison, also the Na$^+$–He interaction potential, v_{Na}, [174] used in Ref. [32]. One can notice that the two ion–He potentials have wells with not very different depth and minimum position and both wells are more than 40 times deep and placed at shorter distances than the well of the He–He potential.

I would remark that the spatial configurations of the ^{4}He atoms in the snowball are a result of the competition of the ion–He and He–He interactions against the thermal and zero point fluctuations of the ^{4}He atoms and the ion. In general, a hypothetical spatial structure of the first shell with a given number of ^{4}He atoms, around an attractive impurity, corresponds to the minimum of the potential energy, if the distances between first-neighbor ^{4}He atoms and the ion–^{4}He distances correspond to the minimum of the respective interaction potentials. Obviously, this ideal situation occurs in particular cases, since the condition just described, i.e. the simultaneous minimization of the two interaction potentials, is not always possible. However, configurations of the atoms configurationally near to the "ideal" structure have a lower overall potential energy, i.e. they are more favorable; clearly, provided that the interaction-potential well between the ion and the atoms in the first shell is not too narrow, because this would increase the zero-point energy, creating a competition with the potential energy in determining the most stable state. If we apply the condition to a shell of the shape of a regular icosahedron, placing one ^{4}He atom at each of the 12 vertices with the distance between two adjacent ^{4}He atoms equal to the position of the minimum of v_{He}, that is $r_{\mathrm{He}} \simeq 2.97$ Å, then the vertices will be at the "ideal" distance $r_{\mathrm{id}} \simeq 0.95\ r_{\mathrm{He}} \simeq 2.82$ Å from the center of the icosahedron, indicated in Fig. 6.1 by the green arrow and dotted line. From Fig. 6.1a, we note that the

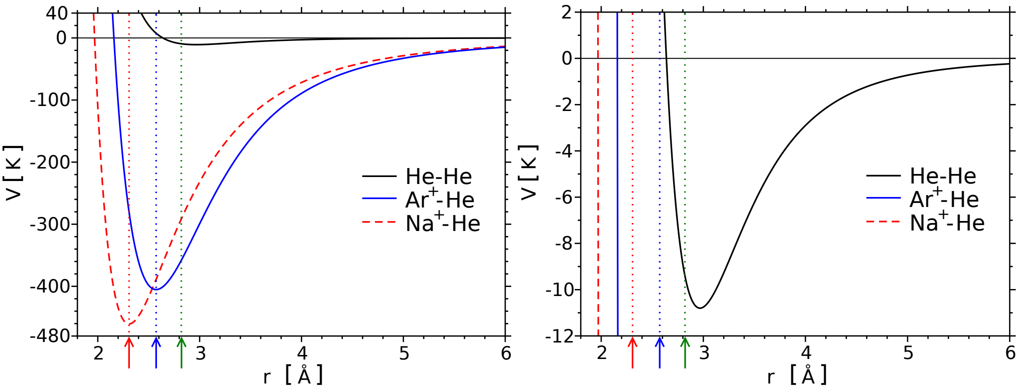

Figure 6.1 He-He, Ar⁺–He and Na⁺–He interaction potentials (v_4, v_{Ar} and v_{Na}) shown in two different scales. The dotted vertical lines and the arrows show the positions of the minimum of the ion–He potentials, r_{Ar} (blue), r_{Na} (red), and of the "ideal" distance, r_{id} (green), as explained in the text.

position of the minimum of v_{Ar} ($r_{\mathrm{Ar}} \simeq 2.57$ Å) is closer to r_{id} than the minimum of the Na⁺–He potential ($r_{\mathrm{Na}} \simeq 2.31$ Å). Moreover, even if the Ar⁺–He potential well is about 12 % less deep, its width at half depth is about 11 % wider, and this should reduce the zero-point motion of the ^{4}He atoms in the first shell. Thus, the overall effect should be the reinforcement of the stability of the icosahedral geometry in the first shell.

In the case of sodium ion, the stability of the icosahedron for N greater than a certain number of particles was already found. So we would expect that, with the argon ion, the stability is enhanced.

6.3.2 Details of the method

In order to perform an accurate microscopic study of ^{4}He nanodroplets doped with Ar⁺ at a realistic finite temperature we have employed the PIMC method, described in Chapter 1, using the Worm algorithm in the canonical ensemble (see Section 1.4). For the short-time propagator we have introduced and employed in this work a *pair-product* [4] variant of the multi-product expansion (MPE) approximation [50], called *'pair' multi-product expansion* approximation (PMPE) [139]. As I have explained in Section 1.6.3, we have built this new approximation [139] by using the pair form of the many-body propagator (see Eq. 1.39 on page 21) and by approximating the two–body propagator with the MPE approximation 1.45 and substituting the many-body coordinates $\mathbf{R}$ with the two-body relative coordinates $\boldsymbol{r}_{ij} = \boldsymbol{r}_i - \boldsymbol{r}_j$, i.e.

$$\hat{G}_{\mathrm{PMPE}}(\mathbf{R}, \mathbf{R}'; \delta\tau) = \prod_{i<j} G^{\mathrm{rel}}_{\mathrm{MPE}}\left(\boldsymbol{r}_{ij}, \boldsymbol{r}'_{ij}, \delta\tau\right) \tag{6.2}$$

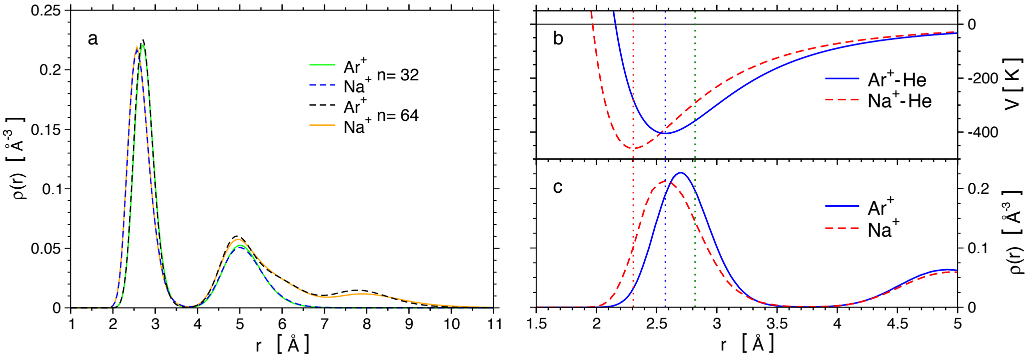

Figure 6.2 (**a**) Radial density profile, $\rho(r)$, of ^{4}He atoms around an Ar$^+$ ion and a Na$^+$ ion in nanodroplets with 32 and 64 ^{4}He atoms. (**b**) Same ion–He interaction potentials showed in Fig. 6.1 enlarged on the region of the minima. (**c**) Enlargement on the density profiles for the Ar$^+$@^{4}He$_n$ and Na$^+$@^{4}He$_n$ nanodroplets with $n = 128$.

For this work, we have adopted the 8-th order of the MPE approximation [50], and with the total imaginary-time step $\delta\tau = 1/160\,\mathrm{K}^{-1}$ we have accurate estimation of the observables.

In order to compare the results also with the those for Na$^+$@^{4}He$_n$ nanodroplets of Ref. [32], we initially performed simulations at $T = 1\,\mathrm{K}$, but we often observed evaporation of some atoms from the complex, so we changed the temperature to the lower value, $T = 0.5\,\mathrm{K}$. Actually the new value is nearer to the experimental temperature of the ^{4}He nanodroplets ($T = 0.37\,\mathrm{K}$) [147]. With this temperature we found that the evaporations do not occur and for all the performed simulations we have verified that v_{Ar} is attractive enough to bind the ^{4}He atoms to the nanodroplets, therefore our results are not affected by evaporations of atoms.

We remind that a PIMC calculation involve a simulation of special interacting ring-polymers, one for each atom in the system and the monomers, the beads of the polymers, correspond to the positions visited by that atom along the imaginary-time path. For each size of the nanodroplet we have run at least 5–20 × 10^4 Monte Carlo steps depending mainly on the size of the nanodroplets. Each Monte Carlo step consists of: an attempted rigid displacement move of each polymer; about one hundred of Brownian-bridge moves, that sample directly the kinetic part of the thermal density matrix, and one or two moves for the “worm” polymer that sample the particle permutations. Each Brownian-bridge move displaces some tens of monomers (about 1/20 of the total number of monomers). The acceptance ratio for swap moves was found to increase with the number of ^{4}He atoms in the nanodroplet, an indirect sign of the increase of superfluidity with the size of the nanodroplets. Unfortunately, only with this information we are not able to determine where the local superfluidity is present within the nanodroplet, since the acceptance ra-

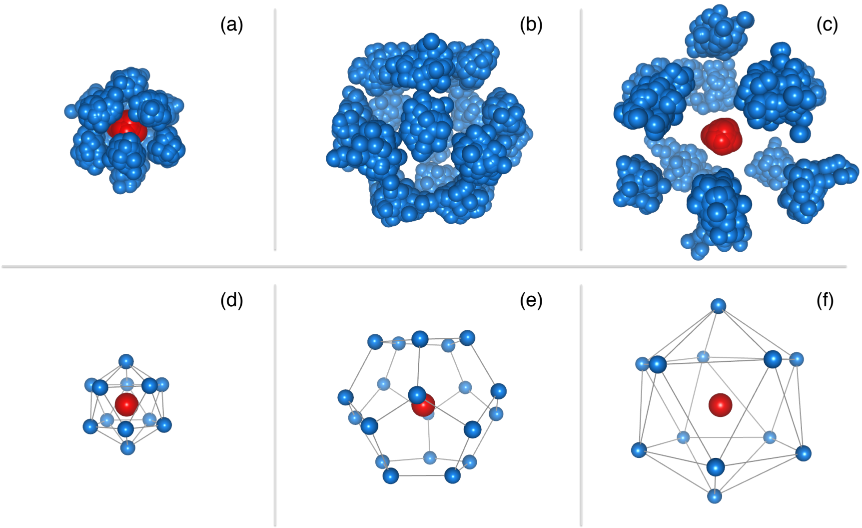

Figure 6.3 Example of a spatial configuration of polymers for a simulated nanodroplet with 128 ^{4}He atoms. In each of the top panels are shown the polymers associated to ^{4}He atoms of the first (**a**), the second (**b**) or the third shell (**c**) and the polymer of the Ar$^+$ ion (red balls). In the bottom panels (**d**,**e**,**f**) are shown the same shell configurations of the top panels, but each polymer is replaced by its center of mass.

tio provided by the simulation, carried out with the code exploited for this work, is a datum on the whole system. For this purpose, other than estimating specifically the local superfluid density, it would be interesting to register the swap acceptance ratios and the how many polymers are connected in a larger polymer in function of the position (relative to the central ion).

6.4 Results

In the initial stage of the work, we simulated doped nanodroplets with 32 and 64 ^{4}He atoms to compare directly density profiles and structures with those found for the nanodroplets doped with a Na$^+$ ion in Ref. [32]. As I have shown in Fig. 6.2a we found density profiles $\rho(r)$ for the two ions very similar. We observe that the density profiles for Ar$^+$ and Na$^+$, apart from the position of the first radial peak, r^{peak}, are very similar. In the Ar$^+$ case, the first peak is placed farther away from the ion, as an effect of the different position of the minimum of the wells of the ion–He potential. However, the ratio $r^{peak}_{\mathrm{Ar}}/r_{\mathrm{Ar}} \simeq 1.05$ is closer to one, than the ratio $r^{peak}_{\mathrm{Na}}/r_{\mathrm{Na}} \simeq 1.12$, indicating that the first shell in the Ar$^+$@^{4}He$_n$ nanodroplet follows more closely the minimum of the ion–He potential. We note also that the shape of the second modulation in the density profile is almost identical to that obtained in the Na$^+$ case. In the study of Na$^+$@^{4}He$_n$ [32], this

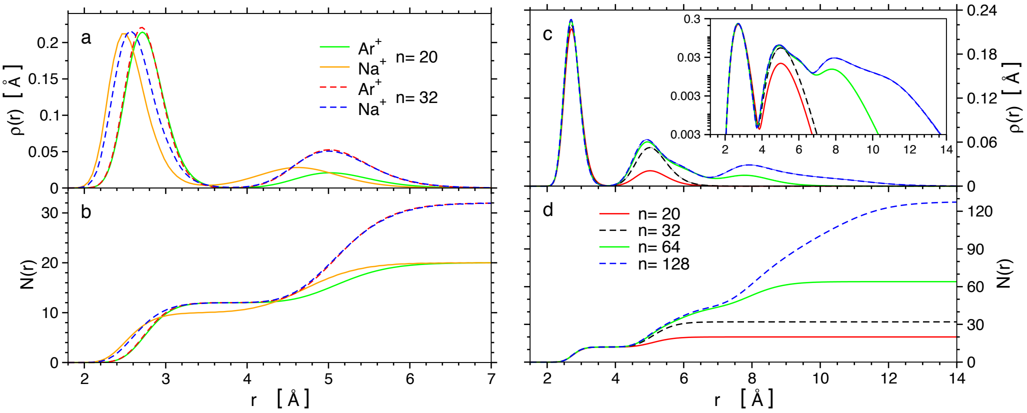

Figure 6.4 (**a**) Radial density profiles $\rho(r)$ of ^{4}He atoms around an Ar$^+$ ion and a Na$^+$ ion [32] in nanodroplets with $n = 20, 32$. (**b**) Number of ^{4}He atoms $N(r)$ within a sphere of radius r around the ion in the same nanodroplets of the panel **a**. (**b**) $\rho(r)$'s of ^{4}He, around, only, an Ar$^+$ ion in nanodroplets with $n = 20, 32, 64$, and 128 ^{4}He atoms. (inset) Same density profiles in logarithmic scale. (**c**) $N(r)$ for the same Ar$^+$ ion doped ^{4}He nanodroplets of the panel **c**.

modulation turned out to correspond to two tightly neighbouring shells, the second and the third, so we expected to find the same structure also for the Ar$^+$ case.

In order to investigate the local structure around the Ar$^+$ ion we have analysed some polymers configurations produced by the simulations. From each configuration we have extracted sub-configurations, each one for a different shell, through the following steps (implemented in a computer program): 1) from the starting configuration of the polymers a configuration of the centers of mass of the polymers is produced; 2) for each shell a sub-configuration of the polymers (or of the centers of mass) is built selecting the polymers whose center of mass is located in a chosen interval of relative positions from the center of mass of the ion (here also called radial positions). Clearly the chosen intervals are adjacent and non-overlapping. For the first shell the interval has been chosen between 0 and the minimum of the density profile placed between the first and the second modulation ($\simeq$ 3.7 Å) (see e.g. Fig. 6.2a). For the second shell, the second end of the interval has been harder to choose, because in the second modulation are present two radially overlapping profiles of two distinct shells, the second and the third. With some trials, based on the resulting number of the polymers belonging to the interval, we have determined a threshold radius ($\simeq$ 5.6 Å). For the third interval the second end is chosen to be the minimum ($\simeq$ 6.9 Å) situated between the second and the third modulation of the density profile, of nanodroplets with 64 ^{4}He atoms, or more. Finally, the fourth and last interval is chosen to be the region of the nanodroplets outside the first three intervals. Just observing, with a suitable software of graphical visualization, the sub-configurations of the centers of mass of the polymers (like those showed in Fig. 6.3), we can recognize immediately,

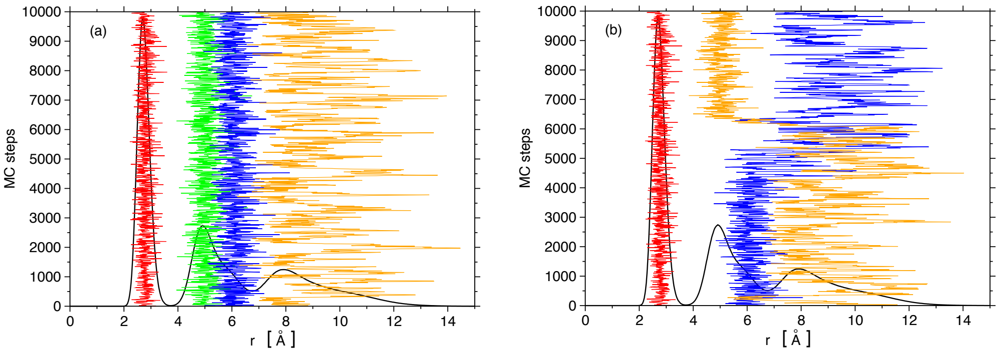

Figure 6.5 Evolution of the distance of some ^{4}He atoms from the Ar$^+$ ion during the MC simulation. Panels **a** and **b** show examples of such evolutions without (**a**) and in presence of (**b**) exchanges between the solid shells and the outer fluid part. (color figure online)

just by eye, the geometric shapes of the first three shells: an icosahedron in the first shell; a dodecahedron in the second shell, where each atom results to be placed on the face of the icosahedron beneath; and, again, an icosahedron in the third shell where each atom is located on the face of the dodecahedron underneath. In Fig. 6.3 I show, as example, the three sub-configurations of the shells thus obtained from a single configuration for a nanodroplet with 128 ^{4}He atoms. The sub-configurations of the polymers are showed in the top panels, while those of the centers of mass of the polymers are presented in the bottom panels.

From our PIMC simulations we have obtained evidence for a strong stability of the icosahedral structure in the first shell of Ar$^+$@^{4}He$_n$ at low temperatures: we have found that the number of ^{4}He atoms in the first shell is 12 for any studied $n \geq 12$. This is different from what was found for Na$^+$ doped nanodroplets, where only 10 ^{4}He atoms are present in the first shell for n below 30, while 12 atoms occur only for n above 30 [32]. This is clearly visible in Fig. 6.4a, where I show the number of ^{4}He atoms, $N(r)$, contained in a sphere of radius r centered on the ion, obtained through a numerical integration of the radial density profiles for $n = 20, 32$, showed inf Fig. 6.4b.

In Fig. 6.4c,d I show the density profiles $\rho(r)$ (6.4c) and and its volume integration in polar coordinates $N(r)$ (6.4d) for different numbers of ^{4}He atoms, $n = 20, 32, 64$, and 128. One can see, also looking at the same curves of $\rho(r)$ in logarithmic scale in the inset, that the first modulation of $\rho(r)$, associated to the first shell, changes only a little going from $n = 20$ to $n = 32$ and substantially does not change above $n = 32$. Observing the peak associated to the second shell, at $r \sim 4.9$ Å, which is complete for $n \leq 32$, one can notice that its radial position shortens from $n = 32$ to $n = 64$. This suggests that the second shell shrinks toward the central ion, under the pressure exerted by the atoms in the third shell and outside of it. Examining carefully the peak of the second modulation of $\rho(r)$

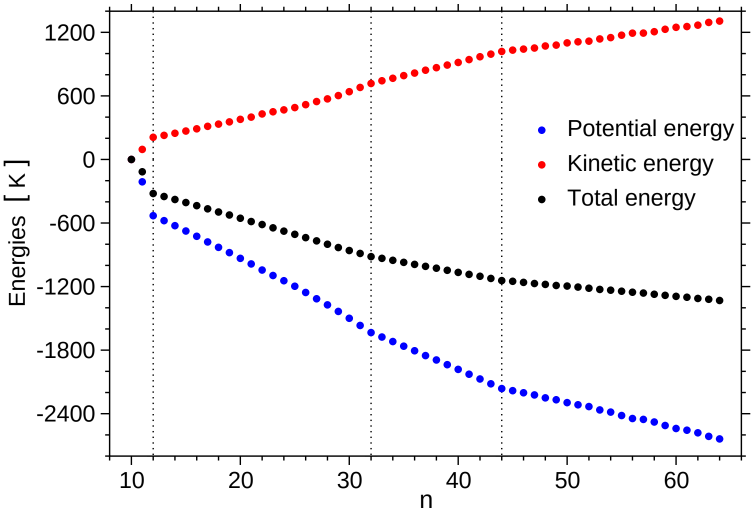

Figure 6.6 Total $E_n - E_{10}$, kinetic $K_n - K_{10}$ and potential $V_n - V_{10}$ energies per particle of Ar$^+$@^{4}He$_n$ complexes with different number, n, of ^{4}He atoms at $T = 0.5\,\text{K}$. All these energies has been shifted by the respective energies obtained for $n = 10$: $E_{10} = -2976(1)\,\text{K}$, $K_{10} = 614(1)\,\text{K}$ and $V_{10} = -3590.8(1)\,\text{K}$.

for nanodroplets with all the three shells complete, with $n = 64, 128$, one can observe its height increases a little and its radial position shortens going from $n = 64$ to $n = 128$. This indicates, again, a shrinking of the second and the third shell and an increase of the radial localization of the atoms therein.

To further characterize the microscopic nature of the solvation shells we have analysed also the radial localization of ^{4}He atoms around the Ar$^+$ ion by measuring the distance between the ^{4}He atoms and the ion during a PIMC simulation. In Fig. 6.5 I show the Monte Carlo evolution of the radial positions of four atoms started at different distances from the Ar$^+$ ion in a nanodroplet of 128 ^{4}He atoms as function of the Monte Carlo steps; a density profile is also shown in order to easily recognize the presence of exchanges of atoms among the shells. During our simulations we observed that atoms started in the first shell $\left(r \approx 2.7\,\text{Å}\right)$ fluctuate around their starting values, without moving to an outer shell. Also the most part of the atoms started in the second $\left(4.6\,\text{Å} \lesssim r \lesssim 5.5\,\text{Å}\right)$ or in the third shell $\left(5.5\,\text{Å} \lesssim r \lesssim 6.3\,\text{Å}\right)$ fluctuate around their starting values (see Fig. 6.5a), but sometimes an atom moves to another shell, or to the external region, conversely, an atom started in the external region can move to the second or third shell (see Fig. 6.5b). This analysis confirms the presence of local solid order in the two first modulations of the density profile, modulations which correspond to the first three shells around the Ar$^+$ ion. A very interesting issue for the future would be the measurement of the local superfluid density around the ion to investigate the simultaneous presence of solid order and

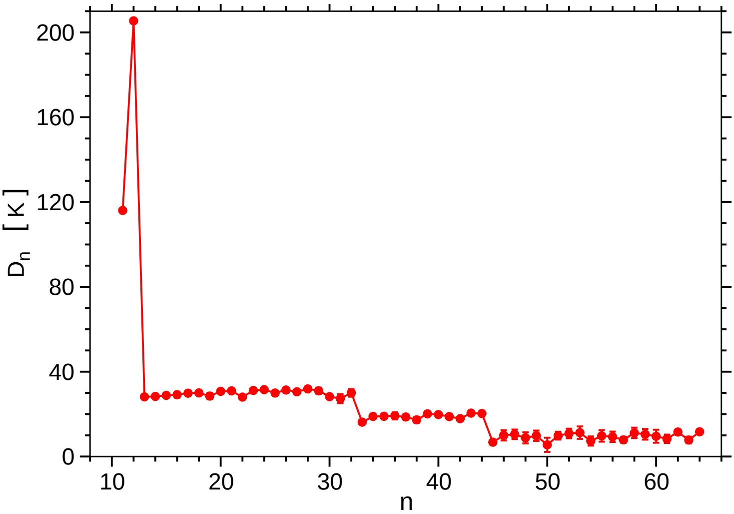

Figure 6.7 Dissociation energy $D_n = E_{n-1} - E_n$, where E_n is the total energy showed in Fig. 6.6 on the facing page.

superfluidity. However, in order to measure a local superfluid fraction of few percent, say 1–5 %, is necessary to reduce the error on the winding number [4] to order of 0.1 %. Within this aim, one should be also confident of having sampled with great accuracy particle exchanges, thus resulting in a challenging task. For these reasons we left such calculations for future investigations.

As discussed in Section 6.2, one of the experimental approaches to investigate the structure and the size of the snowball is to obtain information on the dissociation energies D_n, by looking for anomalies in the abundance distribution I_n of the X$^+$@^{4}He$_n$ complexes measured by means of mass spectrometry experiments. In fact, rapid changes of D_n due to closures of shells have to be reflected in I_n. To explore this aspects and to compare with the experimental results, we have calculated the total, kinetic and potential energies E_n, K_n, V_n, of the Ar$^+$@^{4}He$_n$ nanodroplets for different numbers of ^{4}He atoms, $10 \leq n \leq 64$ (see Fig. 6.6), and also for $n = 128$ (not showed in Fig. 6.6). From the Fig. 6.6 one can observe clearly three changes of slope exactly at the magic numbers found in Ref. [31], i.e. for $n = 12, 32$ and 44. From these energies we have also computed the dissociation energy D_n I show in Fig. 6.7. Here the magic numbers appear as discontinuity points. This result confirms the formation of shells with the same number of ^{4}He atoms discussed above, a structure which yields a very stable configuration for the complex.

6.5 Conclusions and perspectives

In summary, we have performed PIMC simulations of Ar$^+$ ion doped ^{4}He nanodroplets at low temperatures and characterized the microscopic structure of the snowball. We find that the structure around the ion Ar$^+$ is a highly ordered solid, a *snowball*, composed of three shells in which ^{4}He atoms are placed on the vertices of platonic solids: an icosahedron for the first and the third shells and a dodecahedron for the second shell. This solid structure was proposed in the interpretation of recent mass spectrometry measurements on Ar$^+$@^{4}He$_n$ complexes [31], where three magic numbers, 12, 32, 44, were found in the anomalies in the abundance distribution. The calculation of the total and the dissociation energy as a function of the size of the nanodroplets confirms the interpretation of the experimental data.

The same structure has been previously predicted in PIMC calculations for ^{4}He$_n$ nanodroplets doped with Na$^+$ [32] when $n > 30$. In the Ar$^+$@^{4}He$_n$ complexes the icosahedral order in the first shell has been found to be more stable and present for any $n \geq 12$ simulated in the present study. Remarkably, the analysis of the evolution of the radial positions of the ^{4}He atoms during the PIMC simulations revealed the occurrence of exchanges of helium atoms of the second and third shell with the outer region of the system. This raises the question of whether or not these atoms participate in local superfluidity. It will be interesting, even if challenging, in the future to calculate accurately local superfluid densities around the ions, especially in the shells where solid order is present.

Bibliography

[1] L. Reatto, in *Progress in Computational Pysics of Matter* (World Scientific, Singapore, 1995).

[2] M. H. Kalos, D. Levesque, and L. Verlet, Phys. Rev. A **9**, 2178 (1974).

[3] P. A. Whitlock, D. M. Ceperley, G. V. Chester, and M. H. Kalos, Phys. Rev. B **19**, 5598 (1979).

[4] D. M. Ceperley, Rev. Mod. Phys. **67**, 279 (1995).

[5] S. Baroni and S. Moroni, Phys. Rev. Lett. **82**, 4745 (1999).

[6] A. Sarsa, K. Schmidt, and W. Magro, J. Chem. Phys. **113**, 1366 (2000).

[7] D. E. Galli and L. Reatto, J. Phys. Soc. Jpn. **77**, 111010 (2008).

[8] D. M. Ceperley and B. J. Alder, Phys. Rev. Lett. **45**, 566 (1980).

[9] S. Gandolfi, F. Pederiva, S. Fantoni, and K. E. Schmidt, Phys. Rev. Lett. **98**, 102503 (2007).

[10] S. Giorgini, J. Boronat, and J. Casulleras, Phys. Rev. A **60**, 5129 (1999).

[11] U. Frisch and R. Bourret, J. Math. Phys. **11**, 364 (1970).

[12] M. Boninsegni, L. Pollet, N. Prokof'ev, and B. Svistunov, Phys. Rev. Lett. **109**, 025302 (2012).

[13] R. P. Feynman, Int. J. Theor. Phys. **21**, 467 (1982).

[14] D. M. Ceperley, in *Monte Carlo and Molecular Dynamics of Condensed Matter Systems*, edited by K. Binder and G. Ciccotti (Editrice Compositori, Bologna, Italy, 1996).

[15] J. Kaipio and E. Sommersalo, *Statistical and Computational Inverse Problems* (Springer-Verlag, New York, 2004).

[16] M. Jarrell and J. E. Gubernatis, Phys. Rep. **269**, 133 (1996).

[17] S. R. White, in *Computer Simulation Studies in Condensed Matter Physics III* (Springer-Verlag Berlin, Heidelberg, 1991) pp. 145–153.

[18] A. W. Sandvik, Phys. Rev. B **57**, 10287 (1998).

[19] A. S. Mishchenko, N. V. Prokof'ev, A. Sakamoto, and B. V. Svistunov, Phys. Rev. B **62**, 6317 (2000).

[20] S. Fuchs, T. Pruschke, and M. Jarrel, Phys. Rev. E **81**, 056701 (2010).

[21] E. Vitali, M. Rossi, L. Reatto, and D. E. Galli, Phys. Rev. B **82**, 174510 (2010).

[22] M. D. Ediger and P. Harrowell, J. Chem. Phys. **137**, 080901 (2012).

[23] D. W. Oxtoby, in *Liquids, Freezing and Glass Transition*, Proceedings of the Les Houches Summer School, Session LI, edited by J. P. Hansen, D. Levesque, and J. Zinn-Justin (Elsevier, Amsterdam, 1991).

[24] D. Turnbull, Contemp. Phys. **10**, 473– (1969).

[25] M. D. Ediger, P. Harrowell, and L. Yiu, J. Chem. Phys. **128**, 034709 (2008).

[26] M. L. F. Nascimento and E. D. Zanotto, J. Chem. Phys. **133**, 174701 (2010).

[27] J. Russo and H. Tanaka, Sci. Rep. **2**, 505 (2012).

[28] C. Tang and P. Harrowell, Nat. Mater. **12**, 507 (2013).

[29] M. Guerdane, H. Teichler, and B. Nestler, Phys. Rev. Lett. **110**, 086105 (2013).

[30] M. Kühnel, J. M. Fernández, F. Tramonto, G. Tejeda, E. Moreno, A. Kalinin, M. Nava, D. E. Galli, S. Montero, and R. E. Grisenti, Phys. Rev. B **89**, 180201 (2014).

[31] P. Bartl, C. Leidlmair, S. Denifl, P. Scheier, and O. Echt, J. Phys. Chem. A **118**, 8050 (2014).

[32] D. E. Galli, D. M. Ceperley, and L. Reatto, J. Phys. Chem. A **115**, 7300 (2011).

[33] E. Vitali, M. Rossi, F. Tramonto, D. E. Galli, and L. Reatto, Phys. Rev. B **77**, 180505 (2008).

[34] M. Rossi, M. Nava, L. Reatto, and D. E. Galli, J. Chem. Phys. **131**, 154108 (2009).

[35] J. E. Cuervo, P.-N. Roy, and M. Boninsegni, J. Chem. Phys. **122**, 114504 (2005).

[36] N. Metropolis, A. Rosenbluth, M. Rosenbluth, A. Teller, and E. Teller, J. Chem. Phys. **21**, 1087 (1953).

[37] M. Kalos and P. Whitlock, *Monte Carlo Methods Vol.1: Basics*, Interscience Publication, Vol. 1: Basics (Wiley, New Yor, 1986).

[38] M. Boninsegni, J. Low Temp. Phys. **141**, 27 (2005).

[39] M. Boninsegni, N. Prokof'ev, and B. Svistunov, Phys. Rev. Lett. **96**, 070601 (2006).

[40] M. Boninsegni, N. V. Prokof'ev, and B. V. Svistunov, Phys. Rev. E **74**, 036701 (2006).

[41] N. Prokof'ev and B. Svistunov, Phys. Rev. Lett. **87**, 160601 (2001).

[42] N. Prokof'ev, B. Svistunov, and I. Tupitsyn, J. Exp. Theor. Phys. **87**, 310 (1998).

[43] N. Prokof'ev, B. Svistunov, and I. Tupitsyn, Phys. Rev. A **238**, 253 (1998).

[44] F. Mezzacapo and M. Boninsegni, Phys. Rev. Lett. **97**, 045301 (2006).

[45] F. Mezzacapo and M. Boninsegni, Phys. Rev. A **75**, 033201 (2007).

[46] H. De Raedt and B. De Raedt, Phys. Rev. A **28**, 3575 (1983).

[47] H. F. Trotter, Proc. Am. Math. Soc. **10**, 545 (1959).

[48] E. L. Pollock and D. M. Ceperley, Phys. Rev. B **30**, 2555 (1984).

[49] S. Pilati, *Studies of ultracold gases using quantum Monte Carlo techniques*, Ph.D. thesis, Università degli Studi di Trento (2008).

[50] R. E. Zillich, J. M. Mayrhofer, and S. A. Chin, J. Chem. Phys. **132**, 044103 (2010).

[51] S. Chin, Celest. Mech. Dyn. Astr. **106**, 391 (2010).

[52] T. Minoguchi, M. Nava, F. Tramonto, and D. E. Galli, J. Low Temp. Phys. **171**, 259 (2013).

[53] D. Pines and P. Nozieres, *The theory of quantum fluids*, Vol. I (W. A. Benjamin, New York, 1966).

[54] D. Forster, *Hydrodynamic fluctuations, broken symmetry, and correlation functions*, Frontiers in Physics Series, Vol. 47 (WA Benjamin, Inc., Reading, Massachusetts,

1975).

[55] A. Griffin, *Excitations in a Bose-Condensed Liquid* (Cambridge University, Cambridge, England, 1993).

[56] N. I. Mushkelisvili, *Singular Integral Equations* (Noordhoof, 1953).

[57] R. Kubo, J. Phys. Soc. Jpn. **12**, 570 (1957).

[58] P. Martin and J. Schwinger, Phys. Rev. **115**, 1342 (1959).

[59] J. Hadamard, *Lectures on Cauchy's Problem in Partial Differential Equations* (Yale University Press, New Haven, 1923).

[60] J. Skilling, ed., *Maximum Entropy and Bayesian Methods* (Kluwer Academic, Dordrecht, 1989).

[61] J. E. Gubernatis, M. Jarrel, R. N. Silver, and D. S. Sivia, Phys. Rev. B **44**, 6011 (1991).

[62] R. K. Bryan, Eur. Biopys. **18**, 165 (1990).

[63] M. Boninsegni and D. M. Ceperley, J. Low Temp. Phys. **104**, 339 (1996).

[64] O. F. Syljuasen, Phys. Rev. B **78**, 174429 (2008).

[65] D. R. Reichman and E. Rabani, J. Chem. Phys **131**, 054502 (2009).

[66] A. Tarantola, Nat. Phys. **2**, 492 (2006).

[67] H. R. Glyde, *Excitations in Liquid and Solid Helium* (Clarendon Press, Oxford, 1994).

[68] L. Pitaevskii and S. Stringari, *Bose-Einstein Condensation* (Clarendon Press, Oxford, 2003).

[69] F. Dalfovo, S. Giogrini, L. P. Pitaevskii, and S. Stringari, Rev. Mod. Phys. **71**, 463 (1999).

[70] J. Steinhauer, R. Ozeri, N. Katz, and N. Davidson, Phys. Rev. Lett **88**, 120407 (2002).

[71] E. C. Svensson, P. Martel, V. F. Sears, and A. D. B. Woods, Can. J. Phys. **54**, 2178 (1976).

[72] E. F. Talbot, H. R. Glyde, W. G. Stirling, and E. C. Svensson, Phys. Rev. B **38**, 11229 (1988).

[73] W. G. Stirling and H. R. Glyde, Phys. Rev. B **41**, 4224 (1990).

[74] K. H. Andersen, W. G. Stirling, R. Scherm, A. Stunault, B. Fak, H. Godfrin, and A. J. Dianoux, J. Phys: Condens. Matter **6**, 821 (1994).

[75] K. H. Andersen and W. G. Stirling, J. Phys: Condens. Matter **6**, 5805 (1994).

[76] M. R. Gibbs, K. H. Andersen, W. G. Stirling, and H. Schober, J. Phys: Condens. Matter **11**, 603 (1999).

[77] R. P. Feynman, Phys. Rev. **94**, 262 (1954).

[78] R. Rota, F. Tramonto, D. E. Galli, and S. Giorgini, Phys. Rev. B **88**, 214505 (2013).

[79] K. Huang and C. N. Yang, Phys. Rev. **105**, 767 (1957).

[80] J. P. Hansen, D. Levesque, and D. Shiff, Phys. Rev. A **3**, 776 (1971).

[81] J. Cao and B. J. Berne, J. Chem. Phys. **97**, 2382 (1992).

[82] L. H. Nosanow, Phys. Rev. **146** (1966).

[83] S. T. Beliaev, Zh. Eksp. Teor. Fiz. **34**, 433 (1958), [Sov. Phys. JETP **7**, 299 (1958)].

[84] J. Boronat, J. Casulleras, and S. Giorgini, Phys. B **284**, 1 (2000).

[85] R. J. Donnelly, J. A. Donnelly, and R. N. Hills, J. Low Temp. Phys. **44**, 471 (1981).

[86] E. C. Svensson, V. F. Sears, A. D. B. Woods, and P. Martel, Phys. Rev. B **21**, 3638 (1980).

[87] F. K. Achter and L. Meyer, Phys. Rev. **188**, 291 (1969).

[88] R. Cowley and A. Woods, Can. J. Phys. **49**, 177 (1971).

[89] E. Vitali, D. E. Galli, and L. Reatto, in *Advanced in Quantum Many-body Theory*, Vol. 11 (2008) p. 251.

[90] R. Rota, J. Casulleras, F. Mazzamti, and J. Boronat, Phys. Rev. E **81**, 016707 (2010).

[91] A. Denton, P. Nielaba, K. Runge, and N. Ashcroft, Phys. Rev. Lett. **64**, 1529 (1990).

[92] M. Rossi and L. Salasnich, Phys. Rev. A **88**, 053617 (2013).

[93] F. Cinti, P. Jain, M. Boninsegni, A. Micheli, P. Zoller, and G. Pupillo, Phys. Rev. Lett. **105**, 135301 (2010).

[94] S. Saccani, S. Moroni, and M. Boninsegni, Phys. Rev. B **83**, 092506 (2011).

[95] S. P. Das, *Statistical physics of liquids at freezing and beyond* (Cambridge University Press Cambridge, UK, 2011).

[96] F. Caupin and T. Minoguchi, J. Low Temp. Phys. **138**, 331 (2005).

[97] C. N. Likos, S. Moroni, and G. Senatore, Phys. Rev. B **55**, 8867 (1997).

[98] T. V. Ramakrishnan and M. Yussouff, Phys. Rev. B **19**, 2775 (1979).

[99] T. Minoguchi and D. E. Galli, J. Low Temp. Phys. **162**, 160 (2011).

[100] T. Minoguchi, D. E. Galli, M. Rossi, and A. Yoshimori, J. Phys.: Conf. Ser. **400**, 012050 (2012).

[101] B. K. Clark and D. M. Ceperley, Phys. Rev. Lett. **96**, 105302 (2006).

[102] F. Caupin, J. Boronat, and K. H. Andersen, J. Low Temp. Phys. **152**, 108 (2008).

[103] M. Rossi, E. Vitali, L. Reatto, and D. E. Galli, Phys. Rev. B **85**, 014525 (2012).

[104] R. A. Aziz, V. P. S. Nain, J. S. Carley, W. L. Taylor, and G. T. McConville, J. Chem. Phys. **70**, 4330 (1979).

[105] J. S. Brooks and R. J. Donnelly, J. Phys. Chem. Ref. Data **6**, 51 (1977).

[106] A. R. Denton and N. W. Ashcroft, Phys. Rev. B **39**, 4701 (1989).

[107] A. R. Denton, P. Nielaba, and N. W. Ashcroft, J. Phys.: Condens. Matter (1997).

[108] D. E. Galli, L. Reatto, and W. M. Saslow, Phys. Rev. B **76**, 052503 (2007).

[109] U. Gasser, J. Phys.: Condens. Matter **21**, 203101 (2009).

[110] G. L. Hunter and E. R. Weeks, Rep. Prog. Phys. **75**, 066501 (2012).

[111] H. J. Schöpe, G. Bryant, and W. van Megen, J. Chem. Phys. **127**, 084505 (2007).

[112] V. L. Ginzburg and A. A. Sobyanin, JETP Lett. **15**, 242 (1972).

[113] O. N. Osychenko, R. Rota, and J. Boronat, Phys. Rev. B **85**, 224513 (2012).

[114] D. Coslovich and G. Pastore, J. Chem. Phys. **127**, 124504 (2007).

[115] L.-C. Valdes, F. Affouard, M. Descamps, and J. Habasaki, J. Chem. Phys. **130**, 154505 (2009).

[116] U. R. Pedersen, T. B. S. der, J. C. Dyre, and P. Harrowell, Phys. Rev. Lett. **104**, 105701 (2010).

[117] S. Jungblut and C. Dellago, J. Chem. Phys. **134**, 104501 (2011).

[118] A. Banerjee, S. Chakrabarty, and S. M. Bhattacharyya, J. Chem. Phys. **139**, 104501 (2013).

[119] I. F. Silvera, Rev. Mod. Phys. **52**, 393 (1980).

[120] M. Zoppi, J. Phys.: Condens. Matter **15**, R1047 (2003).

[121] J. De Boer, Phys. **14**, 139 (1948).

[122] J. De Boer and B. Blaisse, Phys. **14**, 149 (1948).

[123] J. De Boer and R. Lunbeck, Phys. **14**, 520 (1948).

[124] E. Rabani and D. R. Reichman, Annu. Rev. Phys. Chem. **56**, 157 (2005).

[125] M. Kühnel, J. M. Fernández, G. Tejeda, A. Kalinin, S. Montero, and R. E. Grisenti, Phys. Rev. Lett. **106**, 245301 (2011).

[126] B. J. Kozioziemski and G. W. Collins, Phys. Rev. B **67**, 174101 (2003).

[127] D. White and J. R. Gaines, J. Chem. Phys. **42**, 4152 (1965).

[128] D. M. Herlach and P. K. Galenko, Mater. Sci. Eng. A **449**, 34 (2007).

[129] K. A. Jackson, Inter. Sci. **10**, 159 (2002).

[130] M. Leocmach, J. Russo, and H. Tanaka, J. Chem. Phys. **138**, 12A536 (2013).

[131] P. Steinhardt, D. R. Nelson, and M. Ronchetti, Phys. Rev. B **28**, 784 (1983).

[132] M. Leocmach and H. Tanaka, Nat. Commun. **3**, 974 (2012).

[133] W. Lechner and C. Dellago, J. Chem. Phys. **129**, 114707 (2008).

[134] A. P. Lima, A. S. Martins, and J. S. S. Martins, Phys. A **391**, 4281 (2012).

[135] S. R. Williams, C. P. Royall, and G. Bryant, Phys. Rev. Lett. **100**, 225502 (2008).

[136] G. Tarjus, S. A. Kivelson, Z. Nussinov, and P. Viot, J. Phys.: Condens. Matter **17**, R1143 (2006).

[137] F. C. Frank, Proc. R. Soc. London Ser. A **215**, 43 (1952).

[138] A. Hirata, L. J. Kang, T. Fujita, B. Klumov, K. Matsue, M. Kotani, A. R. Yavari, and M. W. Chen, Science **341**, 376 (2013).

[139] F. Tramonto, P. Salvestrini, M. Nava, and D. Galli, J. Low Temp. Phys. (2015), 10.1007/s10909-014-1266-6.

[140] E. Lugovoj, J. P. Toennies, and A. F. Vilesov, J. Chem. Phys. **112**, 8217 (2000).

[141] S. A. Krasnokutski and F. Huisken, J. Phys. Chem. A **115**, 7120 (2011).

[142] J. P. Toennies and A. F. Vilesov, Annu. Rev. Phys. Chem. **49**, 1 (1998).

[143] K. B. Whaley, in *Advances in molecular vibrations and collision dynamics*, Vol. 3, edited by J. M. Bowman and Z. Bačić (JAI Press, Stamford, CT, 1998) p. 397.

[144] J. P. Toennies, A. F. Vilesov, and K. B. Whaley, Phys. Today **54**, 31 (2001).

[145] C. Callegari, K. K. Lehmann, R. Schmied, and G. Scoles, J. Chem. Phys. **115**, 10090 (2001).

[146] F. Stienkemeier and A. F. Vilesov, J. Chem. Phys. **115**, 10119 (2001).

[147] J. P. Toennies and A. F. Vilesov, Angew. Chem. Int. Ed. **43**, 2622 (2004).

[148] M. Barranco, R. Guardiola, S. Hernández, R. Mayol, J. Navarro, and M. Pi, J. Low Temp. Phys. **142**, 1 (2006), and references therein.

[149] C. Callegari and W. E. Ernst, in *Handbook of High-resolution Spectroscopy*, edited by M. Quack and F. Merkt (John Wiley and Sons, Chichester, UK, 2011) pp. 1551–1594.

[150] E. Latimer, D. Spence, C. Feng, A. Boatwright, A. M. Ellis, and S. Yang, Nano Lett. **14**, 2902 (2014).

[151] D. Spence, E. Latimer, C. Feng, A. Boatwright, A. M. Ellis, and S. Yang, Phys. Chem. Chem. Phys. **16**, 6903 (2014).

[152] S. Yang, A. M. Ellis, D. Spence, C. Feng, A. Boatwright, E. Latimer, and C. Binns, Nanoscale **5**, 11545 (2013).

[153] G. Careri, F. Scaramuzzi, and J. Thomson, Il Nuovo Cimento **13**, 186 (1959).

[154] F. Reif and L. Meyer, Phys. Rev. **119**, 1164 (1960).

[155] G. Careri, in *Prog. Low Temp. Physics, Vol. III*, edited by C. J. Gorter (North-Holland Publishing Co., Amsterdam, Netherlands, 1964) pp. 58–79.

[156] A. L. Fetter, in *The Physics of Liquid and Solid Helium, Part I*, Interscience Monographs and Texts in Physics And Astronomy, edited by K. H. Bennemann and J. B. Ketterson (Wiley, New York, 1976) Chap. 3, p. 207.

[157] K. R. Atkins, Phys. Rev. **116**, 1339 (1959).

[158] J. Tiggesbaumker and F. Stienkemeier, Phys. Chem. Chem. Phys. **9**, 4748 (2007).

[159] K. Hiraoka, A. Shimizu, A. Minamitsu, M. Nasu, H. Wasada, and S. Yamabe, J. Chem. Phys. **108**, 6689 (1998).

[160] T. Kojima, N. Kobayashi, and Y. Kaneko, Z. Phys. D: At., Mol. Clust. **22**, 645 (1992).

[161] B. E. Callicoatt, K. Förde, T. Ruchti, L. Jung, K. C. Janda, and N. Halberstadt, J. Chem. Phys. **108**, 9371 (1998).

[162] C. A. Brindle, M. R. Prado, K. C. Janda, N. Halberstadt, and M. Lewerenz, J. Chem. Phys. **123**, 064312 (2005).

[163] J. H. Kim, D. S. Peterka, C. C. Wang, and D. M. Neumark, J. Chem. Phys. **124**, 214301 (2006).

[164] F. Ferreira da Silva, P. Bartl, S. Denifl, O. Echt, T. D. Mark, and P. Scheier, Phys. Chem. Chem. Phys. **11**, 9791 (2009).

[165] E. Coccia, E. Bodo, F. Marinetti, F. A. Gianturco, E. Yildrim, M. Yurtsever, and

E. Yurtsever, J. Chem. Phys. **126**, 124319 (2007).

[166] E. Bodo, E. Coccia, D. López-Durán, and F. A. Gianturco, Phys. Scr. **76**, C104 (2007).

[167] S. Paolini, F. Ancilotto, and F. Toigo, J. Chem. Phys. **126**, 124317 (2007).

[168] E. Coccia, E. Bodo, and F. A. Gianturco, EPL **82**, 23001 (2008).

[169] S. Bovino, E. Coccia, E. Bodo, D. Lopez-Durán, and F. A. Gianturco, J. Chem. Phys. **130**, 224903 (2009).

[170] D. E. Galli, M. Buzzacchi, and L. Reatto, J. Chem. Phys. **115**, 10239 (2001).

[171] M. Buzzacchi, D. E. Galli, and L. Reatto, Phys. Rev. B **64**, 094512 (2001).

[172] M. Rossi, M. Verona, D. E. Galli, and L. Reatto, Phys. Rev. B **69**, 212510 (2004).

[173] A. Carrington, C. A. Leach, A. J. Marr, A. M. Shaw, M. R. Viant, J. M. Hutson, and M. M. Law, J. Chem. Phys. **102**, 2379 (1995).

[174] R. Ahlrichs, H. J. Böhm, S. Brode, K. T. Tang, and J. P. Toennies, J. Chem. Phys. **88**, 6290 (1988).

Acknowledgments

I would like to thank my parents and my sister for supporting and encouraging me for all these years of study.

I wish sincerely to express my deep gratitude to Prof. Davide Galli for his patient guidance, encouragement, enthusiasm and for our friendship.

I thank all the professors and researchers which I have worked with in the fruitful collaborations: Robert Grisenti, Riccardo Rota, Stefano Giorgini and Tomoki Minoguchi.

I thank all the people of the LCP group for their friendship and helpfulness: Gianluca Bertaina, Mario Motta, Marco Nava, Ettore Vitali, Maurizio Rossi. And also the undergraduates of the group that I have met during the PhD years: Alessandro Colombo, Federico Arrigoni, Francesco Mambretti, and Martina Teruzzi.